BALLISTIC CARRIER TRANSPORT IN SEMICONDUCTORS STUDIED BY ULTRAFAST LASER TECHNIQUES

BY

Lalani K. Werake

Submitted to the Graduate Degree Program in Physics and Astronomy

and the Faculty of the Graduate School of the University of Kansas in partial fulfillment of the requirements for the degree of Doctor of Philosophy.

Dr. Hui Zhao, Thesis Supervisor

Dr. Siyuan Han

Dr. Judy Wu

Dr. Matthew Antonik

Dr. Christopher Elles

Date defended: April 19, 2011

The dissertation committee for Lalani K. Werake certifies

that this is the approved version of the following dissertation:

BALLISTIC CARRIER TRANSPORT IN SEMICONDUCTORS

STUDIED BY ULTRAFAST LASER TECHNIQUES

Thesis Committee:

Dr. Hui Zhao, Thesis Supervisor

Dr. Siyuan Han

Dr. Judy Wu

Dr. Matthew Antonik

Dr. Christopher Elles

Date Accepted: July 30, 2011

Abstract

Exploring the spin degree of freedom of electrons has been recognized as a promising solution to several limitations in semiconductor device industry. Injection, transport, detection and manipulation of "spin" in materials are the key elements of this new electronic technology, known as spintronics. Despite the extensive efforts in recent years, there are still significant challenges and spintronics is still in the research phase.

This dissertation is devoted to study one of these key processes: spin transport. We used quantum interference and control technique to inject spin currents. Two techniques are developed to detect the spin transport, namely a pump probe technique and a second-harmonic generation technique. Spin transport in several materials and structures are studied, including GaAs bulk, quantum wells, and germanium wafers. We observed the intrinsic inverse spin-Hall effect by time-resolving the ballistic spin and charge transport. We found that the Hall current appeared before the first scattering event. We discovered a new nonlinear optical effect, second-harmonic generation, induced by the pure spin current, and demonstrated that it can be used to directly detect pure spin currents. We have also discovered a charge-current-induced second-harmonic generation process, and used it to study plasma oscillation in GaAs. Finally, we also attempted to observe the second harmonic generation induced by spin polarized and spin unpolarized carrier populations. We did not observe a significant change in the observed second harmonic generation induced by spin polarized and spin unpolarized carrier populations.

~ ~ §~ ~

Dedicated with deep love and affection to

Govinda Jayasinghe; my soul mate,

Chandra and Werake Bandara; my parents

and

Lakmini and Chaminda Werake Bandara; my sister and my brother

-whose love and support encouraged me

to be more than that I thought I could be

~ ~ § ~ ~

Acknowledgement

My graduate school experience has been enriched through the interaction with many wonderful people. The completion of my Ph.D. would not have been possible without their friendship and support, for which I am truly grateful. I am immensely grateful to my advisor, Dr. Hui Zhao. I feel extremely fortunate to be his first Ph.D. graduate. He had been nothing but an amazing mentor. During my first few months in the lab, he made time to look over my shoulders, give me a helping hand and train me with his ability and skills. Right through out, he was very patient and very supportive in every possible way. The compassion he showed was a reminder that he cared about us as individuals not just as employees. His enthusiasm lifted my spirits and inspired me to work harder. Many, many thanks, Dr. Zhao. I have had a wonderful graduate career, and it has been because of your advising style and engaging research program.

A special recognition needs to be given to Dr. Siyuan Han, Dr. Judy Wu, Dr. Mathew Antonik and Dr. Christopher Elles for serving as my co-advisors. Thank you very much for all your valuable input.

I sincerely acknowledge my wonderful colleagues in the group, Brian Ruzicka and Eric Loren for all the good times we have had, inside and outside the lab. I have learned a lot from both of you. I also want to thank our most junior member of the group, Nardeep Kumar, for all your jokes and the lab was full of laugh when you were around.

Finally, I would take this opportunity to thank my former teachers from University of Missouri – Science and Technology, University of Peradeniya in Sri Lanka. Special thanks for Dr. Upali Karunasiri, for advising and supporting me to pursue my graduate studies.

Contents

LIST OF FIGURES

Figure Page

Chapter 1

Chapter 2

Chapter 3

Chapter 4

Chapter 5

Chapter 6

Chapter 7

LIST OF SYMBOLS AND ABBREVIATIONS

Symbol / Abbreviation	Definition
$a_{cv}(\boldsymbol{k})$	Interband transition amplitude
$a_{cv}^{2\omega}(\boldsymbol{k})$	One-photon transition amplitude driven by the 2ω pulse
$a_{cv}^{\omega}(\boldsymbol{k})$	Two-photon transition amplitude driven by the ω pulse
$\boldsymbol{B}$	Magnetic field
BBO	Beta barium borate
c	Speed of light
CB	Conduction band
CMOS	Complementary metal-oxide-semiconductor
D_n	Diffusion co-efficient of electrons
D_p	Diffusion co-efficient of holes
e	Charge of an electron
$\boldsymbol{E}$	Electric field
$\boldsymbol{E}_{2\omega}(r,t)$	Electric field of the 2ω pulse
$\boldsymbol{E}_{\omega}(r,t)$	Electric field of the ω pulse
E_{bit}	Energy dissipation as heat in the loss of information / bit
E_{LO}	Electric field amplitude of the local oscillator
E_P	Electric field amplitude of the probe pulse (1790 nm)
FWHM	Full width at half maximum
G	Gain
GDD	Group delay dispersion
$\hbar$	Planck constant
$\hbar k$	Crystal momentum

I_{in}	Intensity of the incident beam
I_{out}	Intensity of the transmitted beam
$I_{\omega,2\omega}$	Intensity of ω and 2ω pulses
J	Density of pure charge current
$J_{diffusion}$	Diffusion current density
J_{drift}	Drift current density
K	Density of pure spin current
k(ω)	Spectral phase
$\boldsymbol{L}$	Orbital angular momentum
L	Length of the medium
$L_{s(N)}$	Separation of spin (electron)profiles along x-direction
LO	Local oscillator
m	Mass of an electron
N	Carrier density
n	Density of electrons
n_j	Refractive index
$N^{\uparrow}$	Carrier density of spin up electrons
$N^{\downarrow}$	Carrier density of spin down electrons
$N_{Saturation}$	Saturated carrier density
OPO	Optical parametric oscillator
p	Density of holes
$\boldsymbol{P}$	Polarization
P	Power of the light
PCC	Pure charge current
PSC	Pure spin current

$P_{x,y,z}$	The x,y,z components of momentum
QUIC	Quantum interference and control
S	Spin density
SHE	Spin-Hall effect
SHG	Second harmonic generation
SOI	Spin-orbital interaction
SPCC	Spin-polarized charge current
T	Transmission co-efficient
T_o	Linear transmission
$\boldsymbol{v}$	Velocity
v	Potential energy between electron and nucleus
V	Voltage
$\langle \boldsymbol{v} \rangle$	*A*verage velocity of the electrons
$\langle \boldsymbol{v}^{\uparrow} \rangle$	Average velocity of spin up electrons
$\langle \boldsymbol{v}^{\downarrow} \rangle$	Average velocity of spin down electrons
$\boldsymbol{v}_0$	Initial velocity of the electrons
$\boldsymbol{v}_G$	Group velocity
VB	Valence band
$w_{unknown,known,sum}$	Temporal width of the compressed pulse, known pulse and the sum
α	Absorption co-efficient
α_n	Absorption co-efficient with the presence of the pump pulse
α_o	Linear Absorption co-efficient
$\nabla n(p)$	density gradient of the electrons (holes)

$\Delta\alpha_n$	Change in absorption
ΔT	Differential transmission
$\Delta\phi$	Relative phase between ω and 2ω pulses
$\Delta T^{+(-)}$	Differential transmission of right (left) circular polarizations
$\Delta\omega_p$	Spectral width
Δt	Temporal width of the pulse
$\Delta\lambda$	Bandwidth
ΔN	Electron accumulation
Δx	Motion of the spin profiles along x direction
Δy	Motion of the electron profiles along y direction
ΔP	Spin/charge current induced SHG
ΔI	Intensity of the SHG induced by PSC
η	Current injection efficiency
μ	Intrinsic magnetic moment
$\mu_{p(n)}$	Mobility of holes (electrons)
$\hat{\sigma}^+$	Right circular polarization
ϵ_0	Permittivity of the free space
τ	Probe delay
τ_p	Duration of the pulse
τ_m	Momentum relaxation time
$\Phi_{\omega(2\omega)}$	Phase of ω (2ω) pulse
$\psi_{c(v)k}$	Wave function of electrons (holes) in the CB (VB)
χ	Susceptibility

List of publications

[1] **Werake, L.,** Ruzicka, B. and Zhao, H. (2011) "Observation of intrinsic inverse spin Hall effect" *Phys. Rev. Lett.* 106 107205

[2] **Werake, L.** and Zhao, H. (2010) "Observation of second-harmonic generation induced by pure spin current" *Nat. Phys.* 6 875

[3] **Werake, L.,** Story, G. Bertino, M. and Blum, F. (2005) "Photolithographic synthesis of polyaniline nanofibres" *Nanotechnology* 16 2833-2837

[4] Ruzicka, B., **Werake, L.**, Samassekou, H. and Zhao, H. (2010) "Ambipolar diffusion of photo-excited carriers in bulk GaAs" *Appl. Phys. Lett.* 97 262119

[5] Ruzicka, B., Wang, S., **Werake, L.**, Weintrub, B., Loh, K. and Zhao, H. (2010) "Hot carrier diffusion in graphene" *Phys. Rev. B* 82 195414

[6] Ruzicka, B., **Werake, L**. and Zhao, H. (2010) "Femtosecond pump-probe studies of reduced graphene oxide thin films" *Appl. Phys. Lett.* 96 173106

[7] Loren, E., Ruzicka, B.**, Werake, L**. and Zhao, H. (2009) "Optical injection and detection of ballistic pure spin current in Ge" *Appl. Phys. Lett.* 95 092107

[8] Ruzicka, B.A., **Werake, L**. and Zhao, H. (2008) "All-optical generation and detection of sub-picosecond ac spin-current pulses in GaAs" *Phys. Rev. B* 78 045314

[9] Blum, F., Pillalamarri, S., **Werake, L**., Story, J., Bertino, M. and Tokuhiro, A. (2006) "Nanometal Containing Nanocomposites and Photolithographic Polyaniline, Nanofibers" *Polymer Preprints* 47 405

Chapter 1: Introduction

The fast development of modern electronic technology relies on the continuous reduction of the size of the elementary devices in integrated circuits; thus increase in the density of the devices. As Moore's law predicted, the density of the devices doubled in every two years, which resulted in an exponential increase in the information processing capability. Now, the channel length of a transistor in an integrated circuit is 22 nm and the goal is to reach 10 nm in 2018, according to the International Technology Roadmap for Semiconductors. (Intel press, 2011; International Technology Roadmap for Semiconductors 2003)

However, is it possible to achieve further progress in electronic technology by simply continuing the reduction of the size of the transistors in microprocessors and other electronic devices? This has been recognized as a non-realistic approach since further increase of the device density will cause several technical issues. First, computers heat up as electrons move through miles long tiny wires in microchips. More heat is generated per unit area with higher device density, causing problems on heat dissipation. Second, the static-power dissipation is challenging in improving device performance which is related to the dynamic-power dissipation (from gate switching) in complementary metal-oxide-semiconductor. (Prinz 1998)

Moreover, there are design and fabrication issues as well as quantum effects of electrons. Therefore, new approaches have to be explored. Among them, spintronics is a promising candidate. (Wolf 2001; Zutic 2004)

1.1 Spintronics

Spintronics involves magnetism, electronic transport, and optics. (Flatte 2007) Its central theme is the active manipulation of spin degree of freedom in solid-state systems. The goals of spintronics are to understand the interaction between the electronic and nuclear spins and their solid-state environments and to make useful devices with higher capabilities and new functions compared to the traditional charge-based technology. (Zutic 2004; Wolf 2001; Prinz 1998; Baibich 1988; Moonlera 1995)

There are many advantages of using spin, instead of charge, to carry information. The charge conservation requires that in steady transport, every electron entering an electrical component of a circuit must exits. Thus the charge transport in semiconductors sustains large deviations of local-charge density from equilibrium. In contrast to charge-based electronic devices, spintronics employs the transfer of spin orientation of electrons.

A magnetic field induced spin-flip of an electron is faster than lowering or raising the energy barrier in a metal-oxide-semiconductor field-effect transistor. A 1 meV spin splitting can cause a spin to completely reorient by precession in only 2 ps. (Hall 2003) Generating this spin flip via applying an electric field, through the spin-orbital interaction (SOI) needs a very small threshold voltage compared to complementary metal-oxide-semiconductor devices. The threshold voltage in the recently proposed InAs/GaSb/AlSb heterostructure is ~ 2000 times smaller. Furthermore, the achieved smaller capacitance yields an estimated power-delay product 500 times smaller. (Hall 2003) Therefore, using spin degree of freedom will allow ultra-small logic elements and ultrafast computer chips of higher information processing capacity and lower energy consumption. The spin-transistor design, with charge inputs, outputs, and gates is significant to complementary metal-oxide-semiconductor at the end of the roadmap node in 2018. (International Technology Roadmap of Semiconductors 2003; Flatte 2007). In addition, the quantum mechanical nature of spin makes it a natural choice for carrying quantum information. In fact, electronic and nuclear spins have been used as quantum bits in some promising proposals for quantum computers, (Loss et al 1998; Kane 1998) which need to coherently manipulate the spins. (Ivanov 2004; Dietl 2007; Wolf 2001; Das Sarma 2000).

Although, most fundamental advantages of spin have only been demonstrated in research laboratory, practical applications of spintronics already exist, and improvement in the conventional microelectronics has been demonstrated. The first practical spintronics; “spin valve” is used to read information from hard drives. The second generation device, a type of computer memory knows as a magnetoresistive random access memory has been used as hard disks and other types of memories such as flash memory, commonly used in digital cameras. It has no moving parts and can store data without consuming energy.

Although the giant magneto resistance-based technology is the first spintronics technology with practical applications, and is the most successful spintronics technology so far, the majority of research is now focused on semiconductor-based spintronics. (Zutic 2004, Wolf

2001) This is because only the semiconductor-based spintronics can be integrated with the charge-based semiconductor technologies, taking advantage of the current technologies of fabricating and characterizing electronic devices. In this dissertation, I will focus on the semiconductor-based spintronics.

1.2 Semiconductor spintronics

The physics foundation of spintronics is the spin-orbital interaction, which is the interaction between the spin motion of an electron (magnetic moment) and its linear motion in the crystal. Since, most semiconductors are non-centrosymmetric, the consequences of the SOI is different in semiconductors than in metals. (Flatte 2007) To illustrate the concept of SOI, let's consider the interaction between an electron and the protons in an atom,

$$v(r) = \frac{1}{4\pi\epsilon_0}\frac{-Ze}{r}, \tag{1.1}$$

which corresponds to an electric field,

$$\boldsymbol{E} = \frac{1}{4\pi\epsilon_0}\frac{Ze}{r^3}\boldsymbol{r}, \tag{1.2}$$

where ϵ_0, e and Z are the permittivity of the free space, electron charge and the atomic number, respectively. Due to the relative motion between the electron and the nucleus, a magnetic field will be experienced by the electron,

$$\boldsymbol{B} = \boldsymbol{E} \times \frac{\boldsymbol{v}}{c} = \left(\frac{1}{4\pi\epsilon_0}\right)^{\mathbf{2}} \frac{Ze^2}{cr^3}\boldsymbol{r} \times \boldsymbol{v} = \left(\frac{1}{4\pi\epsilon_0}\right)^{\mathbf{2}} \frac{Ze^2}{mc}\frac{1}{r^3}\boldsymbol{L}, \tag{1.3}$$

where c is the speed of light, $\boldsymbol{v}$ and m are the velocity and the mass of the orbiting electron, $\boldsymbol{E}$ is the electric field, and $\boldsymbol{L}$ is the orbital angular momentum of the electron. In this magnetic field, an electron with its intrinsic magnetic moment,

$$\boldsymbol{\mu} = g\,\mu_B\,\boldsymbol{S}, \tag{1.4}$$

acquires an additional potential energy of the SOI,

$$V = -\boldsymbol{\mu}\cdot\boldsymbol{B} = \frac{\mathbf{1}}{\mathbf{4\pi\epsilon_0}}\frac{Ze^2}{2m^2c^2r^3}\boldsymbol{L}\cdot\boldsymbol{S}, \tag{1.5}$$

where $S = \frac{\hbar}{2}$, is the spin of the electron. Hence, the energy levels of the electron with different spin orientations (spin-up and spin-down) will be shifted by, $+\mu B$ and $-\mu B$, respectively. (Dyakonov 2008; Flatte 2007) The consequence of this interaction enables optical spin orientation and detection; causes spin relaxation, and couples the charge and spin transport.

In order to develop semiconductor spintronics, several critical issues must be solved. These issues include injection of spin-polarized carriers in semiconductors, maintaining the injected spin polarization for a time long enough for the desired operations, the enhancement of spin lifetime, detection of spin-polarized carriers and even their coherence in nano-structures, transport of spin-polarized carriers across relevant length scales, and manipulation of both electron and nuclear spins on fast time scales. (Wolf 2001) Current efforts in designing and manufacturing spintronics involve two different approaches. The first approach is to find novel ways to generate and utilize spin-polarized currents in all-semiconductor structures. Although this approach is very challenging, it can be ultimately fully integrated with current semiconductor technology. The other approach is to further develop the giant-magneto-resistance -based technology by developing new materials with large spin polarizations in hybrid structure of metal and semiconductors. Since this approach is based on the mature giant-magneto-resistance technology, it is more likely to produce practical devices in the near future. (Wolf 2001; Sarma 2001)

1.3 Spin transport

As discussed in the previous section, one of the critical issues in semiconductor spintronics is spin transport, that is, an effective transport of spin-polarized carriers in semiconductor devices. This dissertation focuses the spin transport in semiconductors. In this section I will introduce previous experimental studies on spin transport in semiconductors.

Previously, both electrical and optical techniques have been developed by many groups and applied in studies of spin transport in semiconductors. I will first briefly discuss the electrical techniques, and then present details on optical studies since they are more relevant to the experiments discussed in this dissertation.

Several electrical techniques have been used to study spin transport in semiconductors. By measuring the interface resistance, the voltage drop across the ferromagnetic-metal/InAs interface which controls the spin transport in InAs is detected. (Hammar 2002; Yi 2005; Koo 2007) Similarly, the accumulations of spin-polarized electrons in bulk GaAs has been detected electrically. (Rougemaille 2008; Hammar 1999; Lou 2006; Lou 2007) Recently, spin transport in Silicon is also demonstrated. (Appelbaum 2007; Huang 2007; Jonker 2007) Spin-polarized electrons were injected electrically from an Iron (Fe) contact through an Al_2O_3 tunneling barrier into Si and circular polarization of the electroluminescence was observed which indicates a net spin polarized carrier transport in Si. (Jonker 2007)

In addition to these studies on bulk semiconductors, electrical injection of spin-polarized electrons in low dimension systems has also been demonstrated. A clear hysteretic tunnel magnetoresistance effect was observed in a double magnetic tunnel junction contains InAs quantum dots which indicates a spin transport through a single InAs quantum dot. (Hamaya 2007) Similarly, hysteretic magnetoresistance was observed in multi-walled carbon nanotubes as well. (Tsukagoshi 1999, Zhao 2002, Sahoo 2005, Nagabhirava 2006, Man 2006; Jensen 2005; Hueso 2007) More recently, spin transport was detected in graphene using electrical methods. Clear bipolar spin signals were observed in ferromagnetic contacts on top of graphene, indicating spin transport in micrometer-scale distance in single graphene layers. (Tombros 2007; Nishioka 2007; Chen 2007; Goto 2008; Han 2010)

In most studies with electrical techniques, the spin transport studied is in the drift-diffusion regime. Under typical conditions, the mean free path of electrons in semiconductors is on the order of 10-100 nm. Since it takes many scattering events to establish the steady-state drift-diffusion process, this process dominates devices with large length scale. When the size of the devices is comparable to the mean free path, electrons flow through the device with fewer or even no collisions. This is called ballistic transport, which plays a dominating role in nano-scale devices.

To study ballistic spin transport, it is necessary to use experimental techniques with temporal resolutions better than the mean-free time, and spatial resolutions better than the mean-free path. Optical techniques have the potential to achieve such high resolutions. With the ultrafast laser techniques, one can obtain a temporal resolution of less than 0.1 ps. Previously,

several optical techniques have been developed to study spin transport including spin-polarized photoluminescence, Faraday rotation, spin grating, and surface acoustic waves. In the following, I will discuss the principles and recent developments of these techniques.

In time-resolved photoluminescence, the recombination of the spin-polarized carriers emits certain circularly polarized photons. Therefore, the degree of circular polarization of the photoluminescence indicates the spin polarization of the carriers. (Flatte 2007; Hagele 1998; Sanada 2002; Sogawa 2000) By measuring photoluminescence as a function of time and space, one can study dynamics of spin-polarized carriers.

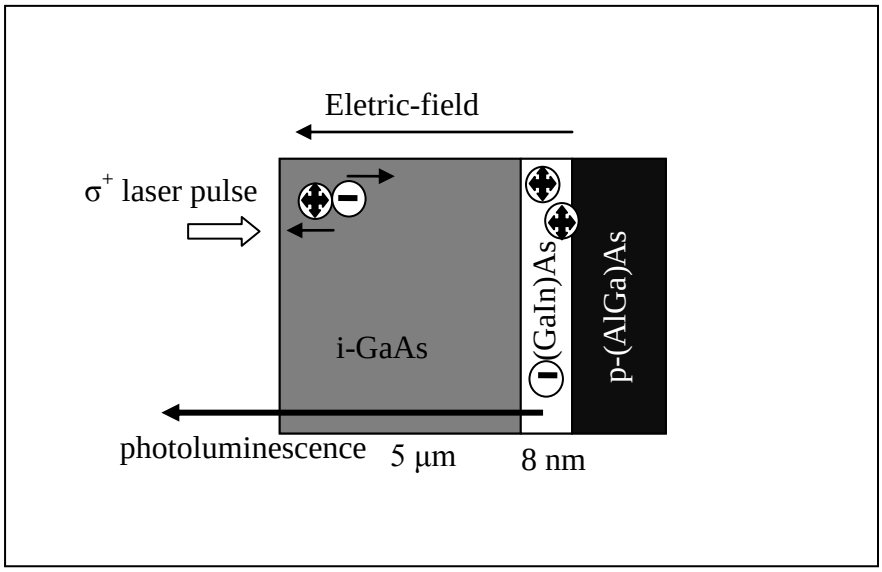

Figure 1.1: Spin transport studied by photoluminescence technique. An electric field is applied along the growth direction and drags the spin-polarized electrons excited at the sample surface by a circularly polarized laser pulse. The electrons drift towards the quantum well where they radiatively recombine with holes from the p-doped (AlGa)As barrier. (Hagele 1998)

Figure 1.1 shows the scheme of the first optical study on spin transport in semiconductors. A circularly polarized laser pulse with a photon energy larger than the GaAs bandgap creates electron-hole pairs close to the surface of a thick GaAs layer. The electrons have

a preferential spin orientation due to the optical selection rules. (Dyakonov and Perel 1984) They were dragged by an applied electric field through the GaAs layer. After that they are captured in a (GaIn)As quantum well, and recombine after energy relaxation. The quantum well photoluminescence has energy lower than the GaAs bandgap and, therefore, can be easily detected through the GaAs layer in the backward direction. The degree of polarization of the quantum well photoluminescence is proportional to the spin polarization of the electrons after drifting through the GaAs layer. (Hagele 1998)

Specifically, the sample shown in Fig. 1.1 consists of an intrinsic GaAs (i-GaAs) layer, and two quantum wells. The optical excitation is achieved by using a pulsed laser. The two circular components of the photoluminescence are detected with a spectral and temporal resolution of 0.5 nm and 10 ps, respectively, by a streak camera with a two-dimensional readout. The left and right circularly polarized transient luminescence is measured at an applied voltage of 2 V in the forward direction and a spot size of 100 μm. The spin polarization is measured to be 30% and the spin polarization decays on a time scale of 1 ns after a transport of 4 μm. The spin transport strongly depends on the applied electric field.

Another optical technique to study spin transport is the Faraday/Kerr rotation. In this technique, the index of refraction is measured, rather than the absorption coefficient. The spin-polarized carriers cause the index of refraction of the material to be different for the two circular polarizations of the light. When a linearly polarized pulse transmits through or reflects from the sample, the two circularly components will receive different phase changes, and therefore the output light will have a linear polarization that is rotations with respect to the incident polarization. This rotation is proportional to the spin density, and can be sensitively detected with a crossed polarizer or an optical bridge. Spatially resolved Faraday/Kerr rotation measurements can be used to study transport of packets of spin-polarized carriers in semiconductors (Kikkawa 1997) or from one semiconductor material to another (Malajovich 2000; Malajovich 2001).

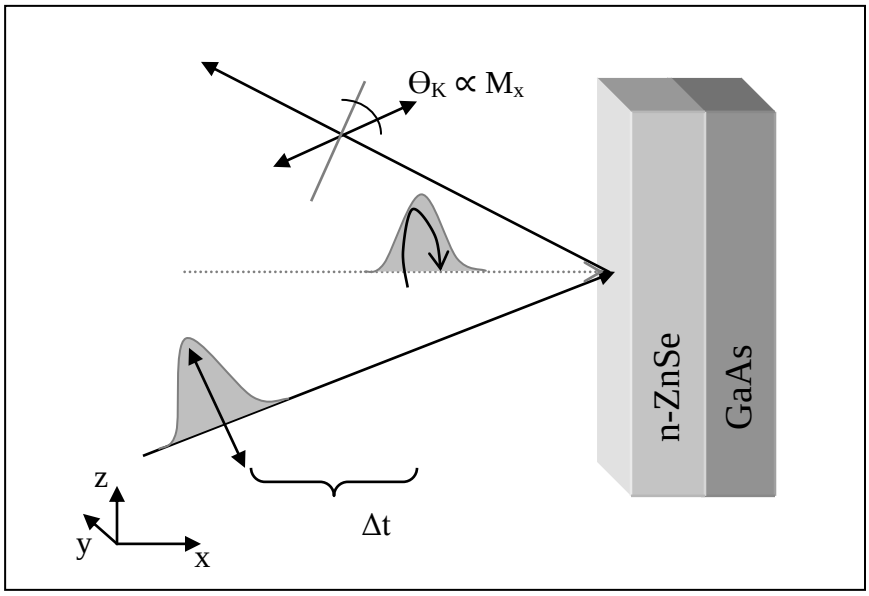

Figure 1.2: Geometry of the spin transport studies in n-type ZnSe/GaAs heretostructures using Kerr rotation. (Malajovich 2000)

Figure 1.2 shows the experimental geometry of a Kerr rotation measurement. The circularly polarized pump pulse has photon energy less than the bandgap of ZnSe, hence transmits through the ZnSe layer with almost no absorption. The pump photons are then absorbed by the GaAs layer, exciting spin-polarized carriers in GaAs. These carriers can move to the ZnSe layer. A linearly polarized probe pulse is used to measure Kerr rotation from the ZnSe surface, hence monitors the spin-polarized carriers that moved from the GaAs layer to the ZnSe layer. (Malajovich 2000) The results of this experiment showed a spin transport from GaAs to ZnSe without applying a magnetic field.

In addition to studies of spin-polarized carriers injecting optically, the Faraday/Kerr rotation techniques have also been used to study spin accumulation caused by the spin Hall effect (SHE). (Kato 2004; Sih 2005; Sih 2006; Stern 2007; Stern 2008) Similar to the charge accumulation at the sample edges induced by a charge current, the spin current generated in the SHE is expected to cause spin accumulation at the sample edges. (Kato 2004)

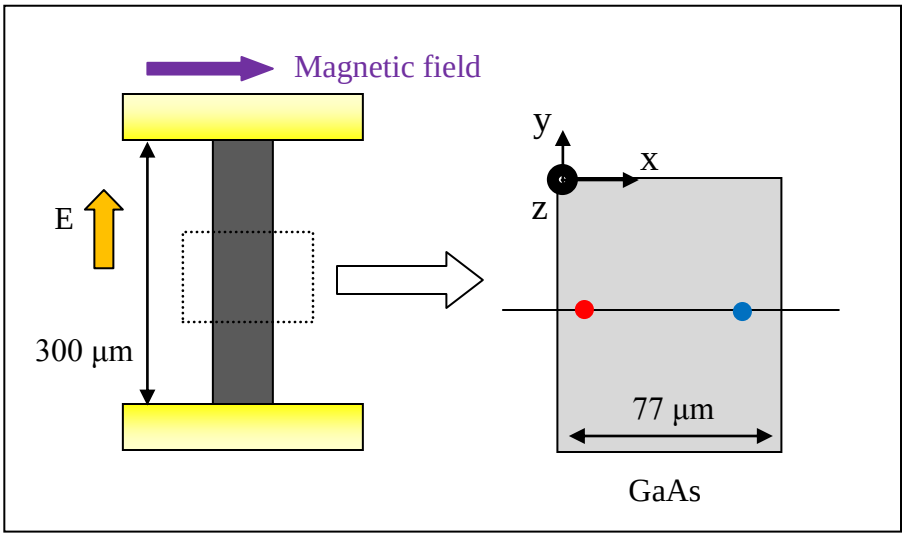

Figure 1.3: Geometry of the Kerr-rotation measurement of the SHE. Right: GaAs sample. The red and blue dots in the Figure show the spin-up and spin-down electron accumulation due to the SHE. Left: the device structure. (Kato 2004)

Figure 1.3 shows the configuration of using the scanning Kerr microscopy to study the SHE in GaAs. (Kato 2004) A charge current is produced along the $\hat{y}$ direction in an n-doped GaAs wafer by applying a DC voltage. Due to the SHE, a pure spin current (PSC) is expected to be generated along the $\hat{x}$ direction with the spin orientation along $\hat{z}$ direction. Such a PSC is uniformly distributed on the wafer, and hence caused spin accumulation at the two edges of the sample. A linearly polarized probe beam along the $\hat{z}$ direction is incident normal to the sample. The polarization of the reflected beam is rotated by an angle that is proportional to the net magnetization along the laser propagation direction induced by the spin accumulation. Therefore, by scanning the laser spot, the spatial distribution of the spin accumulation in the samples can be imaged. (Kato 2004) Result of this experiment shows accumulations of spin-down electrons at $x = -35$ μm and spin-up electrons at $x = -35$ μm. This confirmed the existence of the SHE. Furthermore, they found that an increased electric field causes larger spin accumulation and ultimately the spin accumulation saturates as the spin relaxation time drops. (Kato 2004)

Similar to the Faraday/Kerr rotation, circular dichroism is another optical method to study spin transport. (Zhao 2007, Ruzicka 2008) Some of my experiments were performed with this technique, and therefore the details will be explained later in chapter 4.

Another method of studying spin-transport is transient spin gratings.(Cameron 1996; Carter 2006) In this method, two laser pulses (pumps, k_A and k_B beams in Fig. 1.4) with the same photon energy near the bandgap are coincident on the sample from different directions, exciting electron-hole pairs. For collinearly polarized pumps, interference modulates the intensity across the excitation spot, generating a grating of carrier density. The grating period is determined by the angle between the pump beams and the wavelength. For cross-polarized pumps, the net polarization of the total beam is modulated between right and left circular polarizations across the laser spot. This excites carriers with alternating spin polarizations but a uniform density, as illustrated in Fig. 1.5.

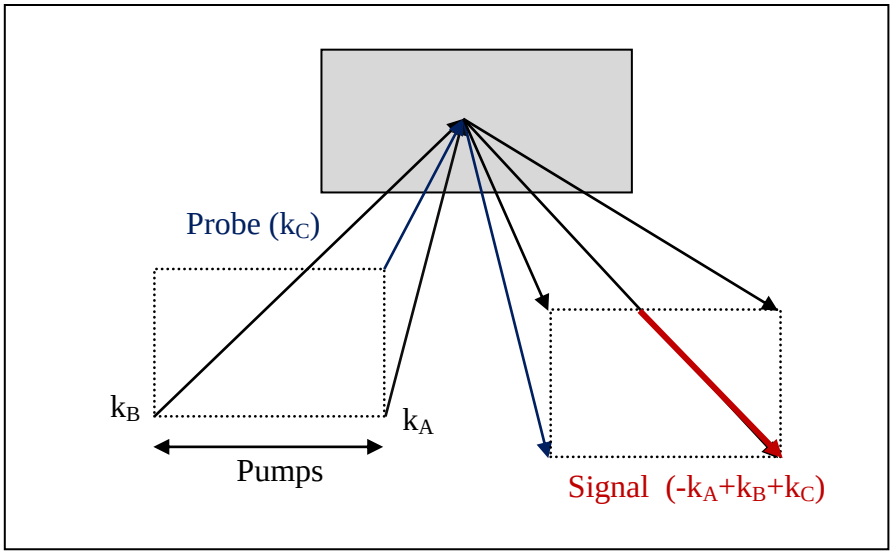

Figure 1.4: Geometry of the transient grating experiment. (Carter 2006)

In this technique, the excited spin grating is detected by observing the diffraction of a probe beam (K_c in Fig 1.4) off the grating. As shown in Fig. 1.4, the reflections of the two pump beams and the probe beam are at the three corners of a rectangle, with the diffracted beam at the

forth corner. (Carter 2006) For collinear experiments, both pumps are horizontally polarized, while for cross-linear experiments, pump A (B) has horizontal (Vertical) polarization. The probe is vertically polarized. The diffracted beam is detected by an amplified photodiode. Results of this experiment show a slower spin diffusion of excess electrons than the diffusion of the unpolarized carriers. This is consistent with, a spin Coulomb drag effect. (Carter 2006)

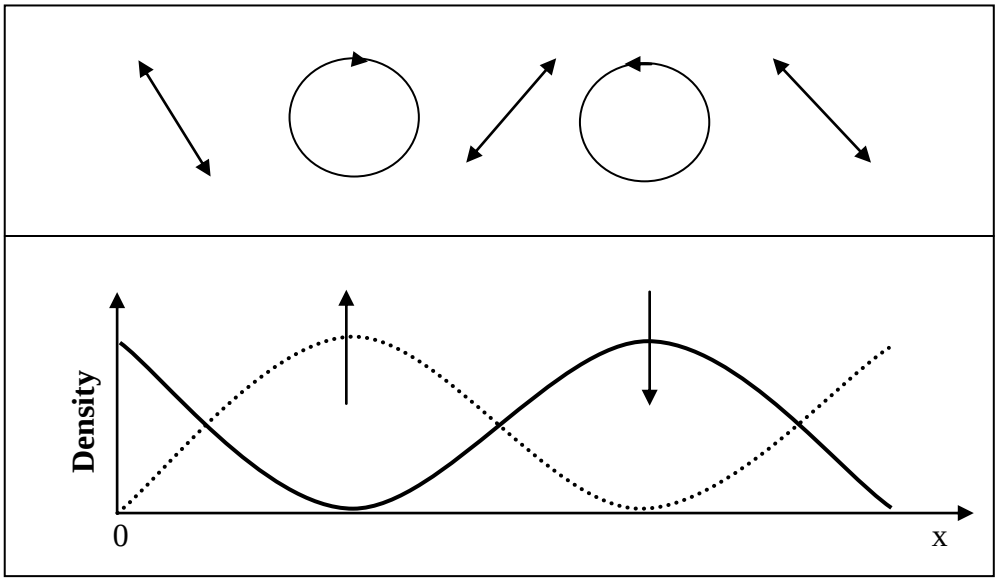

Figure 1.5: Upper panel: the polarization modulation produced when the two cross-linearly polarized laser beams interfere. Lower panel: density of spin-up and spin-down electrons excited by a polarization grating shown in the upper panel. (Cameron 1996)

Very recently, spin transport carried by surface acoustic waves has been studied by optical techniques. (Sogawa 2001; Stotz 2005; Couto 2007) Figure 1.6, shows spin transport in undoped (110) GaAs samples using mobile piezoelectric potentials produced by surface acoustic waves. (Couto 2000). As shows in Fig. 1.6, the acoustic waves along the $\hat{x}$ and $\hat{y}$ directions are generated by focusing inter-digital transducers (IDT in the figure). A laser beam is focused to a small spot G, and injects spin-polarized carriers. When the surface acoustic waves propagate

through G, it carries the spin-polarized carriers with it. The evolution of the packets of spin-up and spin-down electrons can be monitored by a gated charge couple device camera, which records the photoluminescence from the electron-hole recombination along the transport path. (Couto 2000).

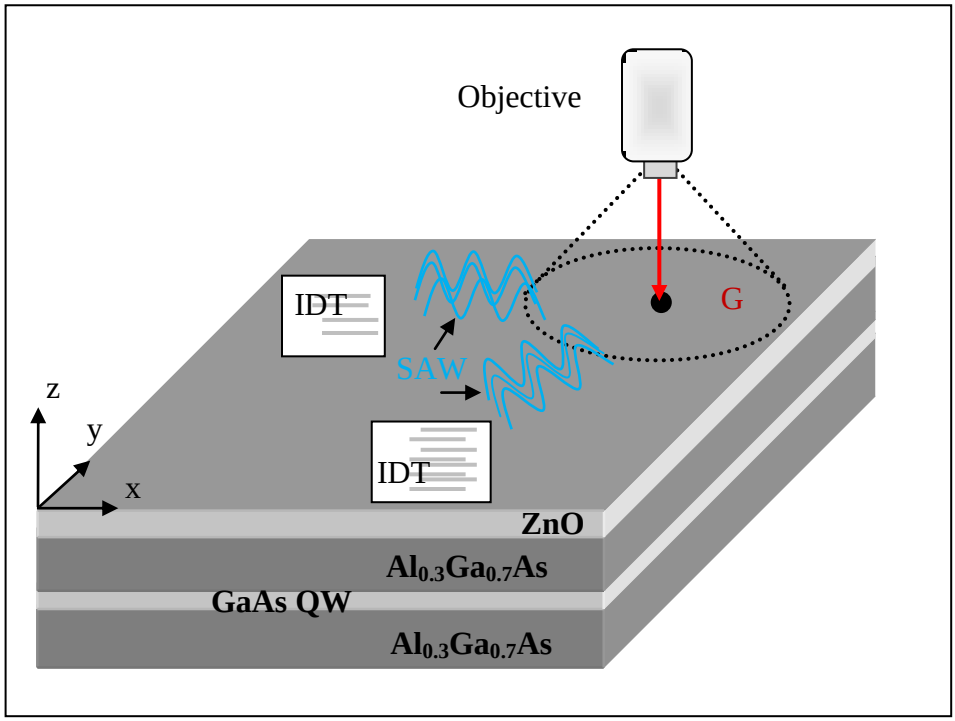

Figure: 1.6: Sketch of the experimental setup. Spin packets photoexcited in the GaAs quantum wells by a laser focused at spot G are transported by surface acoustic waves beams along the $\hat{x}$ or $\hat{y}$ directions. The acoustic beams are generated by IDTs deposited on the sample surface. (Couto 2000)

In the experiments, the surface acoustic waves induced transport of the spin packets are recorded 12.2 ns after the laser pulse and the spin packet has been transported ~30 μm away from the G point. The difference between the left and right circularly polarized photoluminescence components gives evidence of a net spin transport. While the photoluminescence intensity reduces with propagation distance, the width of the carrier packet broadens only slightly during the transport. The packet width exceeds the acoustic wavelength

which indicates that the surface acoustic wave potential is not sufficiently strong to transport all photoexcited carriers within a single surface acoustic waves cycle.

As described above, significant progress has been made in optical studies of spin transport. However, one critical challenge of these techniques is that, the spatial resolution is limited to the order of micrometer. In these techniques, the spin transport is studied by tracking the position of spin packets as a function of time. Spin transport on length scales smaller than the laser spots cannot be accurately measured. This dissertation is devoted to solve this issue by using two approaches. First, a derivative detection scheme will be used to overcome the resolution problem and obtain a sub-nm resolution. Second, new second harmonic generation (SHG) techniques will be used to directly sense the velocity of the electrons. In this scheme, high spatial resolution is not required.

The structure of the dissertation is shown in Fig. 1.7. Chapter 2, outlines the fundamentals of carrier transport in semiconductors, with discussions on ballistic transport and drift-diffusion, as well as charge and spin transport. In chapter 3, the principle of the quantum interference and control (QUIC) technique is discussed. Then the configurations to inject different types of currents are discussed followed by a discussion of the experimental setup. Chapter 4 is devoted to the pump-probe technique that we used to study the carrier and spin transport. I will first discuss the principles of this technique on detecting carrier and spin densities. I will then discuss how to achieve high temporal and spatial resolution. In chapter 5, the experimental results on ballistic transport obtained by using QUIC and the pump-probe technique are presented. First, the observation of spin-polarized charge current (SPCC) in GaAs is discussed. Second, the experimental results of the intrinsic inverse SHE in GaAs quantum wells are presented. The last topic of this chapter is the observation of PSC in Ge. Chapter 6 is devoted to using nonlinear optics, particularly the SHG techniques to study carrier transport in semiconductor nanostructures. The principles of both intrinsic and extrinsic SHG are discussed. The SHG in the bulk structure and at the surface or the interface layer is explained. In chapter 7, I will present our experimental results on using the SHG techniques to study carrier dynamics, including PSC, PCC, and carrier densities. I will summarize the results and discuss some future directions in chapter 8.

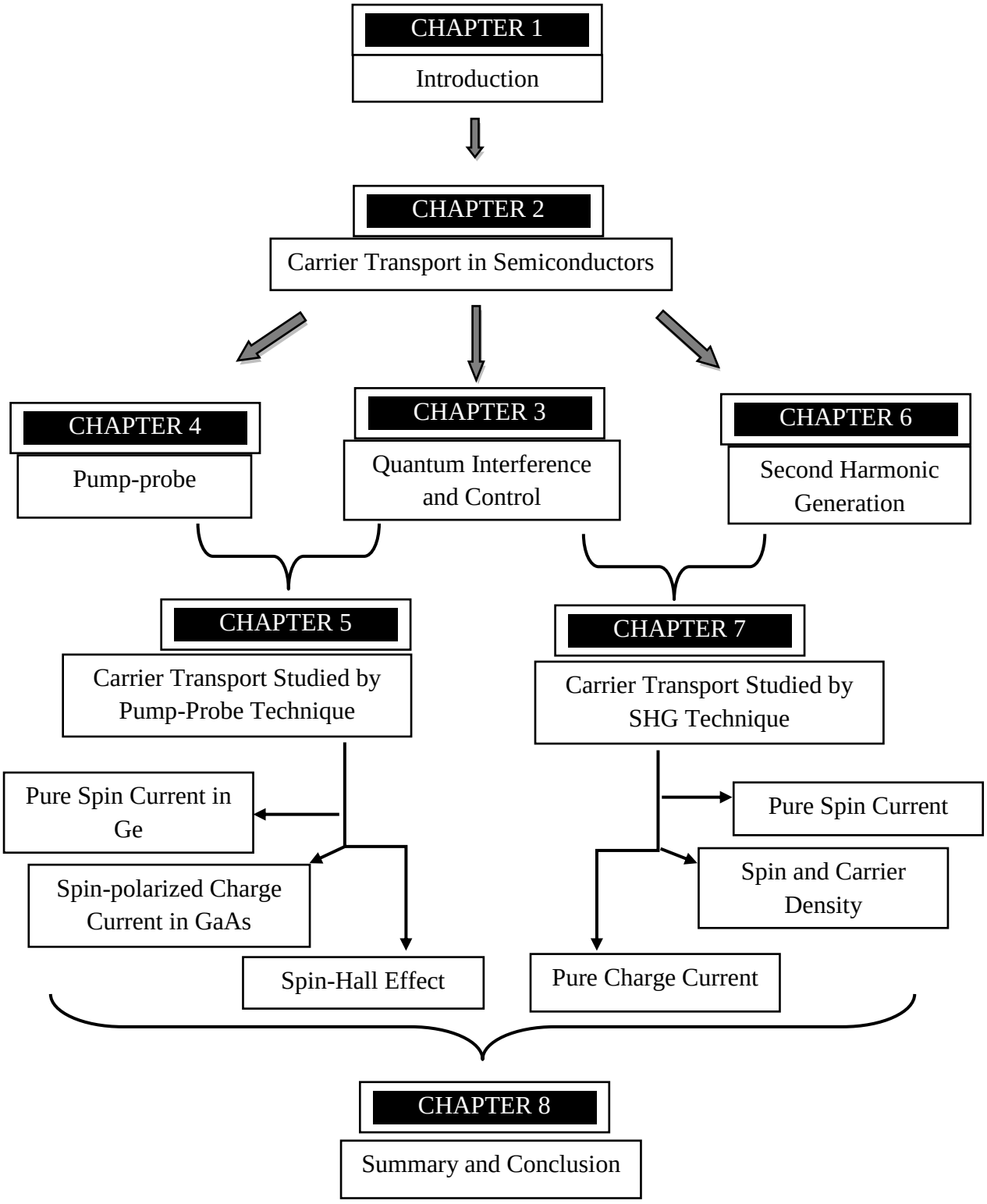

Fig: 1.7: The structure of the dissertation.

Chapter 2: Carrier transport in semiconductors

This dissertation is about optical studies of carrier transport in semiconductors, with emphasis on spin transport. Therefore, in this chapter, I will provide a brief discussion on the concepts of different types of carrier transport. Depending on the driving force, carrier transport can be drift or diffusion, driven by an externally applied electric field or a density gradient, respectively. These transport processes will be discussed in Sec. 2.1. According to the actual physical quantities that are moved, carrier transport can be divided to pure charge transport, pure spin transport, or transport of both charge and spin. Different types of transport will be discussed in Sec,2.2. In Sec. 2.3, I will discuss different regimes of transport, and emphasizes the scattering-free ballistic transport occurs on small length scales, in comparison to drift-diffusion of thermalize carriers on larger length scales.

2.1 Drift and diffusion transport

Upon application of an electric field in a semiconductor, the electrostatic force causes carriers to move. They first accelerate and then reach a steady velocity, known as drift velocity, due to the scattering with impurities. Figure 2.1(a) shows the drift process. The resulting current density, $\boldsymbol{J}_{drift}$ is proportional to the applied electric field, $\boldsymbol{E}$. As electrons and holes move in opposite directions,

$$\boldsymbol{J}_{drift} = e\left(p\mu_p + n\mu_n\right)\boldsymbol{E}, \tag{2.1}$$

where e, $\mu_{n(p)}$ and $n(p)$ are the charge of one electron, mobility of electrons (holes) and the density of electrons (holes), respectively.

Diffusive motion of carriers is driven by a density gradient, as illustrated in Fig 2.1(b). This transport mechanism is due to the random motion of carriers caused by their thermal energy. The resulting current density is,

$$\boldsymbol{J}_{diffusion} = -e(D_n\boldsymbol{\nabla}n + D_p\boldsymbol{\nabla}p), \tag{2.2}$$

where $D_{n(p)}$ and $\nabla n(p)$ are the diffusion coefficients of the electrons (holes) and the density gradient of the electrons (holes), respectively. (Kittel 1996)

As the effective mass of the electrons is smaller than the holes, the mobility of electrons is usually larger than the holes. Hence, electrons usually make a larger contribution to the overall current in undoped samples. In the rest of the dissertation, the carrier motion is usually referred to the motion of electrons in the conduction band (CB). The motion of holes is neglected unless it is specified.

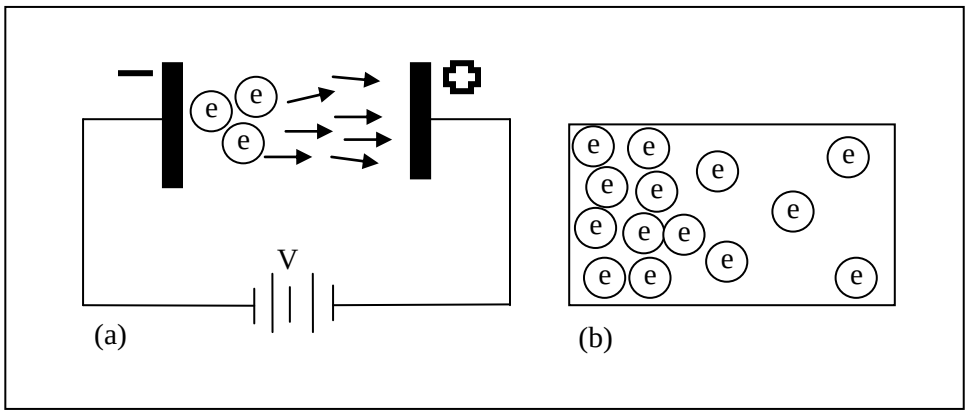

Figure 2.1 Carrier transport in semiconductors: (a) the applied voltage drives the electrons - drift current and (b) electrons move from high density area to low density area without a driving force - diffusion current.

2.2 Charge and spin currents

An electron in the CB of a semiconductor has an angular momentum or spin of $\pm\frac{\hbar}{2}$, in addition to its mass and charge. A SPCC consists of unequal numbers of spin-up and spin-down electrons flowing along the same direction. As there is a net carrier movement, there is a charge current. Since the moving carriers are spin-polarized, there is also a spin current. Figure 2.2 shows a cartoony picture of the SPCC.

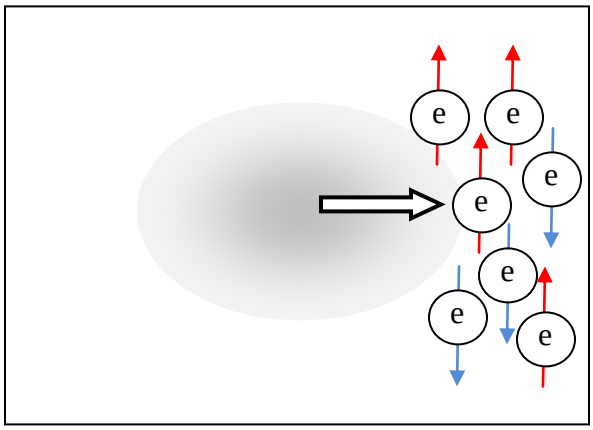

Figure 2.2: Schematic of real-space motion of electrons in a SPCC. Unequal numbers of spin-up and spin-down electrons move in the same direction.

Depending upon the spin polarizations, electron transport can produces different types of current. A flow of spin-unpolarized carriers produces a PCC, since there is no net spin transport. If there are more electrons of $+\frac{\hbar}{2}$ compared to the $-\frac{\hbar}{2}$ or vice versa, the carrier system is spin polarized. A flow of such carriers is called a SPCC. Moreover, if there are an equal number of electrons with opposite spin orientation moving in opposite directions with the same speed, the flow is called a PSC, since there is no net charge flow. In the next sections, I will discuss these currents in detail.

2.2.1 Pure charge current

A PCC consists of an equal number of spin-up and spin-down electrons moving along the same direction. As the numbers of spin-up and spin-down electrons are equal, there is no net spin transport in the system. Thus the PSC is a net flow of charge, as shown in Fig. 2.3.

The density of PCC, $\boldsymbol{J}$, can be expressed as

$$\boldsymbol{J} = -eN\langle \boldsymbol{v} \rangle, \tag{2.3}$$

where N and $\langle \boldsymbol{v} \rangle$ are the density and the average velocity of the electrons.

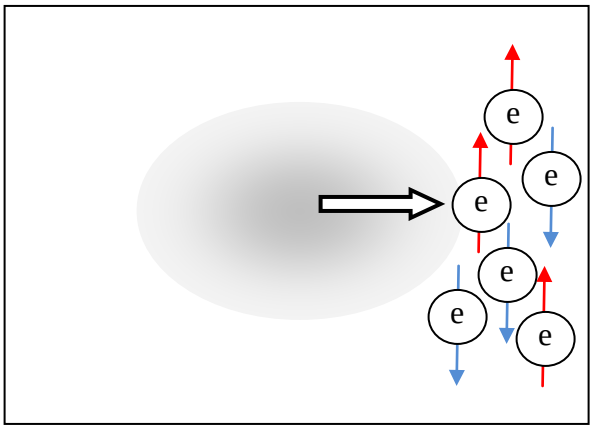

Figure 2.3: Schematic of real-space motion of electrons in a PCC. Equal numbers of spin-up and spin-down electrons move in the same direction. There is no net spin transport.

2.2.2 Pure spin current

A PSC consists of an equal number of spin-up and spin-down electrons moving along opposite directions, with the same speed. Since the charge currents carried by the two spin systems are equal in magnitude but opposite in sign, they cancel each other. Hence, a PSC does not involve net charge transport. It is a net flow of spin, as shown in Fig. 2.4.

The density of a PSC, $\boldsymbol{K}$, can be defined as

$$\boldsymbol{K} = \frac{\hbar}{2} N^{\uparrow} \langle \boldsymbol{v}^{\uparrow} \rangle + \frac{-\hbar}{2} N^{\downarrow} \langle \boldsymbol{v}^{\downarrow} \rangle , \tag{2.4}$$

where $\hbar$ is the Planck constant, $N^{\uparrow(\downarrow)}$ and $\langle \boldsymbol{v}^{\uparrow(\downarrow)} \rangle$ are the density and the average velocity of the spin-up (spin-down) electrons.

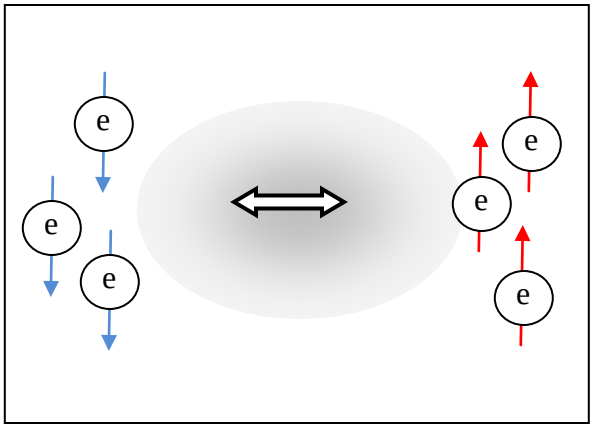

Figure 2.4: Schematic of real-space motion of electrons of PSC. An equal number of electrons with spin-up and spin-down move in opposite direction. There is no net charge transport.

2.3 Ballistic transport and drift-diffusion

In Sections 2.1 and 2.2, I have discussed two aspects of carrier transport, the driving force (drift versus diffusion) and the physical quantities moved (charge versus spin). Based on the microscopic transport mechanism, carrier transport can also be classified as ballistic and drift-diffusion processes.

The carrier transport in the scattering-free regime is called the ballistic transport. This is an important type of transport in nano-scale devices. As the size of devices continues to shrink down and gets smaller than the mean free path of electrons, the carrier transport inside such devices does not involve many phonon or impurity scatterings. On the other hand, in the carrier transport over macroscopic distance, electrons travel in a drift manner and experience many collisions. Therefore, in bulk semiconductor structures, the carrier transport is a drift-diffusion process described by the macroscopic quantities including the mobilities and the diffusion coefficients. Obviously, depending on the physical quantities involved, both the ballistic current and the drift-diffusion current can be PCC, PSC, and SPCC, as discussed in Sec. 2.2.

In this chapter, I have discussed the fundamental concepts of carrier transport in semiconductors and introduced three different aspects of carrier transport. In the next chapter, I will discuss how to use optical techniques to inject different types of currents.

Chapter 3

Quantum interference and control technique to inject ballistic currents

In this chapter, I will first discuss optical injection of spin-polarized carriers. I will then discuss the principles of the quantum interference and control technique as the current injection method we used in our experiments. Then, I will introduce different experimental configurations to inject pure spin current, pure charge current, and spin-polarized charge current via quantum interference and control technique. Finally, I will describe our experimental setup to achieve these current injections.

3.1 Optical injection of spin-polarized carriers

To understand the principle of the QUIC technique that we used in our experiments to inject charge and spin currents, it is beneficial to first, discuss the optical injection of spin-polarized carriers. This process has been generally applied to study spin dynamics such as spin relaxation and spin transport in spintronics. (Wolf 2001; Zutic 2004) In the process of interband absorption of a photon in a semiconductor, an electron in the CB and a hole in the valence band (VB) are generated. The total spin of the electron-hole pair equals to the angular momentum of the photon absorbed. A photon with right or left circular polarization has a projection of the angular momentum in the direction of the wavevector that is equal to $+\hbar$ or $-\hbar$, respectively. A linearly polarized photon is in the superposition of these two states. The angular momentum of the circularly polarized photon is distributed between the electron and the hole according to the selection rules determined by the band structure of the semiconductor. (Meier and Zakharchenya 1984)

Figure 3.1 shows the direct absorption of both left and right- circularly polarized photons in semiconductors. According to spin selection rules, the quantum number can only be changed by $\Delta m = \pm 1$ during direct transitions from the VB to the CB. Therefore, for right-circularly polarized light (+1), only direct transitions from the light hole-VB $\left(m_j = -\frac{1}{2}\right)$ and the heavy

hole-VB$\left(m_j = -\frac{3}{2}\right)$ to the CB $\left(m_j = -\frac{1}{2}\right)$ are allowed and all the other transitions, for example from the other heavy hole-VB $\left(m_j = +\frac{3}{2}\right)$ and light hole-VB $\left(m_j = +\frac{1}{2}\right)$ to the CB are not allowed.

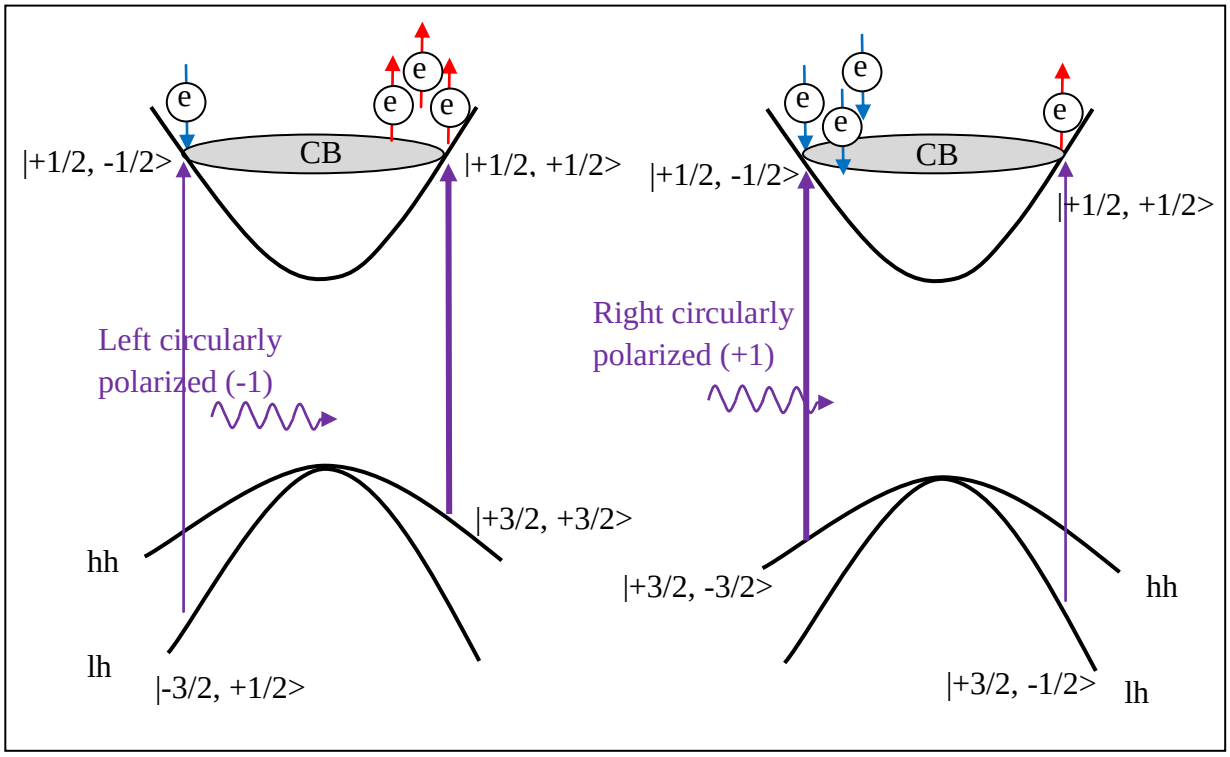

Figure 3.1: Schematic of the optical transitions between levels of the heavy hole-VB and the light hole-VB with $\left(m_j = \pm\frac{3}{2}\right)$ and $\left(m_j = \pm\frac{1}{2}\right)$ during an absorption of a left (-1) and right (+1) circularly polarized photons. According to the selection rules, left-circularly polarized light excite more spin-up electrons (left band structure) and right-circularly polarized light (right band structure) create more spin-down electrons. It is assumed that the photon energy is low enough to avoid exciting electrons from the split-off band to the CB. (Meier and Zakharchenya 1984)

Similarly, for left- circularly polarized light (-1), only direct transitions from the light hole-VB $\left(m_j = +\frac{1}{2}\right)$ and the heavy hole-VB $\left(m_j = +\frac{3}{2}\right)$ to the CB $\left(m_j = -\frac{1}{2}\right)$ are allowed and

all the other transitions for example from the other heavy hole-VB $\left(m_j = -\frac{3}{2}\right)$ and light hole-VB $\left(m_j = -\frac{1}{2}\right)$ to the CB are not allowed.

Therefore, owing to the spin selection rules, the direct transitions from the heavy hole-VB will produce electrons with the opposite spin of those from the light hole-VB. However, the heavy hole-VB to the CB single-photon transition is three times stronger than the light hole-VB to the CB, leading to 3:1 ratio of spin-up and spin-down in the CB electrons. (Meier and Zakharchenya 1984) To calculate the spin-polarization of this population, we can use the relation,

$$Spin\ polarization = \left[\frac{N^{\uparrow} - N^{\downarrow}}{N^{\uparrow} + N^{\downarrow}}\right] \times 100\ \%. \qquad (3.1)$$

Substituting, $N^{\uparrow} = 3N^{\downarrow}$, in Eq. (3.1), the ratio 3:1 leads to a 50% spin-polarization.

3.2 Quantum interference and control

Although a circularly polarized light can excite spin-polarized carriers, in a typical optical interband excitation, equal numbers of carriers are injected with opposite momenta, and therefore move oppositely, resulting in no net current. The QUIC technique is developed to solve this problem and inject currents optically. In this scheme, the sample is excited with laser pulses with angular frequencies of ω and 2ω, respectively. Under the condition of $\hbar\omega < E_g < 2\hbar\omega$, carrier excitation from the VB to the CB can be done by one-photon absorption of the 2ω pulse and two-photons absorption of the ω pulse. Acting alone, each pulse can inject carrier and spin densities in the CB and the VB. When both pulses are present simultaneously, quantum interference between the two transition amplitudes occurs. By controlling the relative phase between ω and 2ω pulses, constructive and destructive interferences can be arranged in k state with opposite signs. This causes asymmetric distribution of carriers in k space, leading to current.

In the following, I will describe a brief theory on QUIC. More detailed theoretical treatments can be found in the following references. (Bhat 2000; Stevens 2003)

Generally, the interband transition amplitude,

$$a_{cv}(\boldsymbol{k}) \propto \langle \psi_{c\boldsymbol{k}} | \boldsymbol{E} \cdot \boldsymbol{p} | \psi_{v\boldsymbol{k}} \rangle, \tag{3.2}$$

where $\psi_{c(v)k}$ is the wavefunction of the electron in the conduction (valence) band. When the system is driven by the two optical fields, the total transmission amplitude can be written as the sum of the two individual transition amplitudes driven by the ω and 2ω fields.

$$a_{cv}(\boldsymbol{k}) = a_{cv}^{2\omega}(\boldsymbol{k}) + a_{cv}^{\omega}(\boldsymbol{k}). \tag{3.3}$$

The total population injection rate,

$$\dot{n} \propto \sum_{c,v,\boldsymbol{k}} | a_{cv}^{2\omega}(\boldsymbol{k}) + a_{cv}^{\omega}(\boldsymbol{k})|^2, \tag{3.4}$$

which can be expended to,

$$\dot{n} \propto \sum_{c,v,\boldsymbol{k}} \{ |a_{cv}^{2\omega}(\boldsymbol{k})|^2 + |a_{cv}^{\omega}(\boldsymbol{k})|^2 + a_{cv}^{2\omega}(\boldsymbol{k})^* a_{cv}^{\omega}(\boldsymbol{k}) + a_{cv}^{2\omega}(\boldsymbol{k}) a_{cv}^{\omega}(\boldsymbol{k})^* \}. \tag{3.5}$$

The four terms in Eq. (3.5) can be recognized as,

$$\dot{n} = \dot{n}_{2\omega} + \dot{n}_{\omega} + \dot{n}_{I}, \tag{3.6}$$

where $\dot{n}_{2\omega}$and $\dot{n}_{\omega}$ are the individual injection rates of the pulses, and

$$\dot{n}_{I} \propto \sum_{c,v,\vec{\boldsymbol{k}}} a_{cv}^{2\omega}(\boldsymbol{k})^* \, a_{cv}^{\omega}(\boldsymbol{k}) + c.c., \tag{3.7}$$

the quantum interference term. Using the individual transition amplitude of ω,

$$a_{cv}^{\omega}(\boldsymbol{k}) \propto |E_{\omega}|^2 e^{i2\phi_{\omega}}, \tag{3.8}$$

and 2ω,

$$a_{cv}^{2\omega}(\boldsymbol{k}) \propto |E_{2\omega}| e^{i\phi_{2\omega}}, \tag{3.9}$$

it can be shown that (Bhat 2000; Stevens 2003),

$$a_{cv}^{2\omega}(\boldsymbol{k})^* a_{cv}^{\omega}(\boldsymbol{k}) \propto |E_{2\omega}||E_{\omega}|^2 e^{i(2\phi_{\omega} - \phi_{2\omega})}. \tag{3.10}$$

According to Eqs. (3.7) and (3.10), the QUIC term, $\dot{n}_I$, explicitly depends on the phase difference of the optical fields. Therefore, this is a coherent control technique. (Bhat 2000; Stevens 2003; Hubner 2003)

3.3 Injection of ballistic currents

3.3.1 Pure spin currents

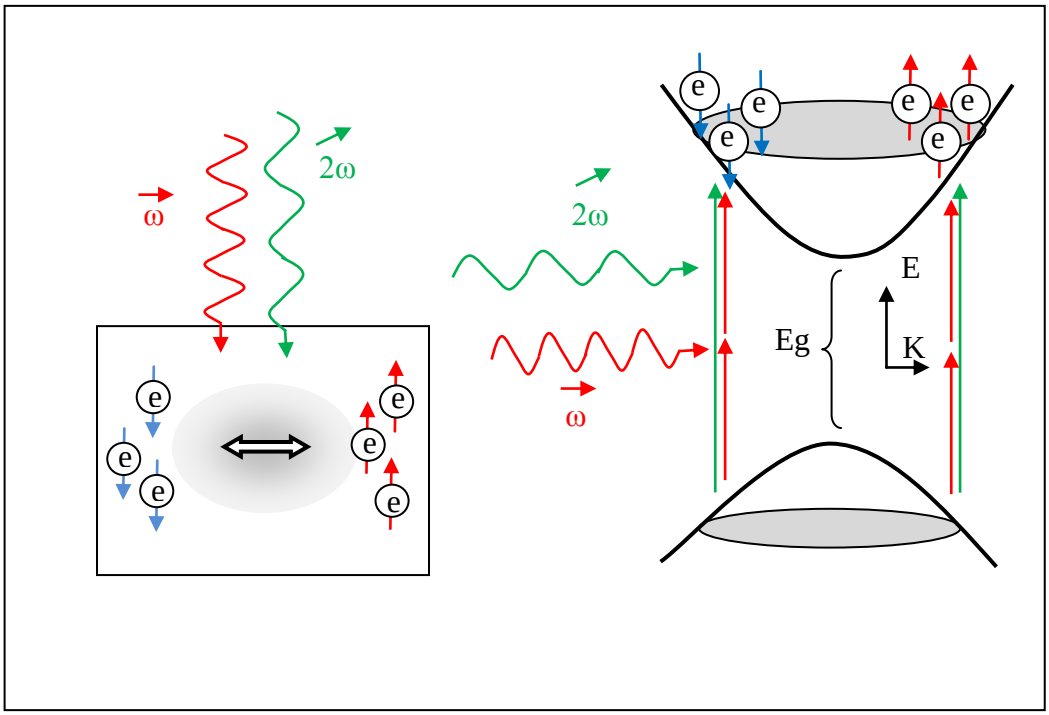

Figure 3.2 Schematic drawings of PSC injection. The left panel is a real-space drawing of the orthogonally polarized pulses, ω and 2ω, generating a PSC. The right panel shows the k-space distribution of carriers in the PSC. The charge is distributed symmetrically while the spin is distributed asymmetrically in the k space. Equal numbers of spin-up and spin-down electrons are injected with velocities in $+\hat{x}$ and $-\hat{x}$ directions.

As explained above, the QUIC technique can be used to optically inject a spin current without an associated charge current (Stevens 2003). This is achieved when the polarizations of the ω ($\hat{x}$ direction) and 2ω ($\hat{y}$ direction) pulses are orthogonal. In this configuration, spin-up electrons are excited with an average velocity along $\hat{x}$- direction, while an equal number of spin-down electrons are excited with an average velocity in the opposite (-$\hat{x}$) direction. The average velocities are proportional to the relative phase, $\Delta\phi = 2\phi_{\omega} - \phi_{2\omega}$,

$$\langle \boldsymbol{v}^{\uparrow} \rangle = -\langle \boldsymbol{v}^{\downarrow} \rangle \propto \cos \Delta\phi. \tag{3.10}$$

The left-panel of Fig. 3.2 is a real-space diagram showing the orthogonally polarized pump pulses, (ω and 2ω), generating a PSC in the semiconductor sample. In the right paneEl of Fig. 3.2, the k-space distribution of carriers of a PSC is shown. Under the condition of $\hbar\omega < E_g < 2\hbar\omega$, equal numbers of spin-up (+$\hat{z}$ direction) and spin-down electrons (–$\hat{z}$ direction) are injected with velocities in +$\hat{x}$ and –$\hat{x}$ directions, respectively.

3.3.2 Pure charge currents

Similarly, the QUIC technique can be used to inject a PCC. When the polarizations of both ω and 2ω are parallel ($\hat{x}$ direction), a PCC will be injected along $\hat{x}$ direction with an average velocity of the electrons that is proportional to the sine of the relative phase,

$$\boldsymbol{v} \propto \sin \Delta\phi. \tag{3.11}$$

Hence, the magnitude of the PCC is controlled by the $\Delta\phi$.

The left panel of Fig. 3.3 shows a real-space diagram of the parallelly-polarized pump pulses, ω and 2ω injecting a PCC in the sample. Both spin-up and spin-down electrons move in the same direction. In the right-panel of Fig. 3.3, the k-space distribution of carriers for a PCC is shown. Equal numbers of spin-up electrons (spin orientation along +$\hat{z}$) and spin-down electrons (spin orientation along –$\hat{z}$) are injected with velocities in +$\hat{x}$ direction.

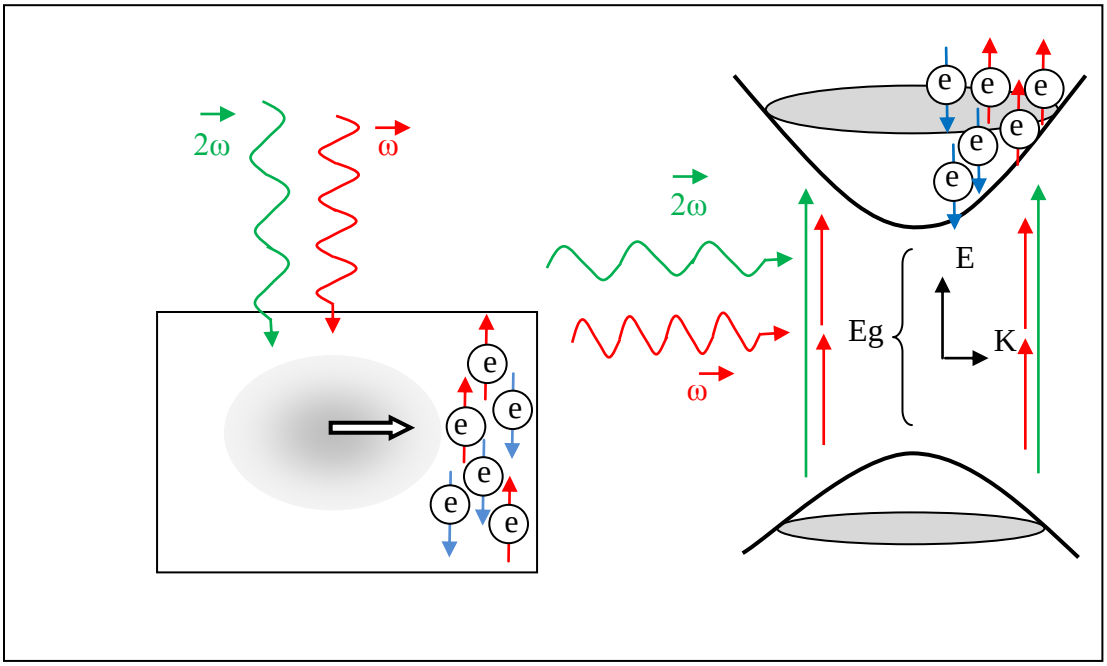

Figure 3.3: Schematic drawings of PCC injection. Left panel shows a real-space drawing of the parallel polarized pulses, ω and 2ω, generating a PCC. Right panel shows a k-space distribution of carriers in a PCC. The carriers are distributed asymmetrically but the spin is distributed symmetrically in the k space.

3.3.3 Spin polarized charge current

When both ω and 2ω pulses are circularly polarized (for example, right-hand circularly polarized, $\hat{\sigma}^{+} = \frac{\hat{x}+i\hat{y}}{\sqrt{2}}$), a SPCC is injected in the direction of $\hat{m} = \sin\Delta\phi\,\hat{x} + \cos\Delta\phi\,\hat{y}$. Unlike the injection of the PSC and PCC, the relative phase does not control the magnitude but changes the direction of the current.

The left panel in Fig. 3.4 is a real-space diagram showing the circularly-polarized pump pulses, ω and 2ω generating a SPCC in the sample. Upon injection, all the carriers move in one direction. In right-panel of Fig. 3.3 is a k-space distribution of carriers for a SPCC is shown. An unequal number of spin up electrons (spin along $+\hat{z}$ direction) and spin down electrons (spin along $-\hat{z}$ direction) are injected with velocities in +x̂ direction.

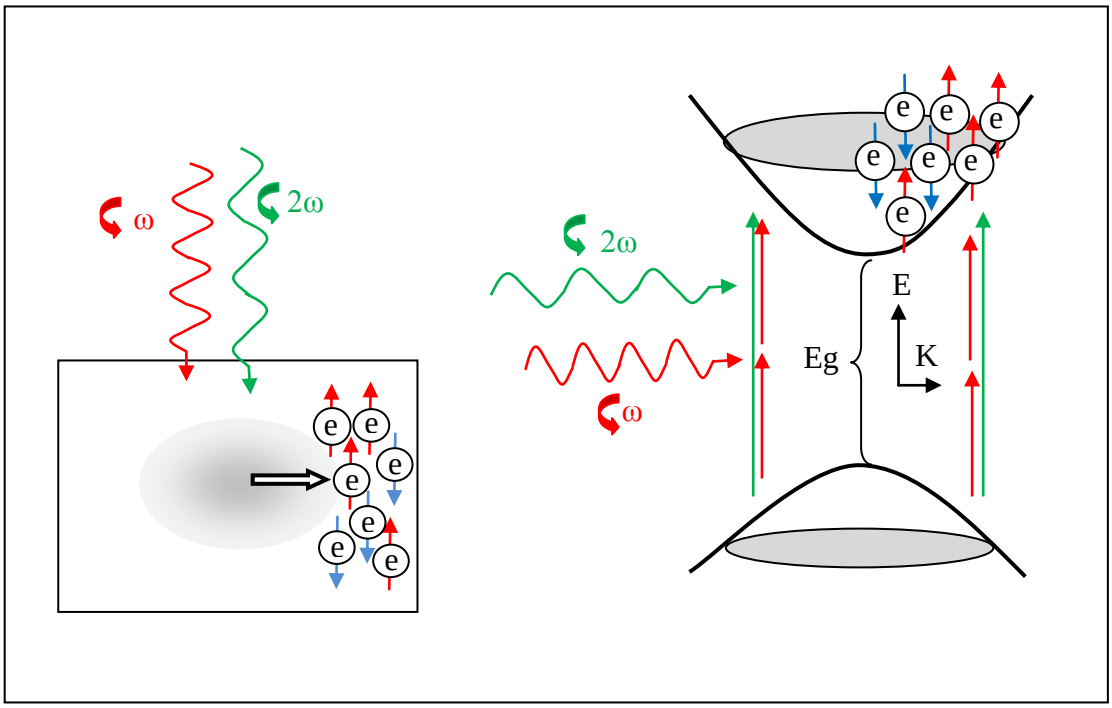

Figure 3.4: Real and k-space drawings of SPCC injection in semiconductors. The left panel is a real-space diagram of the circularly polarized pulses, ω and 2ω, generating a SPCC and the right panel shows a k-space distribution of carriers for SPCC. Both charge and spin are distributed asymmetrically in the k space.

3.4 Experimental setup

Figure 3.5 shows the experimental configuration of QUIC technique to inject ballistic currents. The diode-pumped solid-state continues-wave laser (Spectra-Physics) with a wavelength of 532 nm and a power of 10 W is used to pump the titanium-doped sapphire (Ti:Sapphire) mode-locked laser. The Ti:Sapphire laser is capable of producing a tunable output range of near infrared wavelengths, 690-1080 nm, with a variable pulse width of 80-50 fs and a repetition rate of 80 MHz. The optical parametric oscillator (OPO) is a solid-state laser which is pumped by the Ti:sapphire laser. It employs a lithium triborate nonlinear crystal to generate new infrared frequencies. The output power of the OPO is ~150 mW with a pulse width of ~130 fs. The tunable wavelength ranges in 1.3 -1.5 μm.

The output of the OPO is used as the ω pump pulse and a berium beta borate (BBO) crystal is used to double the frequency of ω to generate 2ω, the second pump pulse. The co-propagating pump pulses are separated, directed to the sample along two paths. Thus, the powers and polarizations of them can be controlled independently. Finally, the pulses are combined and focused tightly to the sample surface using an objective lens.

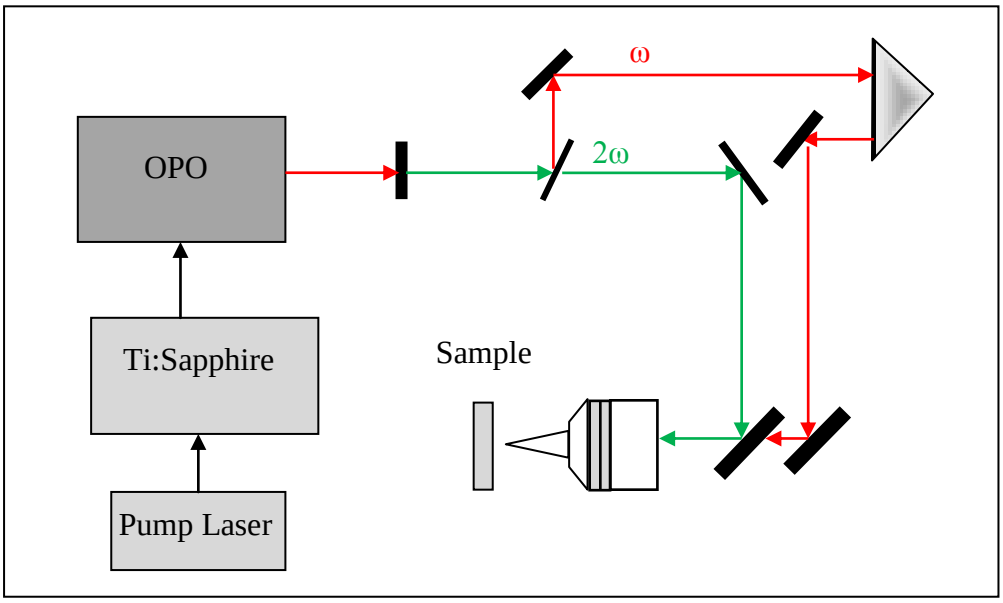

Figure 3.5: Schematic of the experimental apparatus setup to inject ballistic currents using QUIC technique.

In this chapter, I have discussed how QUIC technique can be used to optically inject and coherently control ballistic currents including PSCs, PCCs, and SPCCs in semiconductors. In the next chapter, I will discuss about the pump-probe technique that we use to spatially and temporally resolve these ballistic currents.

Chapter 4

Ultrafast pump-probe technique to study carrier transport

In this chapter, I will first discuss the principles of the pump-probe technique. Then, I will discuss how to achieve high temporal resolution by using femtosecond lasers, and related issues of pulse broadening and pulse compression. Finally, I will discuss the derivative detection scheme that we used to achieve high spatial resolution.

4.1 Principle of pump-probe technique

Pump-probe technique is a powerful tool to study dynamical properties of many systems. In general, a pump is used to change the state of a system, and the change is detected by a probe. Optical pump-probe technique has been widely used to study carrier dynamics in semiconductors. In this scheme a femtosecond pump pulse excites electrons from the VB to the CB of a semiconductor sample. A time-delayed probe pulse monitors carrier dynamics via detecting the change in the transmission or reflection of the sample induced by the pump pulse as a function of time and space. Figure 4.1 shows a schematic of the pump-probe technique.

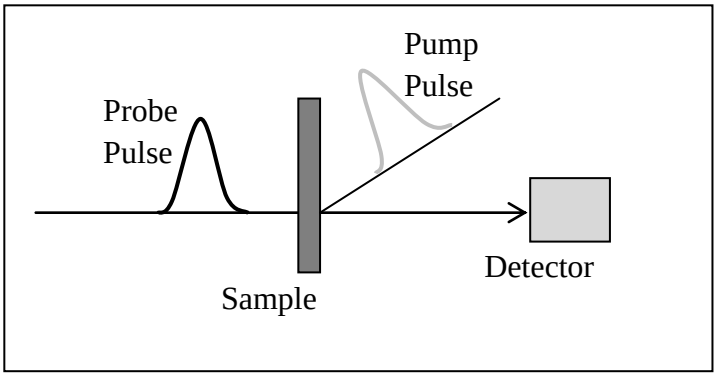

Figure 4.1: Schematic drawing of the pump-probe geometry. The pump pulse is used to change the state of the sample and the probe pulse is used to detect the change explained in the text. The differential transmission of the probe pulse due to the absorption at the sample is monitored by the detector.

4.1.1 Detection of carrier density

In our experiments, we measure the change in the transmission of the probe pulse, which is called the differential transmission, as a function of the time and/or space using lock-in techniques. The differential transmission is directly related to the change in the absorption coefficient. Specifically, we use 2ω pump pulse (or ω pump pulse) to excite electrons from the VB to the CB, and detect the change of the transmission of the probe pulse. As electrons are fermions, two of them cannot occupy the same quantum state. Since the carrier excited by the pump pulse occupy some of the states in the CB, the available states in the CB for the absorption of the probe will be reduced. Thus, the probe transmission will increase. Consider a pulse with intensity, I_{in}, strikes on a sample with a thickness, L, as shown in Fig. 4.2. The transmission intensity,

$$I_{out} = I_{in} e^{-\alpha L}, \tag{4.1}$$

with α, the absorption coefficient of the material.

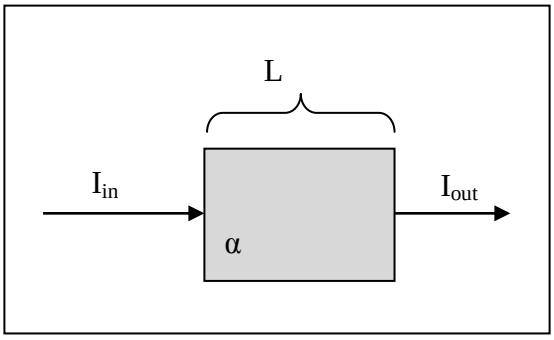

Figure 4.2: Schematic of the transmission of light pulse through a medium with length, L and absorption coefficient, α.

The transmission coefficient is defined as

$$T = \frac{I_{out}}{I_{in}} = e^{-\alpha L}. \tag{4.2}$$

The absorption coefficient with the presence of the carriers excited by the pump pulse, α_n can be written as the sum of the probe absorption coefficient when there is no carriers, α_o and $\Delta\alpha_n$, the change in the absorption coefficient,

$$\alpha_n = \alpha_o + \Delta\alpha_n. \tag{4.3}$$

The differential transmission is defined as

$$\frac{\Delta T}{T_o} = \frac{T_{with\ pump\ excitation} - T_o}{T_o}, \tag{4.4}$$

where ΔT is the change of the probe transmission due to pump pulse and T_o is the probe transmission without the pump pulse. Now, substituting Eq. (4.2) and (4.3) in (4.4), we get

$$\frac{\Delta T}{T_0} = \frac{I_o\, e^{-(\alpha_o + \Delta\alpha_n)L} - I_o e^{-\alpha_o L}}{I_o e^{-\alpha_o L}},$$

$$= e^{-\Delta\alpha_n L} - 1. \tag{4.5}$$

When $\Delta\alpha_n L << 1$, Eq. (4.5) can be simplified to

$$\frac{\Delta T}{T_o} \approx -\Delta\alpha_n\, L. \tag{4.6}$$

In Eq. (4.3), the α_n can be defined as

$$\alpha_n = \alpha_0 \frac{1}{1 + \frac{N}{N_{sat}}}, \tag{4.7}$$

where N and N_{sat} are the carrier density and the saturation carrier density. Now, substituting Eq. (4.7) in (4.3), $\Delta\alpha_n$ can be written as

$$\Delta\alpha_n = \alpha_0 \left[1 - \frac{1}{1 + \frac{N}{N_{sat}}}\right],$$

$$= \alpha_0 \frac{N}{N_{sat}} \left[\frac{1}{1 + \frac{N}{N_{sat}}}\right]. \tag{4.8}$$

Usually, $\frac{N}{N_{sat}} << 1$ hence, Eq. (4.8), can be simplified to

$$\Delta\alpha_n = \alpha_0 \frac{N}{N_{sat}}. \tag{4.9}$$

Using Eq. (4.6) and (4.9), it can be deduced that

$$\frac{\Delta T}{T_0} \propto N. \tag{4.10}$$

Thus, for low carrier densities the differential transmission is proportional to the *N*.

The differential transmission can be measured by sending the probe pulse to a photodiode. The intensity of the pump beam can be modulated by a mechanical chopper and the lock-in amplifier is referenced to the modulation frequency. Usually, a combination of filters is used to block un-wanted light from reaching the detector.

4.1.2 Detection of spin density

The spin density is defined as $S = N^{\uparrow} - N^{\downarrow}$. It can be measured by analyzing carrier-induced circular dichroism of a probe pulse, i.e., the difference in the absorption of the right- and left-circularly polarized components in the presence of spin-polarized carriers (Meier and Zakharchenya 1984). The most effective way to measure *S* is to use a linearly polarized probe pulse, which is composed of equal amounts of left- and right-circular components. Due to spin selection rules, each component preferentially senses one spin system. (Zhao et al. 2009) By using a quarter-wave plate, the two circular components are converted to two orthogonal linear polarizations, which are then separated by a Wollaston prism and sent to two photodiodes of a balanced detector.

The output of the balanced detector is proportional to the difference between the differential transmissions of the two circular components which is proportional to *S*, i.e.,

$$\frac{\Delta T^{+} - \Delta T^{-}}{T_0} \propto S. \tag{4.11}$$

4.1.3 Experimental setup

The experimental configurations for the detection of both *N* and *S* are shown in Fig. 4.3. The 2ω pulse excites electrons to the CB. Depending upon the polarization of the beam, *N* is generated with or without *S*.

As shown in Fig. 4.3, the transmitted probe beam is split to two paths. The pulse in path A is directly detected by a Si-diode in order to measures *N*. The pulse in path B is sent through a quarter-wave plate to convert the left- and right- circularly polarized components to two linearly polarized components. The difference between them is proportional to *S* and is measured using a balanced detector and a lock-in amplifier. Both lock-in amplifiers are referenced to the chopping frequency, so they both read the differential transmission of the probe at the same chopping frequency.

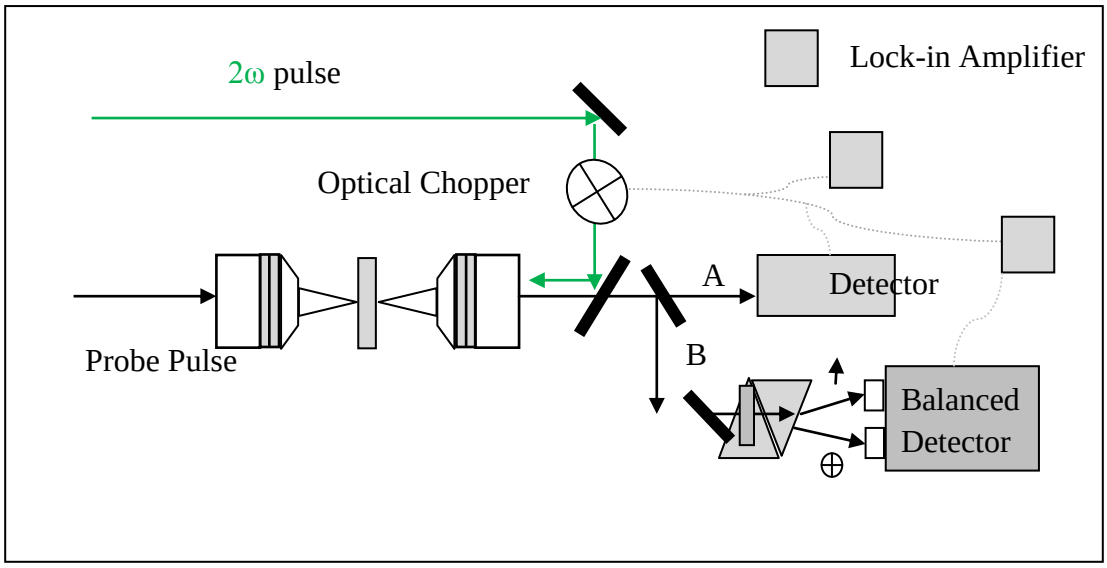

Figure 4.3: Schematic drawing of the experimental setup to measure both N (path A) and S (path B) created by 2ω excitation.

4.2 Achieving high temporal resolution

4.2.1 Femtosecond lasers

Femtosecond lasers are standard tools to study ultrafast dynamics in many systems. The high time resolution is obtained by using short optical pulses from mode-locked lasers. In addition to the high temporal resolution, the spot size of the laser can be adjusted and scanned to obtain high spatial resolution.

Ultrafast laser pulses are electromagnetic wave packets which can be described fully by the time and frequency dependent electric field. The pulse duration, τ_p is defined as the full width of half maximum (FWHM) of the temporal intensity profile. The spectral width, $\Delta\omega_p$ is defined as the FWHM of the spectral intensity profile.

The temporal and the frequency characteristics of the field are related through Fourier transforms,

$$\Delta\omega_p\tau_p = A\,2\pi\,, \tag{4.12}$$

where A is determined by the shape of the pulse. For a Gaussian pulse, $A = 0.441$. (Diels, J. 2006) Therefore, for a Gaussian pulse a wider bandwidth in wavelength, $\Delta\lambda$, corresponds to a shorter temporal width. Specifically, the lower limit of the temporal pulse width for a given bandwidth is called transformation-limited pulse width,

$$\Delta t = 0.441\,\frac{\lambda^2}{c\Delta\lambda}\,. \tag{4.13}$$

4.2.2 Dispersion elements and chirp

Practically, the transformation-limited pulse width is difficult to obtain in experiments because the pulse travels though dispersive elements and broadens temporally. The refractive index of a dispersive element depends on the wavelength. Therefore, different wavelength components travel with different phase velocities. Thus, the duration of the pulse will increase. Even if the laser outputs transformation-limited pulses, since the pulse usually travels through a

number of optics, the width of the pulse delivered to the sample position is not the same transformation-limited pulse width.

The frequency Fourier transform of a Gaussian pulse is

$$E_0(\omega) = \left(A_\omega \, e^{-ln2(\frac{2(\omega-\omega_0)^2}{\Delta\omega})} \right)^{1/2}, \tag{4.14}$$

where A_ω is the amplitude of the pulse (Newport application notes). After propagating through dispersive media, a distance, x, we have

$$E(\omega, x) = E_0(\omega) e^{[-ik(\omega)x]}, \tag{4.15}$$

where $k(\omega) = n\omega/c$, the frequency-dependent propagating factor. (Newport application note; Rulliere 2005)

If we perform a Taylor expansion of the propagating factor, we have

$$k(\omega) = k(\omega_0) + k'(\omega - \omega_0) + \frac{k''}{2}(\omega - \omega_0)^2 + \cdots, \tag{4.16}$$

where

$$k' = [\frac{dk(\omega)}{d\omega}]_{\omega_0} \tag{4.17}$$

and

$$k'' = [\frac{d^2k(\omega)}{d\omega^2}]_{\omega_0}. \tag{4.18}$$

In Eq. (4.16), k adds a constant to the phase, k` adds a time delay which can be determined by the group velocity, $v_G = [\frac{d\omega}{dk}]_{\omega_0}$ and $k``$ is called the group delay dispersion (GDD which introduces a frequency dependent delay or frequency chirp of the different spectral components of the pulse. (Rulliere 2005; Application note – 29 Newport corporation) Here, the GDD in terms of wavelength,

$$k`` = \frac{\lambda^3}{2\pi c^2}\frac{d^2n}{d\lambda^2}, \tag{4.19}$$

where $k``$ depends on the change of the index of refraction upon the wavelength, λ.

4.2.3 Pulse compression

Since most optical elements introduce a positive GDD to an ultrashort pulse, it is possible to compensate the chirp by intentionally introducing a negative GDD. This can be done by using special optical components which can modify the temporal characteristics of pulse by controlling the propagation of different wavelength components of a pulse. In my experiment, I control the pulse with of the pump and probe pulse by using either a pair of prisms or a pair of gratings.

4.2.3.1 Prism

A pair of prism can be used to compress a chirped pulse by adding a negative GDD. In a chirped pulse with a negative GDD, the longer wavelength component (red), travels faster than the shorter wavelength components (blue). Therefore, we can arrange the prism pair such that the red components to travel a longer path compared to blue components. This will allow the blue components to catch the red components.

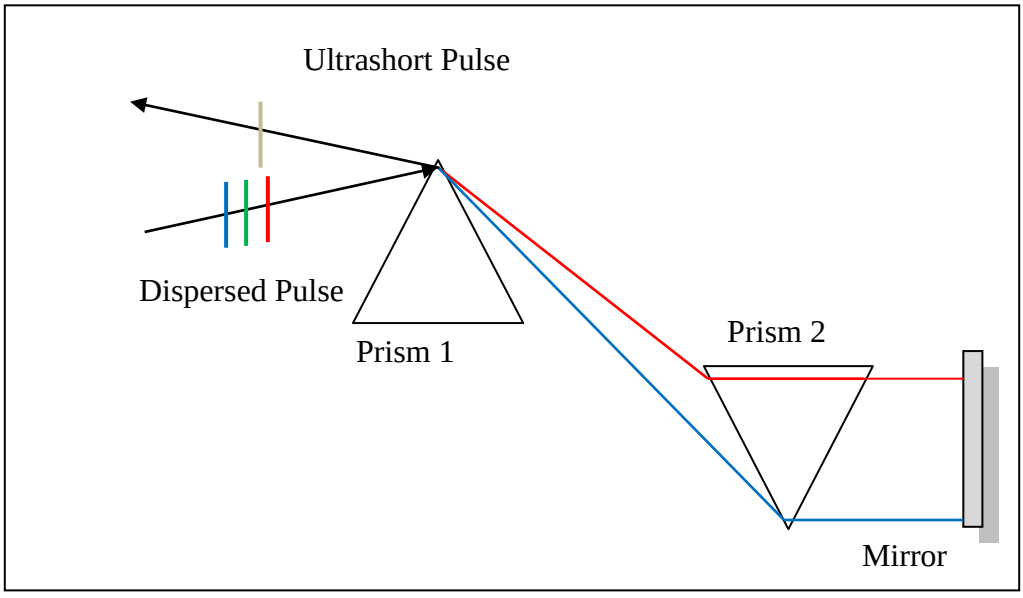

Figure 4.4: Ray diagram and the optics of the prism pair arrangement for pulse compression. The separation of the prisms controls the amount of negative GDD adds to the optical path.

As shown in Fig. 4.4, the prism pair is arranged in such a way that the red components travel a longer path compared to blue components in the Prism 2. The distance between the two prisms also influences the amount of net negative GDD added to the beam path. As the foresaid distance increases, the red components have to travel through more glass; thus it slow down more. However, traveling between the prisms adds a positive GDD to the pulse.

After the pulse travels through the both prisms and arrives at the mirror, the compensation for the time between the colors is partially corrected but the pulse will be spatially dispersed. The spatial and the time correction is fully correct by bouncing the pulse back along the same path. After one round trip through both prisms, the chirped pulse with be compressed both spatially and temporally.

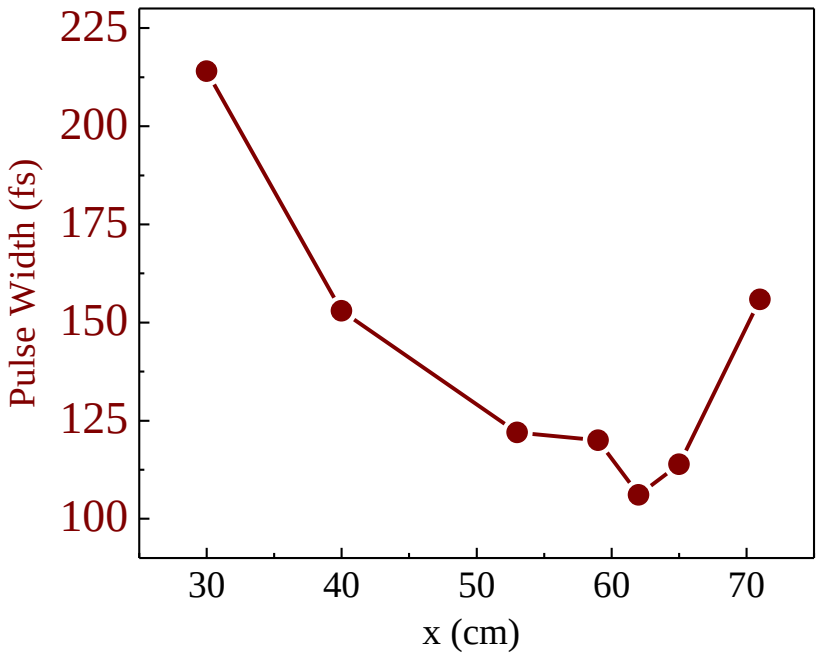

Figure 4.5: The graph of the Ti:Sapphire pulse width versus the separation between the two prisms.

Finally, the compressed pulse width, $w_{unknown}$, is determined by the sum frequency generation technique with another pulse with a known pulse width, w_{known}. The sum of the two pulses ($w_{unknown}$ and w_{known}) are measured at the sample location, w_{sum} and the $w_{unknown}$ is calculated using the following expression.

$$w_{unknown} = [w_{sum}^2 - w_{known}^2]^{0.5} . \quad (4.20)$$

The distance between the two prisms is adjusted to gain the minimum, w_{sum} which corresponds to the minimum, $w_{unknown}$.

Figure 4.5, shows experimental data of compressing the pulse width of Ti:Sapphire pulse. The x-axis denotes the separation of the two prisms in cm-scale. When the two prisms are separated by about 60 cm, the shortest pulse width is achieved. As mentioned in the text, the pulse propagation between the prisms adds a positive GDD. Thus, the transformation-limited pulse width is not possible to obtain at the sample location.

4.2.3.2 Gratings

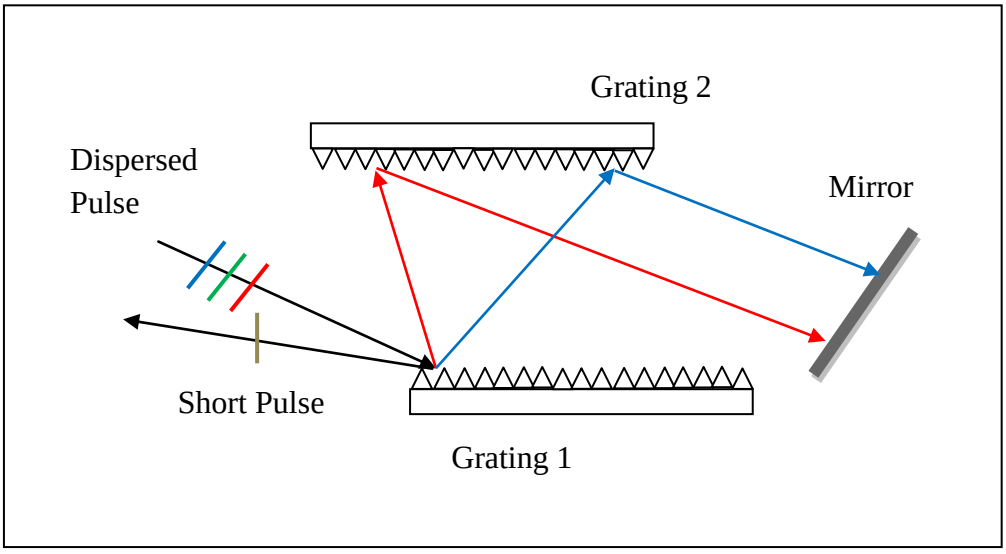

Figure 4.6: Ray diagram and the optics of the pair of gratings arrangement for pulse compression. The separation of the gratings controls the amount of - GDD adds to the optical path.

A pair of gratings can also be used to compress chirped pulses. As shown in Fig 4.6, the grating pair and the other optics are arranged to compress the chirped laser pulse. After reflecting back from the grating 1, the chirped pulse will be further dispersed. The pair of gratings is arranged in such a way that the red components travel a longer distance compared to the blue components. After reflecting off from both grating and arrives at the mirror, the compensation for the time between the colors is partially corrected but the pulse will be dispersed spatially. The spatial and the time correction is fully done after bouncing the pulse back along the same path. As the angular dispersion is stronger compared to that of prisms, the experimental system is more compact. ((Palmer 2002)

Figure 4.6 shows the 2ω pulse width as a function of the separation (in mm scale) between the gratings. The compressed pulse width is calculated using the sum-frequency generation as explained in Sec. 4.3.2.1. Substituting the known pulse width, w_{known} and the experimentally determined sum of the pulses, w_{sum} in Eq. (4.20), $w_{unknown}$ can be calculated.

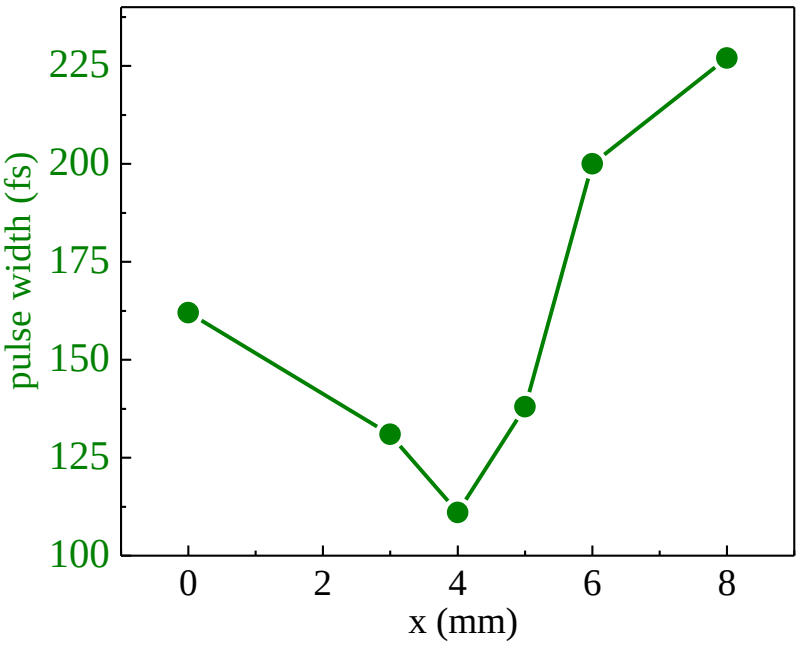

Figure 4.7: The pulse width of the 2ω pulse verses the separation of the gratings in mm-scale.

Similar to Fig. 4.5, Fig. 4.7 shows that both positive and negative GDD broadens the pulse width. When the separation of the pair of gratings is 4 mm, the shortest pulse width of about 107 fs is achieved.

4.3 Achieving high spatial resolution

4.3.1 Derivative detection scheme and spatial resolution

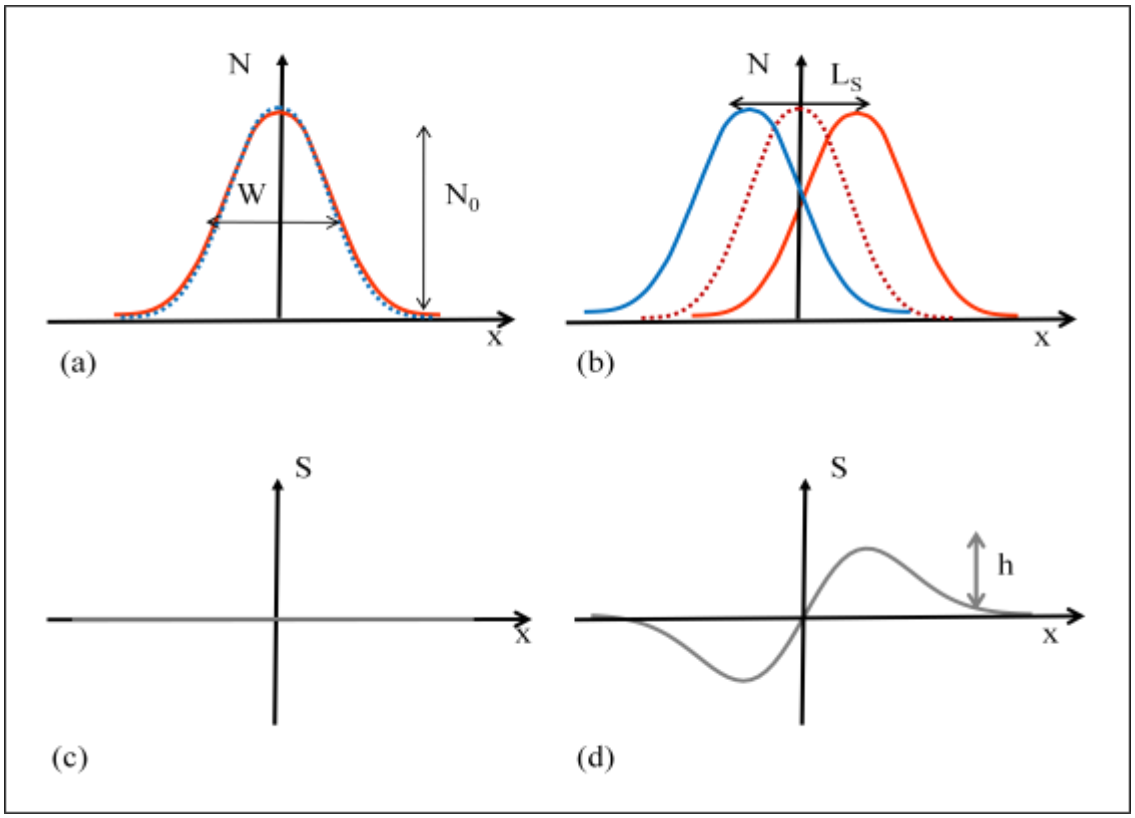

Figure 4.8: Schematic drawing of (a) carrier profile of PSC with total height, N_o, and *FWHM, W*, at $t = 0$, (b) the spin-up and spin-down electron profiles move in opposite directions along $\hat{x}$ direction. The separation, L_s of the two profiles along $\hat{x}$ direction after time, *t.* (c) As the electrons are not moved yet, the spin density, $S = N^{\uparrow} - N^{\downarrow} = 0$ and (d) the two spin-up (-down) electron profiles at $x = \frac{W}{2}\left(-\frac{W}{2}\right)$, the $S = h$, gives the maximum spin density.

In ultrafast laser techniques, the pulse width and the spot size of the laser, limit the time and the spatial resolution, respectively. As the ballistic transport is on nm scales, the spatial resolution has to be pushed beyond the limit of the laser spot size. In my experiment, a derivative detection scheme is used to achieve the desired high spatial resolution. (Zhao 2005)

Similar method is used to calculate the charge accumulation. Upon injection of a PCC, the electron profile move in $\hat{x}$ direction as shown in Fig. 4.9.

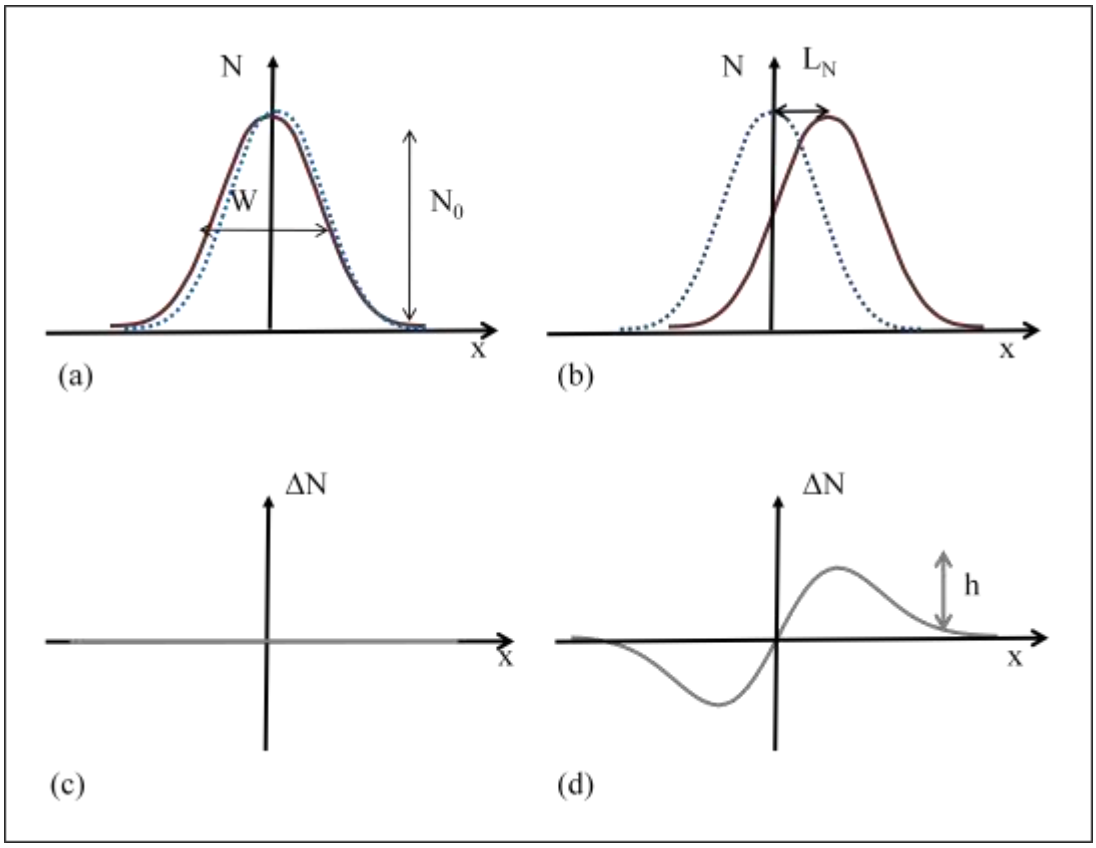

Figure 4.9: Schematic drawing of (a) electron profile of PCC with total height, N_o and *FWHM*, *W*, at $t = 0$, (b) electron profile move along x-axis. L_N the separation of the moved and unmoved profiles along $\hat{x}$-direction after time, *t*, (c) as the electrons are not moved, the charge accumulation, $\Delta N = N^{\uparrow} + N^{\downarrow} = 0$ and (d) electron profile is moved and $= \frac{W}{2}\left(-\frac{W}{2}\right)$, the $\Delta N = h =$ the maximum charge accumulation due to transport.

Similarly, as shown in Fig. 4.9(a), upon injection, the electron profile with width, W and initial height, N_0 is at the origin. Therefore, the charge accumulation is zero as it shows in Fig. 4.9 (c). After time, t, the profile moves a distance, L_N along $\hat{x}$ direction, as shown in Fig 4.9 (b). By measuring the heights of the moved and unmoved electron profiles, h and using expression 4.26, the charge accumulation distance, L_s, can be calculated. (Zhao 2007)

4.3.2 Phase modulation

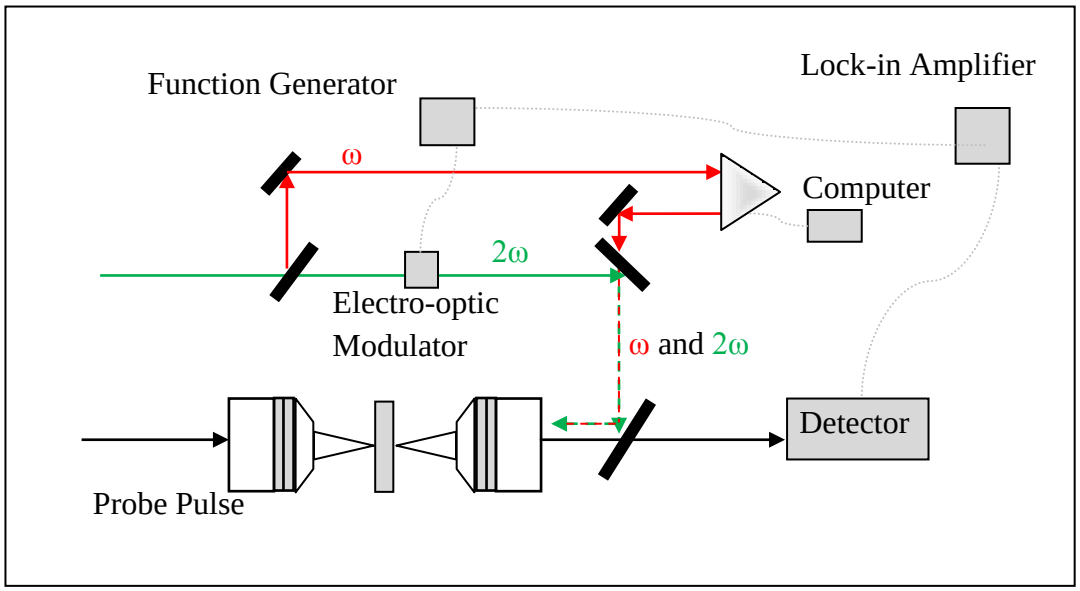

Figure 4.10: The geometry of the phase modulation scheme. The relative phase between ω and 2ω is modulated by a frequency which is assigned using a function generator and the same is referenced to the lock-in amplifier.

Figure 4.10 shows the apparatus setup for the phase modulation. The 2ω pulse is sent through the electro-optic modulator. The phase of 2ω is modulated using a function generator and the same frequency is referenced to a lock-in amplifier. The ω pulse is bounced back using a computer controlled retro-reflector which creates the relative phase between the two pump pulses.

In this chapter, I have discussed ultrafast pump-probe principle as a technique to gain high temporal and spatial resolution in carrier transport studies. In the next chapter, I will discuss three experiments, spin transport in GaAs and Ge and the intrinsic inverse SHE.

Chapter 5

Ballistic transport studied by ultrafast pump-probe technique

In chapter 3 and chapter 4, I have discussed the quantum interference and control technique as the method to inject ballistic currents and the ultrafast pump-probe as a technique to study the carrier transport with high temporal and spatial resolution, respectively. In this chapter, I will discuss three experimental on spin transport performed by using these techniques: spin-polarized charge current in GaAs, intrinsic spin-Hall effect and pure spin currents in Ge.

5.1 Spin-polarized charge currents in GaAs

The injection of spin polarized charge currents in semiconductors is one of the major hurdles in the development of spintronics. The optical injection of ballistic SPCCs using QUIC technique have been demonstrated in several semiconductor nanostructures such as low temperature grown bulk GaAs (Stevens 2002), p-type GaAs/AlGaAs(001) quantum wells grown by metalorganic chemical vapor deposition (Ganichev 2000), n-type GaAs quantum wells (Ganichev et al. 2003), (110)-oriented GaAs/$Al_{0.34}Ga_{0.66}As$ hetero-structures (Diehl 2007), n-type InAs/AlGaAs and p-type GaAs/AlGaAs multiple quantum wells (Ganichev 2001), and $Si_{0.5}Ge_{0.5}$/Si multiple quantum wells (Wei 2007).

In these studies, however, the detection is done by measuring the steady-state voltages (Stevens 2002; Ganichev 2000; Ganichev 2003; Diehl 2007; Ganichev 2001; Wei 2007; Cho 2007; He 2007; Tang 2007) caused only by the charge component of the current. Therefore, the information of the spin polarization and the temporal dynamics of the currents could not be obtained. In our experiment, we used optical methods to detect SPCC pulses in GaAs samples, measured the spin polarization of the currents and time resolved the current dynamics. (Ruzicka 2008)

The experiments are performed on two different GaAs samples at two different temperatures; (a) a multiple quantum well sample at 90 K, which is composed of 10-periods of 14 nm GaAs layers sandwiched by AlGaAs barriers and (b) a 400 nm thick bulk GaAs sample at room temperature.

Figure 5.1 shows a schematic drawing of the experimental configuration. We simultaneously illuminate the GaAs samples with two right-circularly polarized pulses with angular frequencies of ω and 2ω. SPCCs are injected through quantum interference, as discussed in chapter 3. The electrons are injected in to the CB with an average velocity that can be written as

$$< \boldsymbol{v} > = \boldsymbol{v}_0 \eta [sin(\Delta\phi)\hat{x} + cos(\Delta\phi)\hat{y}], \tag{5.1}$$

where $\boldsymbol{v}_0$ is the speed of each electron and η describes the current injection efficiency. (Najmaie 2003) Since both the heavy hole-VB and the light hole-VB transitions are involved in this configuration, according to the spin selection rules the spin polarization of electrons is expected to be about 0.5. (Meier and Zakharchenya 1984)

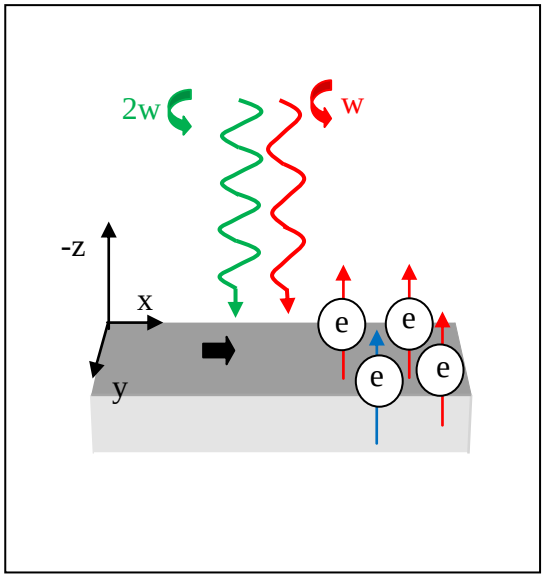

Figure 5.1: Schematics of the experimental configuration of the injection of the SPCC using two circularly polarized pulses.

Figure 5.2 shows the experimental setup for the measurement. The ω pulse with a central wavelength of 1500 nm and a pulse width of 100 fs is obtained from the OPO that is pumped by the Ti:Sapphire laser with a repetition rate of 80 MHz. The 2ω pulse is obtained by doubling the

ω frequency by using a BBO crystal. The two pulses are split using a beam splitter. The 2ω pulse is send through the electro-optical phase modulator in order to modulate its phase. The two pulses are combined and directed to the sample. By using a combination of a polarizer and a quarter-wave plate in each arm, the polarization of each pulse is set to be right-hand circular. The 2ω pulse is tightly focused to a spot size of 1.8 μm FWHM with a peak fluence of 5 μJ/cm^2. The fluence and the beam size of the ω pulse are set to produce the same peak density and size of carrier profile through two-photon absorption.

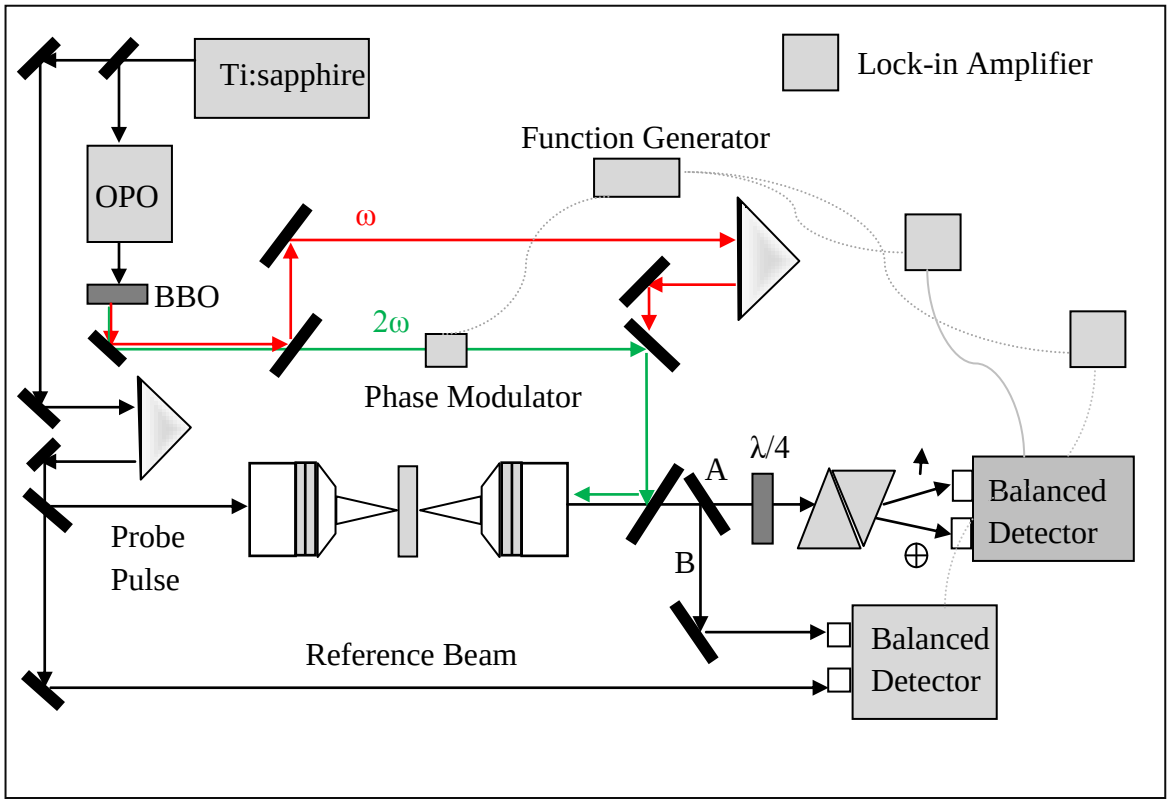

Figure 5.2: Experimental setup to inject and detect spin polarized currents in GaAs samples.

The probe pulse, with a pulse width of 100 fs is taken directly from the Ti:sapphire laser output (Fig. 5.2) and is focused on the sample with a spot size of 1.8 μm FWHM using another objective lens. For the quantum well sample at 90 K, the probe pulse is tuned to the heavy-hole

excitonic resonance (808 nm) to selectively probe electrons based on excitonic absorption saturation caused by free carriers. (Ruzicka 2008)

The linearly polarized probe pulse is split to two parts in order to simultaneously analyze the changes in the polarization state and intensity. In path A, the quarter-wave plate is used to convert the two circularly polarized components of the probe pulse to the corresponding linearly polarized components and the Wellstone prism is used to separate them spatially. The balanced detector reads both components and outputs the difference between them, which is proportional to *S*, to lock-in amplifier. In path B, the detector measures the differential transmission which is proportional to the change of the electron density due to the transport, defined as $\Delta N = N(\tau) - N(\tau = 0)$. It can be viewed as electron accumulation caused by the transport. The two lock-in amplifiers are referenced to the frequency of the phase modulation. Thus the differential transmission of the probe pulse at the frequency of the phase modulation is detected.

The *S*, is measured by analyzing carrier-induced circular dichroism as shown in path B of Fig. 5.2 (Zhao 2005 and 2006). The linearly polarized probe pulse is composed of equal amounts of two circular components. Due to the spin selection rules, each component preferentially senses one spin system and the output is detected as explained Sec. 4.1.2.

The electron accumulation, ΔN is detected by measuring a phase dependent differential transmission by modulating, $\Delta\phi$ (Zhao 2006) (path A of Fig. 5.2). In this measurement, we have achieved the phase modulation by mechanically dithering the length of one arm of the interferometer at 37 Hz using a piezoelectric transducer, instead of using the electro-optic modulator. The output of the balanced detector is detected using a lock-in amplifier as shown in Fig. 5.2. Figure 5.3 summarizes the measurements of the quantum well sample at 90 K performed with a fixed probe delay of 0.3 ps. The spatial profiles of *N* [(a) – circles], ΔN [(a) – solid spheres], *S* [(b) – open squares], and *S* [(b) solid squares] are measured by scanning the probe along $\hat{x}$ direction with $\Delta\phi = \pi/2$. The panels (c) and (d) show the change of ΔN and ΔS as a function of $\Delta\phi$ for three different probe positions, respectively.

Panels (a) and (b) in Fig. 5.3 show the Gaussian profiles of *N* and spin density are consistent with the shape and size of the laser spots. The derivative-like ΔN profile shows that electrons accumulated along $\hat{x}$ direction. From these profiles, the transport length $L_N = 5$ nm is deduced by using the procedure described in Sec.4.3.2. Spin transport is also evident from the derivative-like profile. Panels (c) and (d) show the phase control of the current injection. Up

triangles (down triangles) in (c) show ΔN as a function of $\Delta\phi$ measured at $x = +1.7(-1.7)$ μm. The two curves are out of phase by π. Furthermore, measurement at $x = 0$ shows no signal above the noise level. Similar results are obtained for the ΔS as shown in Panel (d).

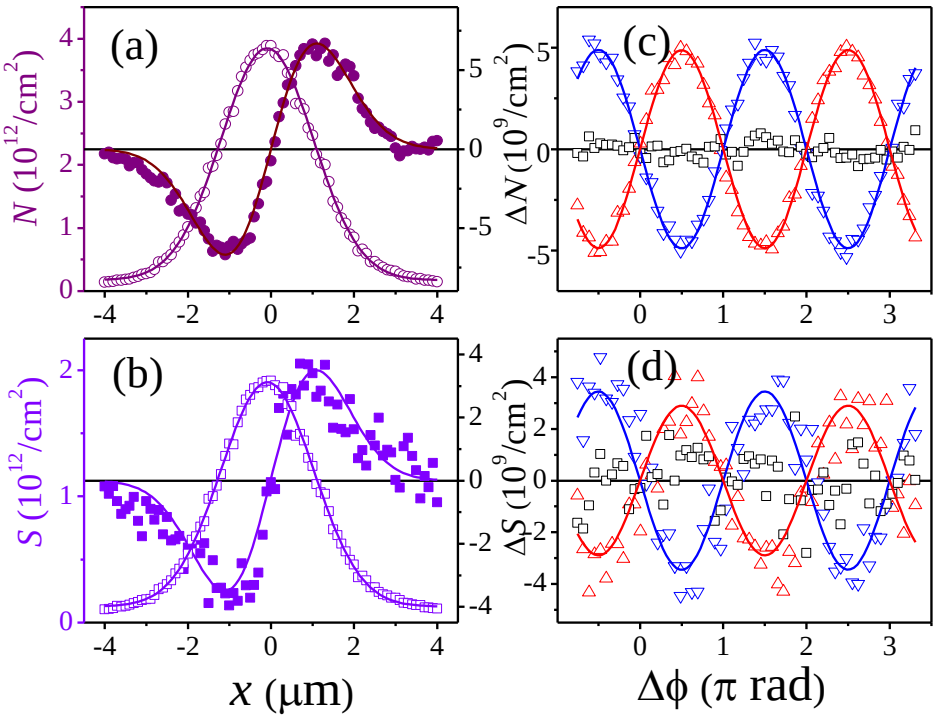

Figure 5.3: Experimental results on spin-polarized charge current on the GaAs quantum well sample at 90 K. The profiles of N and the Gaussian fit [(a) - purple circle and the line], ΔN and the Gaussian fit [(a) - purple spheres and the line], S and the Gaussian derivative fit [(b) – violet squares and the line], ΔS and the Gaussian fit [(b) – solid squares and the line] measured with a τ of 0.3 ps and $\Delta\phi = \frac{\pi}{2}$. From the lines in the panel (a), and the two profiles in panel (a), a transport length of 5 nm is deduced. Panel c (d) shows ΔN (ΔS) measured at a probe position of $x = +1.7$ μm (up triangles), -1.7 μm (down triangles) and zero (squares), respectively, when $\Delta\phi$ is varied. The blue and red lines in the panels (c) and (d) are the sinusoidal fits of the data.

Figure 5.4 shows the measurement of the transport length, L_N, as a function of the probe delay. The solid triangles show the temporal evolution of the average position of electrons. A time derivative of the curve gives the temporal evolution of the average velocity and, therefore, the charge current density, as shown with solid-squares in Fig. 5.4.

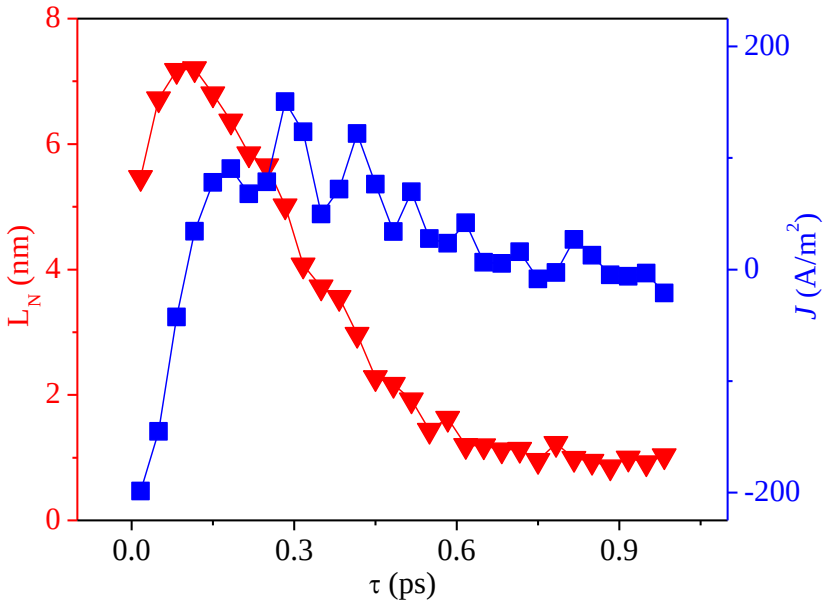

Figure 5.4: Temporal resolution of the average position of the electrons (red- solid triangles and the line) and the density of the current (blue- solid squares and the line) in the ten periods of 14 nm GaAs quantum well sample at 90 K. (Ruzicka 2008)

The oscillatory behavior of the electrons shown in Fig. 5.4 is caused by the space charge field between the electrons and the holes. Upon injection, electrons move along $+\hat{x}$ direction. The same quantum interference process also injects holes with opposite momentum. Thus, holes move along $-\hat{x}$ direction. Since heavy holes have a larger effective mass than the electrons, they move with a smaller average velocity. Once the electrons and the holes separate in space, a space-charge field develops. It drives the electrons and holes back to a common location, which can be clearly seen in the red-triangle curves of Fig. 5.4. During the whole process, strong

phonon and inter-carrier scatterings exist. Hence, the oscillator is strongly damped. Multiple oscillations are not observed.

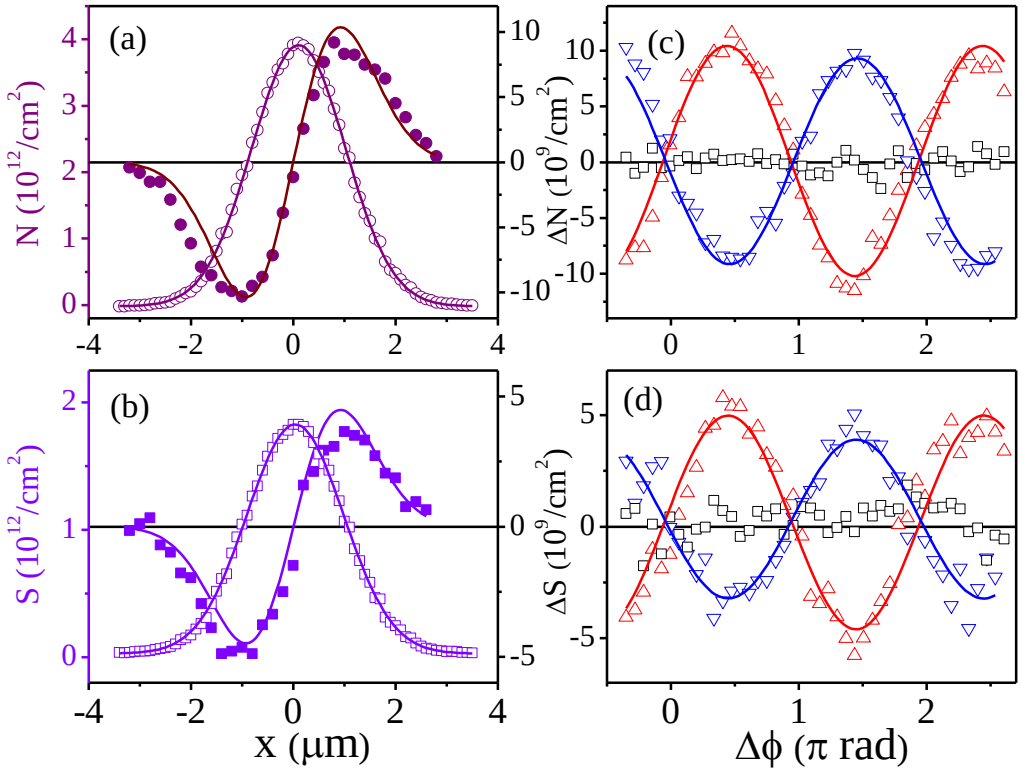

Figure 5.5: Profiles of (a) N and Gaussian fit (purple – circles and line), (a) ΔN and Gaussian derivative (purple–solid circles and line), (b) S and Gaussian fit (violet squares and line) and (b) S and Gaussian derivative (violet–solid squares and line) measurement with a τ of 0.3 ps and $\Delta\phi = \frac{\pi}{2}$, on the bulk sample at room temperature. From the two profiles in panel (a), a transport length of 3.8 nm is deduced. Panels (c) and (d) show, ΔN and the ΔS measured at a probe position of $x = +1.0$ μm (red – up triangles), -1.0 μm (blue –down triangles) and 0 (black squares) respectively, when $\Delta\phi$ is varied. The red and blue lines are the sinusoidal fits of the data.

The experiment on the bulk sample at room temperature is carried out under the same excitation conditions. At room temperature, the excitonic resonances are thermally broadened and overlap with band-to-band transitions. Therefore, it is difficult to selectively probe the heavy-hole excitonic transitions as we did on the quantum well sample at 90 K for efficiently sensing carriers and their spin. In this measurement, the probe pulse is tuned to a central wavelength of 820 nm, with an excess energy of 90 meV. This causes the differential transmission signal $\frac{DT(N)}{T_0}$ to drop by a factor of 20 with the same carrier density.

In order to detect a reduced signal, we improved the signal-to-noise ratio of the detection by replacing the mechanical modulation (37 Hz) device by an electro-optical phase modulator with 2439 Hz modulation frequency. Figure 5.5 shows the measurements on the bulk sample at room temperature performed with a probe delay of 0.3 ps in a similar way of Fig 5.3. Using similar procedures, we deduce a transport length of $L_N = 3.8$ nm.

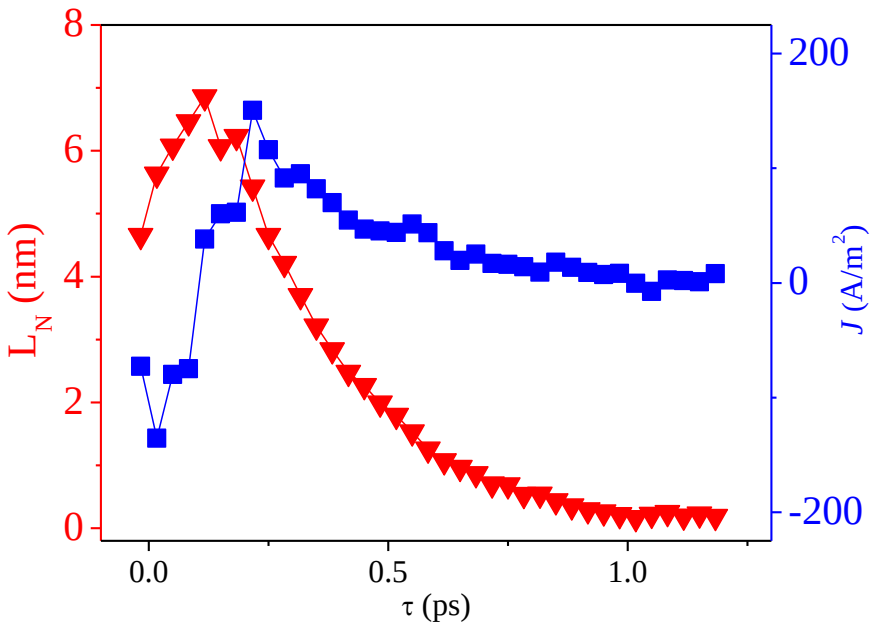

Figure 5.6: Temporal resolution of the transport length (red–down triangles and the line) and current density (blue-solid squares and the line) in the bulk sample at room temperature as a function of τ. (Ruzicka et al. 2008)

The measurement summarized in Fig. 5.5 is repeated as a function of the probe delay, in order to temporally resolve the dynamics. The results are shown in Fig. 5.6.

The dynamics observed in the two experiments are similar. The current dynamics are determined by a number of factors including inter-carrier scatterings, phonon scatterings, and space-charge field. Since phonon absorption rates increase with temperature, one would expect faster momentum relaxation at room temperature, suggesting a smaller maximum transport length. The similar maximum transport lengths observed at 90 K and room temperature indicate that the momentum relaxation is likely dominated by inter-carrier scatterings and phonon emission.

In summary, we demonstrate optical generation and detection of spin-polarized charge currents in GaAs bulk and quantum well structures at room temperature and at 90 K. In contrast to previously reported works, we determined the spin-polarization of the currents, and time-resolved the current dynamics. We found that the currents are ac, due to the strong space-charge field.

5.2 Spin Hall effect

The SHE is a carrier transport phenomenon predicted a long time ago (D'yakonov et al. 1971) and was revisited recently in number of theoretical works (Hirsch 1999; Zhang 2000; Murakami 2003; Sinova 2004). The Hall effect occurs when an electric current flows through a medium with a magnetic field in the transverse direction. Due to the Lorentz force, there exists a charge imbalance in the transverse direction which results a Hall voltage. The SHE is observed in the absence of an externally applied magnetic field. A charge current can induce a spin imbalance in the transverse direction due to the SOI.

Figure 5.7 is a schematic drawing of the Hall effect. As shown in the left panel, electrons are dragged in the -$\hat{y}$ direction by the electric field in $\hat{y}$ direction. As the electrons are charged particles, upon an application of an external magnetic field, B, along $\hat{z}$ direction, there exists a Lorentz force on the electrons in $\hat{x}$ direction as shown in the right panel of Fig. 5.7. Due to the electron accumulation, there exists a voltage in $\hat{y}$ direction which is called the Hall voltage.

Figure 5.8 shows the mechanism of the SHE. Similar to the Hall effect, the electrons are dragged by the electric field, as shown in the left-panel of Fig. 5.8. In the absence of an applied magnetic field, the SOI influences the motion of the electrons. Due to the SOI, the scattering of electrons with impurities is spin-dependent. That is, when scattering off impurities, spin-up electrons are more like to scatter towards one transverse direction, while the spin-down electrons scatter to the opposite direction. This selective scattering mechanism creates a spin imbalance in the transverse direction to the direction of the applied electric field is called the SHE.

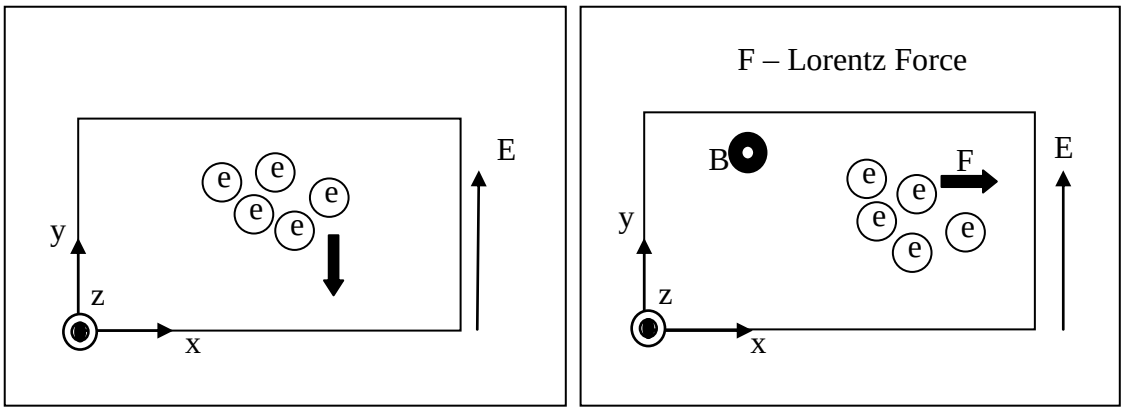

Figure 5.7: Schematic drawing of Hall-effect. The electrons are driven by the electric field and move in the $-\hat{y}$ direction as shown in the left panel. The application of the magnetic field in $\hat{z}$ direction induces Lorentz force on the moving electrons along $\hat{x}$ direction. Thus, the electrons move along $\hat{x}$-direction as shown in the right panel.

The first experimental observations of SHE (Koto 2004; Wunderlich 2005) have stimulated extensive experimental (Sih 2005 and 2006; Stern 2006, 2007 and 2008; Zhao 2006) and theoretical (Mishchenko 2004; Sheng 2005; Kane 2005; Zhang 2005; Nikolic 2005; Bernevig 2005; Murakami 2004; Engel 2005) studies. This effect provides an electrical method to generate spin currents which is an important tool for spintronics. Based on the same physical mechanism, a PSC can generate a transverse charge current. Such an inverse SHE has also been

proposed (Hirsch 1999) and experimentally observed. (Zhao 2006; Valenzuela 2006; Kimura 2007).

In the original proposal of SHE, the induced transverse spin current is caused by spin-dependent scattering. This is now referred to as an extrinsic SHE. An intrinsic SHE originates during the free flights of electrons has also been predicted (Hirsch 1999) which is important in studies of fundamental aspects such as the SOI. Further, this scattering-free ballistic SHE is important in nano technology.

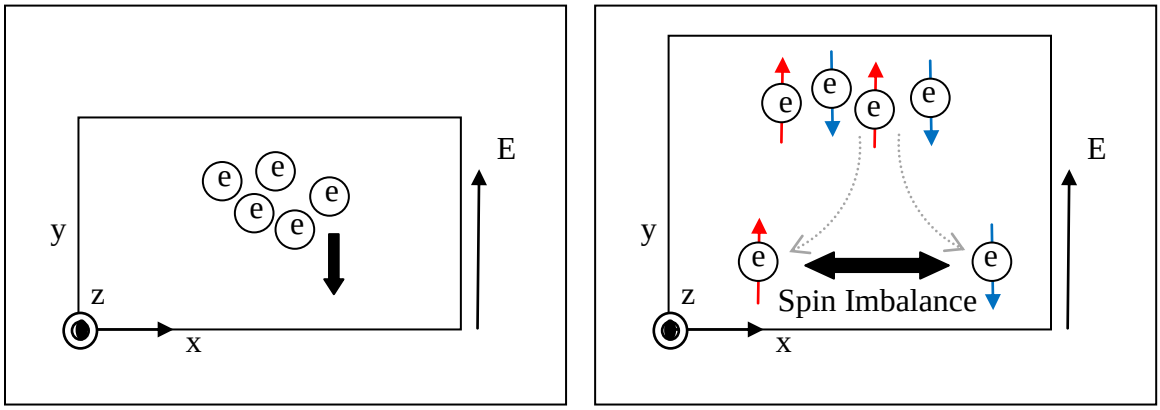

Figure 5.8: Schematic drawing of the SHE. The electrons are driven by the applied electric field, hence move in $-\hat{y}$ direction as shown in the left panel. In the absence of an external magnetic field, the effect of the SOI influences a spin dependent scatting. The spin-up electrons scatter off to one side and the spin-down electrons scatter of to the opposite side of the sample. Thus there will be a spin imbalance transverse to the direction of the applied electric field.

The basic physics of the intrinsic SHE is illustrated in Fig.5.9. In a two dimensional system, electronic Eigen states have definite momentum and, because of SOI, a momentum-dependent effective magnetic field which causes the spins (red arrows) to align perpendicularly to the momenta (green arrows), as shown in Fig 5.9(a). In the presence of an electric field in $\hat{x}$-direction, electrons are accelerated and drift through momentum space as shown in Fig 5.9(b).

The SHE arises from the time dependence of the effective magnetic field experienced by the spin because of its motion in momentum space. (Sinova 2004)

Our approach to observe the intrinsic SHE is to time resolve the current generation and decay dynamics. We studied three un-doped GaAs/AlGaAs multiple quantum well samples: Samples A and B are both 40 periods, with quantum well thicknesses of 7.4 nm and 10 nm, respectively. Sample C has 20 periods of 14 nm quantum wells. The samples are cooled to 10 K to reduce phonon scattering.

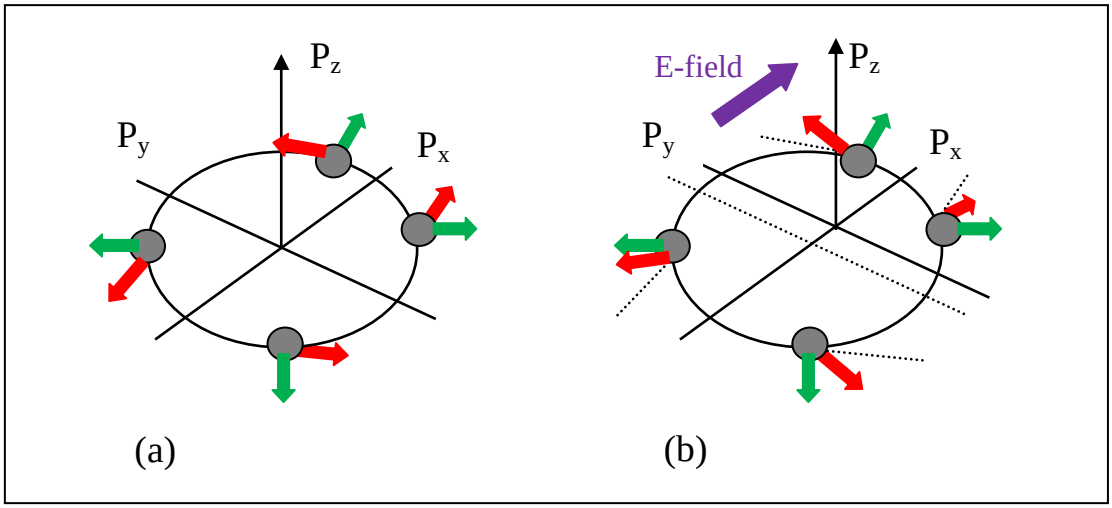

Figure 5.9: Schematic showing of (a) the Fermi surface for two-dimensional system with a Rashba spin-orbital field. Momentum direction and the spin-orbital fields are illustrated with green and red arrows respectively and (b) while moving in momentum space; electrons experience an effective torque which tilts the spin up for $p_y > 0$ and spin down for $p_y < 0$ creating a spin current in the $\hat{y}$ direction. (Sinova 2004)

The sample is simultaneously illuminated by pump pulses ω and 2ω with orthogonal polarizations ($\hat{x}$ and $\hat{y}$ directions) to inject PSC as explained in Sec. 3.2.1. The experimental details and the setup used for this study are similar to the description in Sec. 5.1 and Fig. 5.2.

Initially, the spatial profiles of the spin-up and spin-down electrons overlap in space as shown in the left-panel of Fig. 5.10. After a short period of time, the profiles separate by a

distance of Δx, as a result of the opposite motion of the two spin systems along $\hat{x}$ direction as shown in the right-panel of Fig. 5.10. Due to the inverse SHE, both profiles are expected to move along $\hat{y}$ direction, resulting in a displacement of Δy from origin.

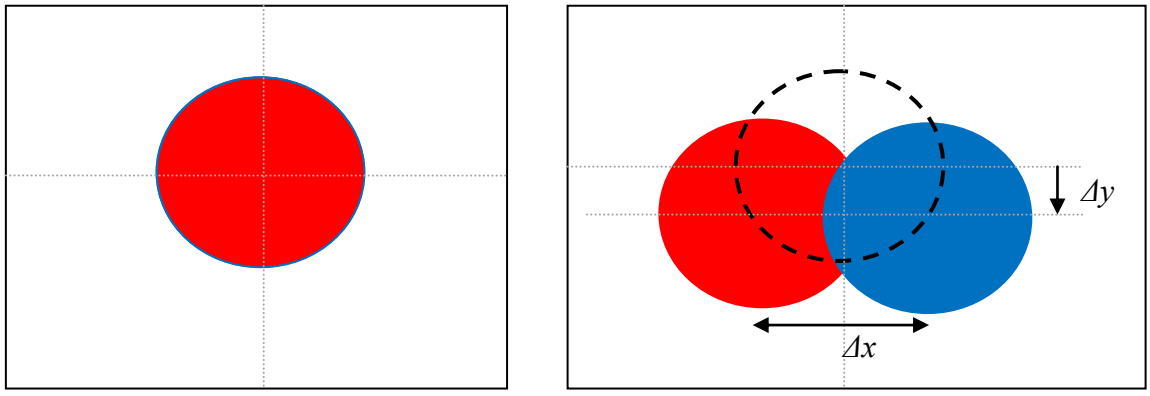

Figure 5.10: Schematic drawing of the spin-up and spin-down profiles of PSC in x-y plane. Upon injection, (left panel) the electron profiles are over lapped and (right panel) spin-up and spin-down electron profiles move oppositely along $\hat{x}$ direction and separate by Δx. Due to the inverse SHE, both profiles to move along $\hat{y}$ direction, resulting in a displacement of Δy from origin.

The experimental setup for this experiment is similar to the one shown in Fig. 5.2. Here, the probe pulse is tuned to the heavy-hole exciton resonance (790 nm) to selectively probe electrons. Both carrier density and spin density are measured. As discussed earlier, the density of the PSC injected by the QUIC technique is proportional to $cos(\Delta\phi)$. In this measurement, we choose $\Delta\phi = 0$ in order to get the maximum PSC injection. Figure 5.11 shows the measured data for the sample A. The panel (a) shows N measured by scanning the probe spot on the sample in x-y plane with a $\tau = 0.5$ ps. The peak carrier density is 6×10^{16}cm^{-3}. The panels (b) and (d) (red squares) show the measure data of the injected PSC measured along $\hat{x}$ [horizontal white line in panel (a)] and $\hat{y}$ [vertical while line in panel (a)] directions and the panels (c) and (e) (green stars) show that of induced charge current, respectively.

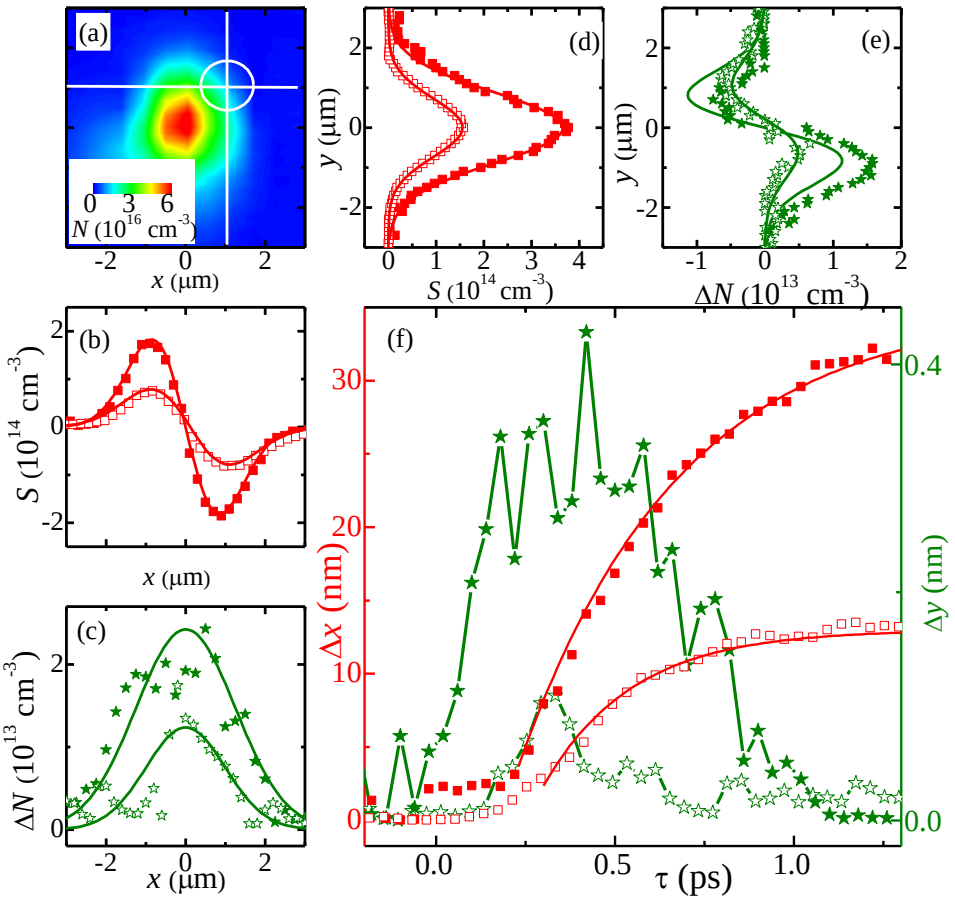

Figure 5.11: The experimental data. Panel (a) shows the profile of N with a peak value of 6×10^{16} cm^{-3}. The S, and ΔN, measured by scanning the probe spot along the horizontal line shown in panel (a) are plotted as the red-solid squares in panel (b) and the green-solid stars in panel (c), respectively. The red lines in the panel (b) and green-lines in the panel (c) are the fits of Gaussian derivative-like and Gaussian profiles respectively. Red-solid squares and the green-solid stars in panel (d) and (e) show both S and ΔN measured by scanning the probe spot along the vertical line shown in the panel (a). The red lines in the panel (d) and green-lines in the panel (e) are the fits of Gaussian and Gaussian derivative like profiles, respectively. Panel (f) shows the deduced Δx (red-solid squares) and Δy (green-solid stars) as a function of the τ. All the open symbols in panels (b)-(f) show corresponding results obtained with a higher peak carrier density of 2.4×10^{17} cm^{-3}. (Werake 2011)

To time resolve the dynamics of both currents, we fix the probe delay at $x = y = 1$ μm [white circle in Fig 5.11 (a)] and simultaneously measure spin density and electron accumulation due to transport as we scan. Figure 5.11 (f) shows *Δx* (red – solid squares) and *Δy* (green – solid stars) as a function of the probe delay. The increase of *Δx* indicates the spin transport, and is slowed down by the scattering mechanisms. The line over the solid squares is the fit of the data with a momentum relaxation time, τ_m=0.45 ps for each spin system.

The decrease of *Δy* after the peak is due to the motion of the electrons back towards the origin which is caused by the induced space charge field between spatially separated electrons and holes. We deduce that at τ_m=0.45 ps, $\Delta x = 17$ nm. Due to the inverse SHE, we expect the profile, *N*, to move along $\hat{y}$ direction, resulting a nonzero *ΔN*. Using the derivative-like profile in Fig. 4.10(e), we deduced $\Delta y = 0.3$ nm. Since the pump pulses do not inject a charge current when the relative phase, $\Delta\phi = 0$, the charge current along $\hat{y}$direction is generated by the PSC along $\hat{x}$ direction via the inverse SHE. The simultaneously measured *S* has a Gaussian-like profile along $\hat{y}$ direction, as shown in Fig. 5.11(e). As the two spin systems do not separate along $\hat{y}$ direction, the profile is expected to be a Gaussian-like shape. Similarly, the simultaneously measured *ΔN* by scanning the probe along $\hat{x}$ direction has a Gaussian-like profile, Fig 5.11(c).

The momentum relaxation of each spin system is caused by scattering events, and therefore the relaxation time of the PSC is determined by the scattering time. Since the sample is undoped, impurity scattering is negligible. The scattering mechanisms contributing to the momentum relaxation include electron-hole scattering, phonon scattering, and scattering between electrons with opposite spin orientations. Therefore, a charge current induced by the electron-hole scattering via the extrinsic inverse SHE can only be established on a time scale longer than 0.45 ps. However, the simultaneously measured *Δy* reaches the maximum before 0.45 ps [green solid stars in Fig. 5.11 (f)]. Since the charge current has been established well before the first scattering event, it cannot be due to the extrinsic inverse SHE (Werake 2011).

We repeated the experiment with higher carrier density and the data are shown in Fig. 5.11 (b)-(f) with open symbols. The momentum relaxation of each spin system is faster, due to the increased scattering rate between the electrons and the holes. The established charge current is observed before the deduced $\tau_m = 0.25$ ps which confirms the intrinsic nature of the observed SHE.

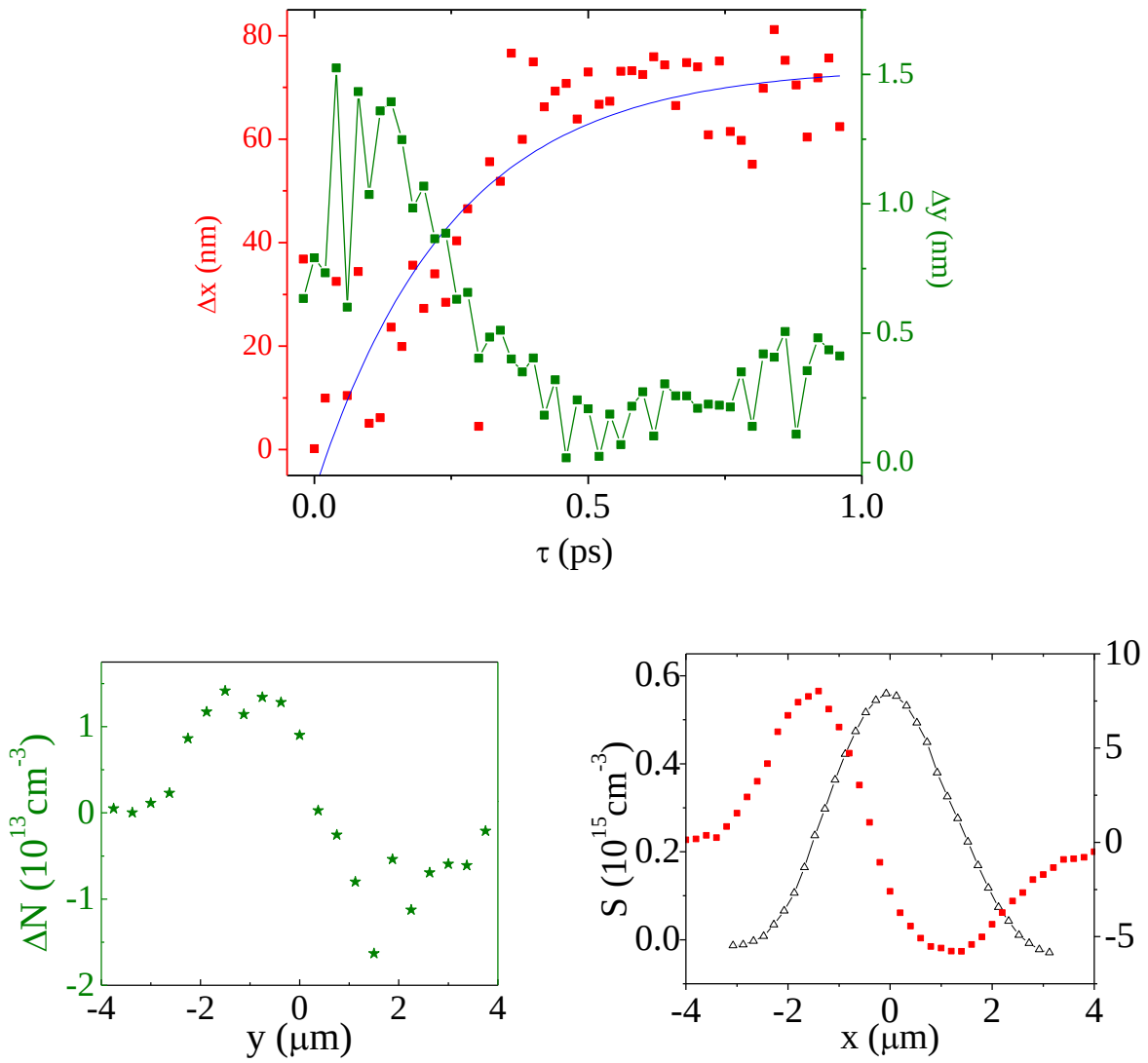

Figure 5.12: Top Panel shows the time dynamics of the PSC and the charge current as a function of τ [corresponds to Fig. 5.11(f)]. The blue line is an exponential fit of the data with a model, $y = A(1 - e^{\frac{x}{\tau_m}})$, gives a $\tau_m = 0.25$ ps is deduced. The lower-left panel, green stars show the derivative like profile of the charge current in $\hat{y}$ direction [corresponds to Fig 5.11(e)]. The lower-right panel, red-solid squares show the spatial profile of the injected PSC along $\hat{x}$ direction [corresponds to Fig. 5.11(b)] and the black-up triangles represent the spin profile. (Werake 2011)

Figure 5.12 shows the experimental data of the sample B with a carrier density of 9×10^{16} cm^{-3} and with the probe pulse at the heavy-hole resonance, 795 nm. Panel A shows the spatial profiles of the spin density (black–up triangles) and the spin accumulation (red–solid square) of the injected PSC along $\hat{x}$ direction. Panel B shows the spatial profile of the charge accumulation in $\hat{y}$ direction. Panel C shows the temporal dynamics of both currents.

The transverse charge current is observed before the relaxation time of the PSC of 0.25 ps [blue-solid line in Fig 5.12 top panel], which is consistent with results of sample A. Due to the instrumental noise in the system, the later portion of the green-star curve shows a wiggly behavior. Figure 5.13 shows the time dynamics of the PSC and the induced charge current for the sample C at two different probe position in x-y plan.

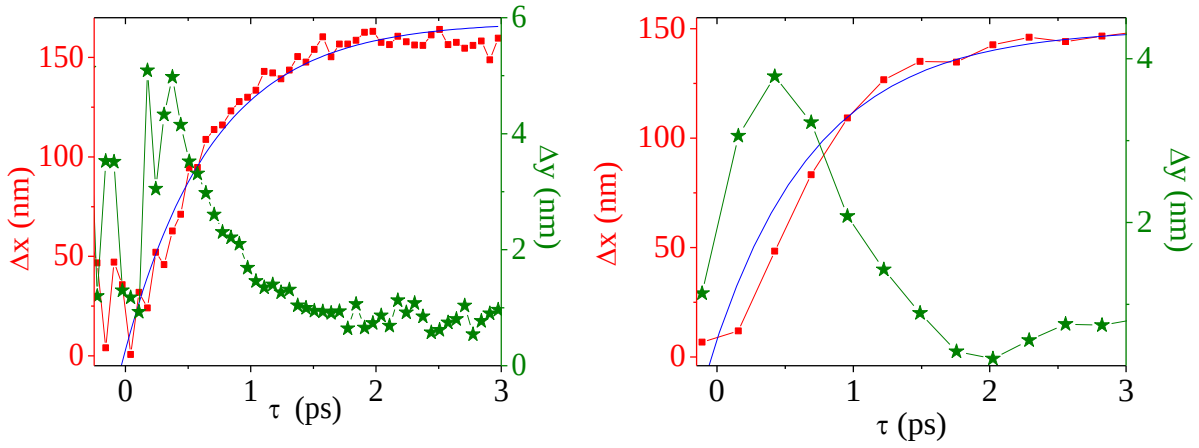

Figure 5.13: The time dynamics of the sample C at two different probe positions. The blue lines are the exponential-fits of the data. (Werake 2011)

With a carrier density of 4×10^{16} cm^{-3} (roughly 2.5 times lower compared to the carrier density of sample B) the relaxation time of the PSC is increased to 0.6 ps which is deduced from the fit (blue lines) of the data. Clearly the charge current is generated much earlier than this time scale. The data presented above confirms the intrinsic nature of the inverse SHE in our experiment.

5.3 Pure spin current in Ge

Due to their indirect bandgap and centrosymmetric crystal structure, the group IV semiconductor such as Si and Ge are hardly used in photonic applications. With a direct bandgap, GaAs is the commonly used material for photonic applications. Si is the material of choice for electronic applications; however, the lattice mismatch of GaAs and Si is large. On the other hand Ge has shown strong electro-optical and nonlinear optical response and has an acceptable lattice match with GaAs. (Loren 2010) In addition, as Ge has a large atomic radius, the SOI is expected to be stronger compared to Si (Wang 1990). Therefore, Ge can be an important material for spintronics applications. In this section, I will present our studies on PSC injection and detection in Ge.

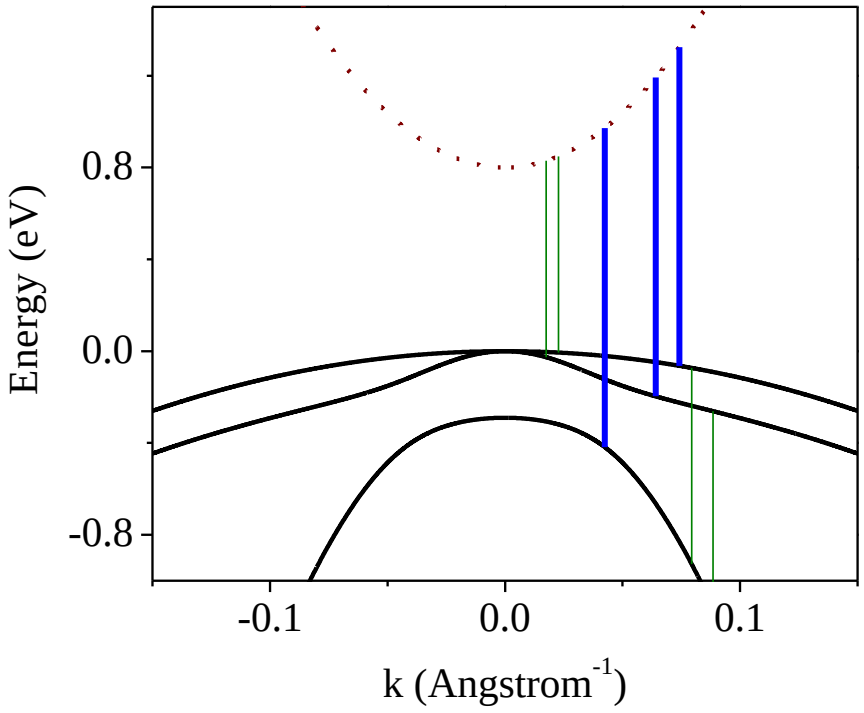

Figure 5.14: The excitation schemes showing the ω and 2ω pump pulses (thick blue) coupling the same initial state in the heavy hole-VB, the light hole-VB, and the split off-VB and final states in the CB of Ge, and showing the direct, and intervalence band transitions with the absorption of the probe pulse (thin green). (Loren 2009)

In the experiment, the sample of 1 μm thick bulk Ge is simultaneously illuminated by two pump pulses (ω – 1786 nm and 2ω – 893 nm) with orthogonal polarizations ($\hat{x}$ and $\hat{y}$ directions) to inject PSC as explained in Sec. 3.2.1. (Stevens 2003; Zhao 2007) The experimental details and the setup used for this study are similar to the description in Sec. 5.1 and Fig. 5.2.

The PSC injection process and spin dynamics in Ge are expected to be similar to those in GaAs. The spatial (left panel) and phase dependence (right panel) of *S(ΔS* in figure) are shown in Fig. 5.15, similar to those shown in Fig. 5.3 and Fig. 5.5. The spatial dependence of spin density is shown in the left panel of Fig 5.15 for a fixed probe delay and a fixed relative phase, $\Delta\phi = \pi$. The phase dependence of the spin density *(ΔS* in figure) is shown in the right panel of Fig. 5.15. Both panels together in Fig. 5.15 show that for a fixed phase, spin-up and spin-down polarized carriers accumulate in opposite sides of the sample and the accumulation sides can be switched by flipping the phase by π. The cosinusoidal dependence of the spin density on the phase and the derivative like spatial profiles confirm the injection of PSC.

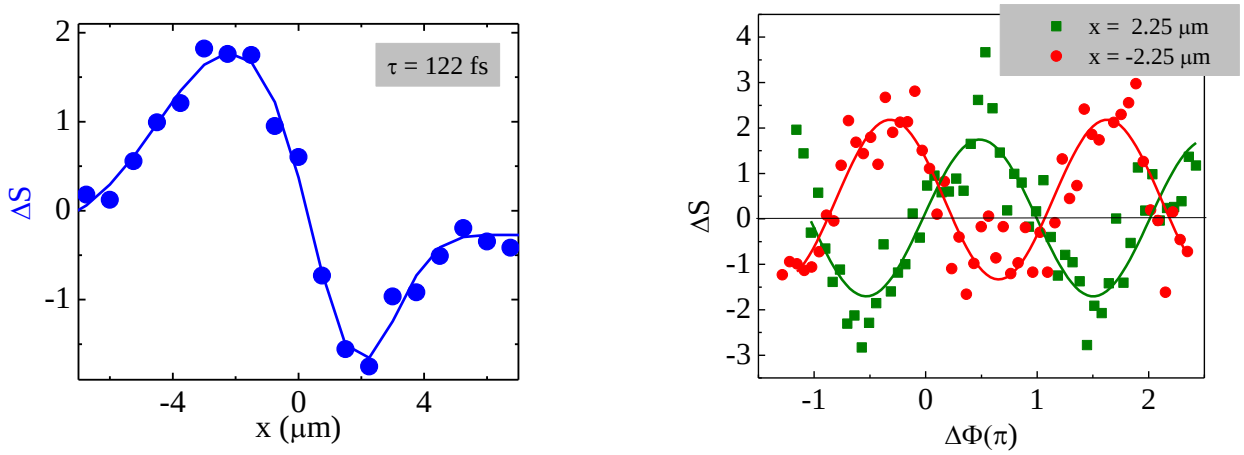

Figure 5.15: The spin density, *S* (*ΔS* in figure), is measured, (left panel) as a function of the position of the probe in x̂-direction with $y = 0$ for τ =122 fs and for fixed $\Delta\phi = \pi$. (right panel) The *S* (*ΔS* in the figure) is graphed as a function of $\Delta\phi$, at fixed τ and $x = 2.25$ μm and -2.25 μm the red and green lines are the sinusoidal fits of the data.

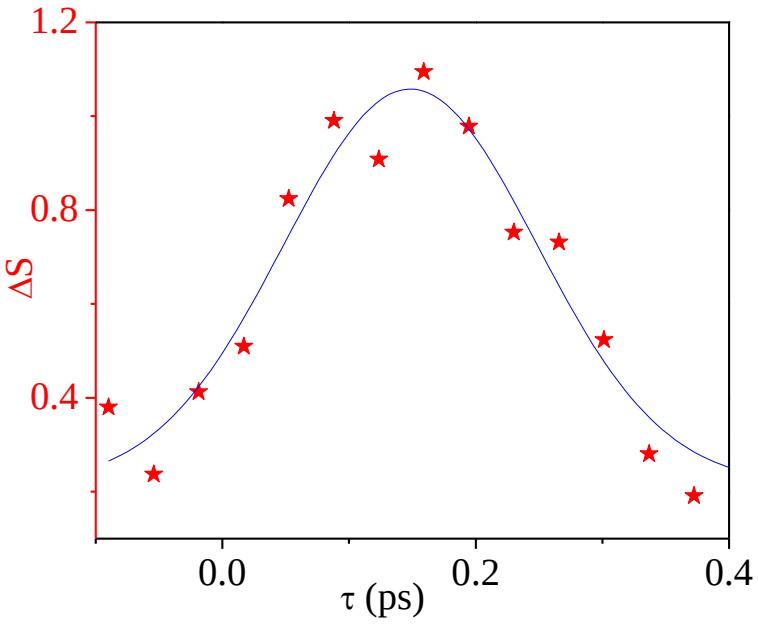

Figure 5.16: The temporal dynamics of spin density at fixed x =2.25, $y = 0$ μm and $\Delta\phi = \pi$ and the blue line is a Gaussian fit of the data with $FWHM = 0.23$ ps. (Loren 2009).

Figure 5.16, shows the temporal dynamics of the injected PSC at fixed probe position, $x = 2.25$ μm, $y = 0$ and relative phase, $\Delta\phi = \pi$. The green line illustrates the Gaussian fit of the data which shows a qualitative consistence with the Gaussian shaped laser pulse.

In GaAs experiments, the probe was primarily sensitive to the electrons, and the separation of the spin profile remained until electronic spin relaxation, recombination and diffusion, all of which occur on 100 ps time scales, were complete. The fast decay of spin current in Ge is either a consequence of the rapid scattering of the electrons to the side valleys or of the ultrafast spin relaxation of the holes.

In summary, we have demonstrated all-optical spin injection in Ge using quantum interference processes and have detected the signatures of the spin current. The efficiency of generation and the lifetime of, spin currents in Ge via the QUIC scheme might be comparable to that of GaAs. However, because the electron intervalley scattering time and the hole spin relaxation time are short, the spin accumulation signal decays much faster in Ge than in GaAs.

In this chapter, I have discussed the experimental details and the data analysis of the ballistic spin transport studies in three different experiments studied by using the high-resolution pump-probe technique. In the next chapter, I will discuss the spin transport studied by using the nonlinear optical technique that directly senses the electron velocity.

Chapter 6

Second-harmonic generation technique

In previous chapters, I have discussed the principle of the pump-probe technique and experimental results obtained by using this technique. In this chapter, I will discuss the second-harmonic generation as a new and more convenient tool to study carrier and spin transport in semiconductors. First, I will discuss the principle of both intrinsic and extrinsic second-harmonic generation. Then, I will discuss in more detail the theory of external second-harmonic generation induced by DC field, pure charge current and pure spin current. Finally, I will discuss our experimental approaches.

6.1 Second-harmonic generation

Optical harmonic generation is related to higher order susceptibilities. It has been used to study crystallographic, electronic, magnetic and structural information of materials. Specifically, the SHG is exploited as a very sensitive tool for space and time symmetry violation studies. In addition, it is a prominent probe to study surface and interface properties.

Consider an optical field, $E(\omega)$, with an angular frequency, ω, interacts with a crystal. The field induces a dipole oscillation of atoms in the crystal. The atoms generally behave as anharmonic oscillators, if the field amplitude is sufficiently large. Hence, the dipoles oscillate at frequencies of 2ω, 3ω, and even higher harmonics in addition to the fundamental frequency. These oscillating dipoles emit electromagnetic radiation, that is, light waves with frequencies ω, 2ω, and higher harmonic frequencies.

The induced dipole moment per unit volume, polarization, $[\boldsymbol{P}(\omega,t)]$, can be written as,

$$\boldsymbol{P}(\omega,t) = \epsilon_o\left[\boldsymbol{E}(\omega,t)\chi^{(1)} + \boldsymbol{E}(\omega,t)^2\chi^{(2)} + \boldsymbol{E}(\omega,t)^3\chi^{(3)} + \cdots\right], \tag{6.1}$$

where $\chi^{(2)}$ and $\chi^{(3)}$ are the second and third order nonlinear susceptibilities and ϵ_0 is the permittivity of a vacuum. The above equation can be written in terms of the first, second and other higher order polarizations,

$$\boldsymbol{P}(\omega,t) = \left[\, \boldsymbol{P}(\omega,t)^{(1)} + \boldsymbol{P}(\omega,t)^{(2)} + \boldsymbol{P}(\omega,t)^{(3)} + \cdots \right], \tag{6.2}$$

where $\boldsymbol{P}(\omega,t)^{(1)} = \epsilon_0 \chi^{(1)} \boldsymbol{E}(\omega,t)$ is the linear optical response and $P(\omega,t)^{(2)}$ is the second-order optical responses of the medium (Boyd 2008).

A centrosymmetric medium possesses inversion symmetry, which means the medium can be superimposed in to its mirror image. Thus, the polarization induced by the inverted electric field is expected to be the same as the one induced by the electric field in the original direction. By substituting $-\boldsymbol{E}(\omega,t)$ in $\boldsymbol{E}(\omega,t)$ in the expression (6.1), the induced polarization of an electric field which propagates in $-\hat{z}$ direction can be expressed as

$$\boldsymbol{P}(\omega,t) = \epsilon_o \left[\chi^{(1)}\big(-\boldsymbol{E}(\omega,t)\big) + \chi^{(2)}\boldsymbol{E}(\omega,t)^2 + \chi^{(3)}(-\boldsymbol{E}(\omega,t)^3) + \cdots \right]. \tag{6.3}$$

If $\chi^{(2)}$ and other even order susceptibility terms are zero, $\boldsymbol{P}(\omega,t) = -\boldsymbol{P}(\omega,t)$. Thus the terms with odd powers of the electric field for example, $\boldsymbol{P}(z,t)^{(1)}$ and $\boldsymbol{P}(z,t)^{(3)}$ will hold while the even powers of the electric field for example, $\boldsymbol{P}(z,t)^{(2)}$ will vanish for centrosymmetric systems. Therefore, in order to observe the SHG, the crystal has to be noncentrosymmetric.

SHG can be observed in noncentrosymmetric; systems which do not show inversion symmetry. The second order polarization $\boldsymbol{P}(2\omega)$ can be written as

$$\boldsymbol{P}(2\omega) = \epsilon_0\, \chi^{(2)}\boldsymbol{E}(\omega)^2, \tag{6.4}$$

where the polarization of the medium is proportional to the square of the electric field.

The generation of second-harmonic light can be categorized in to two groups namely intrinsic SHG and extrinsic SHG. These two types are discussed in detail in the following two sections.

6.2 Principle of intrinsic second-harmonic generation

As described above, the lack of inversion symmetry in a bulk crystal or at the surface of the material can generate second order nonlinear susceptibility.

The SHG was first observed by Franken and co-workers (Franken 1961) in 1961 right after the discovery of laser by T.H. Maiman in 1960. Then, Mayer (Mayer 1968) and Giordmaine and co-workers (Giordamaine 1962) showed that the magnitude of the generated second harmonics can be improved by many orders of magnitude by applying the phase matching concept and changing the temperature of the medium.

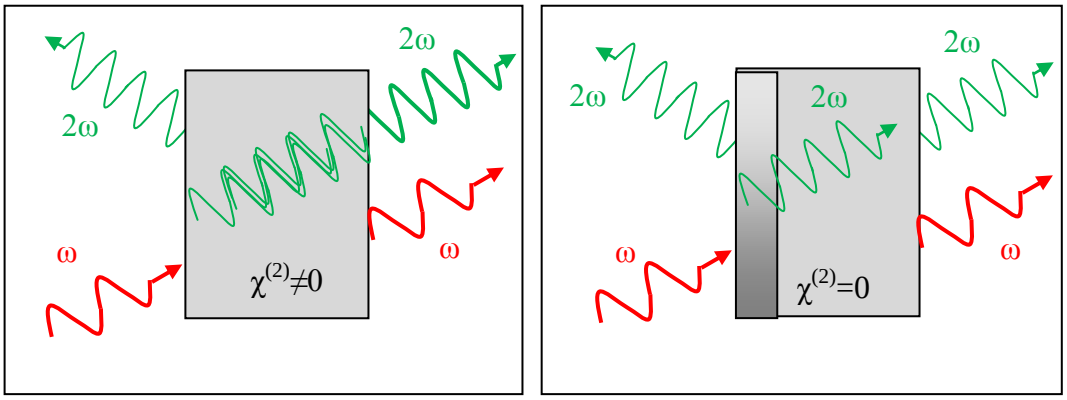

Figure 6.1: Illustration of SHG. Left panel shows a noncentrosymmetric bulk structure, the second-harmonic light is generated at the surface and in the bulk medium, right panel shows a centrosymmetric bulk structure, the second-harmonic light is generated only at the surface which is partially reflected and transmitted in to the bulk structure.

6.2.1 Second-harmonic generation in noncentrosymmetric bulk structure

With SHG, the total electric field within the noncentrosymmetric medium, in the direction of propagation, $\hat{z}$, can be written as,

$$\boldsymbol{E}(z,t) = \boldsymbol{E}_{\omega}(z,t) + \boldsymbol{E}_{2\omega}(z,t)\,, \tag{6.5}$$

with each component,

$$\boldsymbol{E}_j(z,t) = \boldsymbol{A}_j e^{-i\omega_j t} + c.c.\,, \tag{6.6}$$

where j = ω, 2ω and $\mathbf{A}_j$, slowly varying amplitudes. Moreover, the propagation constant and refractive index can be written as

$$k_j = \frac{n_j \omega_j}{c} \qquad \text{and} \qquad n_j = [\epsilon^{(1)}(\omega_j)]^{1/2}\,. \tag{6.7}$$

Using Eq. (6.4), the total polarization in the medium can be written as

$$\boldsymbol{P}^{NL}(z,t) = \boldsymbol{P}_{\omega}(z,t) + \boldsymbol{P}_{2\omega}(z,t), \tag{6.8}$$

with components,

$$\boldsymbol{P}_j(z,t) = \boldsymbol{P}_j e^{-i\omega_j t} + c.c..\,, \tag{6.9}$$

and the polarization amplitude of ω,

$$\boldsymbol{P}_{\omega}(z) = 4\epsilon_0 d_{eff} \boldsymbol{A}_{2\omega} \boldsymbol{A}_{\omega}^{*} e^{i(k_{2\omega}-k_{\omega})z}\,, \tag{6.10}$$

and 2ω,

$$\boldsymbol{P}_{2\omega}(z) = 2\epsilon_0 d_{eff} \boldsymbol{A}_{\omega}^{2} e^{2ik_{\omega}z}\,, \tag{6.11}$$

with $d_{eff} = ½\,\chi^{(2)}$ and amplitudes,

$$\boldsymbol{A}_{\omega} = \left[\frac{I}{2n_{\omega}\epsilon_0 c}\right]^{\frac{1}{2}} \boldsymbol{U}_{\omega} e^{i\phi_{\omega}}\,, \tag{6.12}$$

and

$$\boldsymbol{A}_{2\omega} = \left[\frac{I}{2n_{2\omega}\epsilon_0 c}\right]^{\frac{1}{2}} \boldsymbol{U}_{2\omega} e^{i\phi_{2\omega}} \,. \tag{6.13}$$

Here $\boldsymbol{U}_j$ are the normalized field amplitudes and the real, normalized fields amplitudes are conserved,

$$\boldsymbol{U}_{\omega}^2(z) + \boldsymbol{U}_{2\omega}^2(z) = 1. \tag{6.14}$$

The total intensity of the two waves which are invariant under propagation can be written as (absorption is ignored),

$$I = I_{\omega} + I_{2\omega} \,. \tag{6.15}$$

with $I_j = 2n_j\epsilon_0 c A_j^2$. The relative phase between the two waves can also be introduced as,

$$\Delta\phi = 2\phi_{\omega} - \phi_{2\omega} + \Delta k_z \,. \tag{6.16}$$

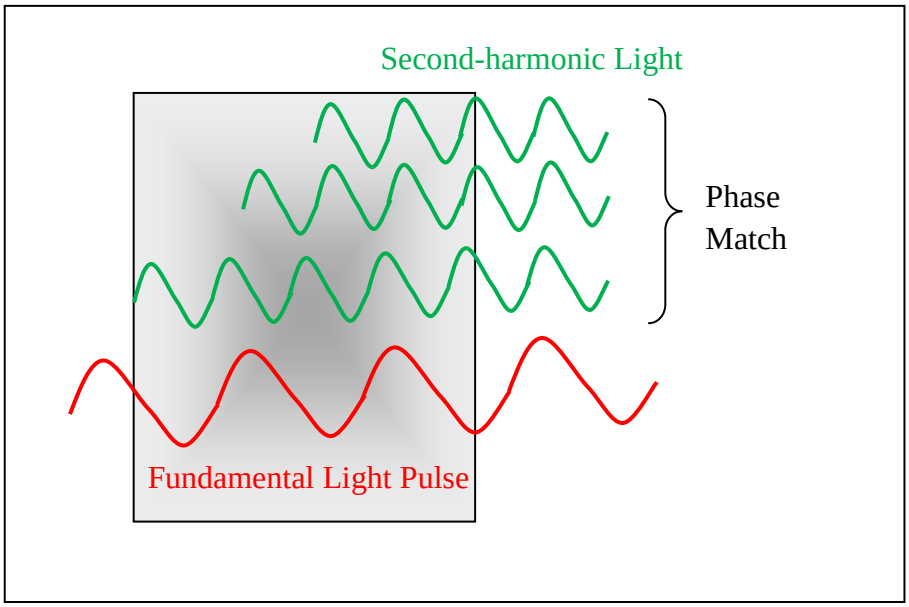

Figure 6.2: The phase matching concept. Inside the sample, the second-harmonic light pulses will be generated at each layer. All the pulses have to be added constructively to generate an intense output.

In order to generate a significant intensity of second-harmonic light, the generated light waves with 2ω frequency throughout the medium has to have the same phase, $\Delta k_z = 0$, in the expression (6.16). If not they interfere destructively and the output intensity will be very low. Therefore for the maximum SHG output, the light has to travel in the medium at the same velocity (Fig. 6.2). Thus, the refractive indices for the two waves with frequencies ω and 2ω have to be the same (Boyd 2008; Franken 1961),

$$n(\omega) = n(2\omega)\ . \tag{6.17}$$

In order to achieve the foresaid phase matching condition, birefringent crystals are used. They have both extraordinary and ordinary indices of refraction. By tuning the angle of incidence and/or the temperature, the foresaid phase match condition can be accomplished. (Boyd 2008)

Such a process is actually used in our previous discussions in generating the 2ω pump pulse. There, the frequency of ω pulse is doubled by using a BBO crystal which has reasonably high conversion efficiency at a particular phase matching angle.

6.2.2 Second-harmonic generation at the surface/interface

The centrosymmetric nonlinear optical materials do not possess a bulk second-order nonlinear optical susceptibility. However, the presence of the interface breaks the inversion symmetry for a thin layer on the order of one molecular diameter in thickness. This thin layer can emit a second-harmonic wave. (Boyd 2008) The intensity of the light emitted by this surface layer depends sensitively on the structural properties of the surface and particularly, the presence of molecules absorbed on to the surface as shown in right-panel of Fig. 6.1. Therefore, the surface SHG is an important diagnostic method in surface science.

The surface SHG technique is sensitive to detect less than a monolayer of molecules absorbed on a surface. Moreover, the surface SHG is highly directional and it is therefore suitable for remote sensing studies and can be used for monitoring surface in a real environment. These advantages make SHG a unique and versatile tool for surface studies.

6.3 Extrinsic second-harmonic generation

Second-harmonics generation due to electric-dipole interactions is restricted to the systems lack of inverse symmetry. However, such restrictions can be removed and materials with inverse symmetry can also show nonzero second order susceptibility if the system is perturbed externally, for example by a DC electric field or a flow of current. In these situations, the inversion symmetry is broken. In the following, I will explain how a charge current, and a PSC and a DC electric field can break the symmetry of a centrosymmetric material to induce a non-zero second order susceptibility.

6.3.1 Charge current induced second-harmonic generation

As stated in Sec. 6.1 and 6.2, in order to induce second-order nonlinear effects in a centrosymmetric system, it is required to break the symmetry of the system. It is shown that a charge current can introduce an asymmetry in the system (Khurgin 1995) and thus induces SHG.

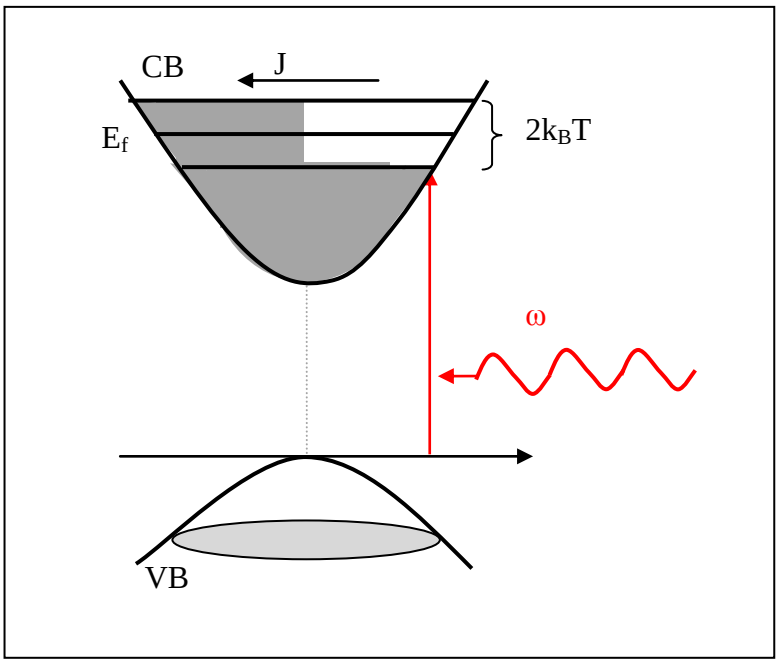

Figure 6.3: The band diagram of the energy states involved in the SHG. (Khurgin 1995)

In a simple two-band model, the induced SHG is proportional to the current in the semiconductor. Consider an n-doped direct bandgap semiconductor with the Fermi level, E_F, lies in the CB as in Fig. 6.3. As a result of an applied field, E, the distribution of the electrons in the CB is described by $[f(\boldsymbol{k}) - f^o(\boldsymbol{k})]$ where $f(\boldsymbol{k})$ is the centro-symmetric equilibrium distribution function and the $f^o(\boldsymbol{k})$ is distribution function which explain the deviation from the equilibrium. (Khurgin 1995)

Figure 6.3 shows an energy band diagram with the bands involved in ω excitation. As a result of the applied field, the equilibrium distribution is shifted in the k space by the amount,

$$\boldsymbol{k}_E = -\frac{e\tau E}{\hbar}. \tag{6.18}$$

Due to the symmetry contribution, state with $\boldsymbol{k}$ will be canceled by the states with $-\boldsymbol{k}$ and only the state within $k_B T$ of the Fermi surface will contribute to SHG. Moreover, they are the same states that are responsible for the DC current flow of,

$$\boldsymbol{J} = -\frac{e\hbar}{m_c}\sum_{\boldsymbol{k}} \boldsymbol{k}\,[f(\boldsymbol{k}) - f^o(\boldsymbol{k})]\,, \tag{6.19}$$

in the CB of the sample. In the presence of the current, the cancellation of the states with $-\boldsymbol{k}$ and $\boldsymbol{k}$ is not complete as there are electron-hole pairs block this process on the left than on the right. (Khurgin 1995)

6.3.2 Spin current induced second-harmonic generation

It is predicted that a PSC can also induce SHG. (Wang 2010) The theory is based on the Faraday rotation caused by spin-polarized electrons. Figure 6.4, shows a diagram of the Faraday rotation of an optical field. The rotation of the plane of the linearly polarized light wave propagating through a magnetized dielectric medium is called the Faraday rotation, as illustrated in Fig. 6.4. Applying a magnetic field causes circular birefringence in the material which decomposes the light into ordinary and extraordinary rays. These rays propagate at different speeds through the medium, combined at the end, yields a ray with a rotated polarization from the incident ray. The rotation is a function of the magnetic field.

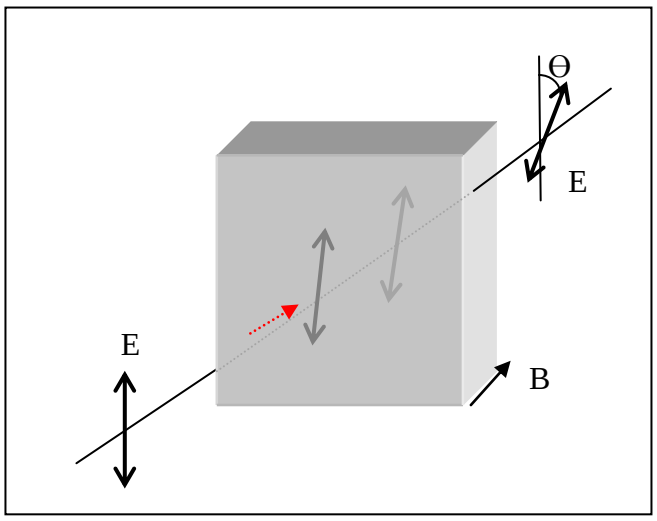

Figure 6.4: Illustration of the Faraday rotation of an E-field. The rotation angle, θ, is a function of the applied magnetic field, B.

Similarly, an electron with a certain spin orientation causes Faraday rotation of a linearly polarized light (Malojovich 2000), with an angle determined by the detuning between the frequencies of the light and the interband transition of the electron. In a PSC, each electron is accompanied by another electron with an opposite crystal momentum and an opposite spin orientation. The Faraday rotation caused by the two electrons seems to cancel.

Using systematic symmetry analysis, Wang (Wang 2010) has discussed the unique polarization dependence of the second-order optical effects of general PSCs. Consider optical fields, $\boldsymbol{F}_1$and $\boldsymbol{F}_2$ with frequencies ω_1 and ω_2, with energies much lower and comparable to the bandgap, respectively. By summing the overall interband and intraband transitions, the linear optical response to the input field, $\boldsymbol{F}_2$, can be written as (Wang 2010),

$$\boldsymbol{P}^{(1)} \propto \boldsymbol{s_k}(xy - yx) \cdot \boldsymbol{F}_2 = \boldsymbol{F}_2 \times \boldsymbol{s_k}, \tag{6.20}$$

where $\boldsymbol{s_k}$ is the spin polarization. The Eq. (6.20) means, the linear polarization of the output field is related to the input field and the spin polarization, essentially a Faraday rotation due to the spin. (Wang 2010)

When the effect of the intraband driving by $\boldsymbol{F}_1$is included, the optical response can be written as

$$\boldsymbol{P} \propto \boldsymbol{F}_2 \times \boldsymbol{s_k} e \boldsymbol{v_k} \cdot \boldsymbol{F}_{1,} \tag{6.21}$$

where $\boldsymbol{v_k} = \frac{\boldsymbol{k}}{m_e}$ is the velocity of the electron with momentum, $\boldsymbol{k}$ and $e\boldsymbol{v_k} \cdot \boldsymbol{F}_1$, is the work done by the field to the electron (Wang 2010). Thus, if the electrons are driven by an optical field, the work done by the intraband acceleration leads to opposite renormalizations to the interband transition frequencies at opposite momenta because at any particular instant of time, one electron accelerates while the other decelerates. Thus, the Faraday rotation caused by the two electrons will not exactly be cancelled off which leaves a net second-order nonlinear optical susceptibility in the system. (Wang 2010)

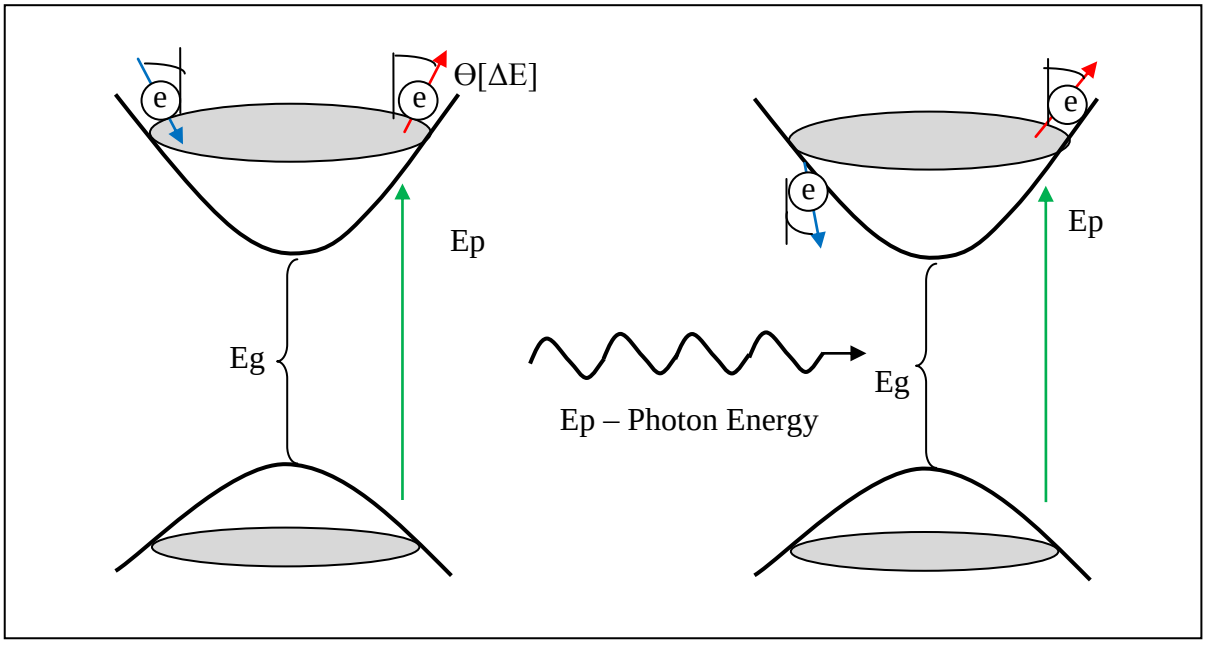

Figure 6.5: Faraday rotation of a pair of electrons in PSC. The rotation angle is a function of the excess energy of electrons. Left panel - the Faraday rotation angles of the both electrons are the same because they carry similar amounts of energies. Right panel – the Faraday rotation angles of the two electrons are different at every instant.

Left-panel of Fig. 6.5 shows for a PSC, the detuning of the spin-up and spin-down electrons are the same; thus the Faraday rotation angles are the same therefore the system is centrosymmetric. Right panel of Fig. 6.5 shows the effect of the optical field, E_P, changes the detuning of the two electrons. Therefore, the Faraday rotation angles are not the same.

This effect can be used for non-invasive, non-destructive and real-time imaging of PSCs in semiconductor nanostructures.

6.3.3 Electric-field induced second-harmonic generation

Similar to PSC and PCC, an applied DC electric field can also break the inversion symmetry in the subsurface space-charge region and induce SHG. This is a result of the initial band bending and/or external bias.

The first observation of DC electric field induced SHG (Terhune 1962) is reported in a calcite crystal which naturally possesses a center of inversion. The similar SHG is observed in non-dipolar fluids such as H_2, O_2 and CCl_4 as well as in dipolar fluids such as CO, $CHCl_3$ and other methyl halogeno-derivatives (Mayer 1968) and in inert gases. (Finn 1971)

In the presence of the DC electric field in a material, the second-order nonlinear polarization can be written as

$$\boldsymbol{P}^{NL} = \boldsymbol{P}^{S} + \boldsymbol{P}^{BQ} + \boldsymbol{P}^{BDE}, \tag{6.22}$$

where $\boldsymbol{P}^{S}$, $\boldsymbol{P}^{BQ}$ and $\boldsymbol{P}^{BDE}$ are the surface nonlinear polarization, bulk quadrupole contribution and the bulk DC electric field induced polarizations respectively. (Lee 1967; Aktsipetrov 1996)

DC electric field induced SHG method is used for characterization of silicon-electrolyte and silver-electrolyte buried interface or any other semiconductor-insulator and semiconductor-metal buried interface which are inaccessible to other surface sensitive techniques. (Terhune 1962; Lee 1967) As a promising noninvasive and in-situ method to monitor the imperfections at the interface of Si-SiO_2, the most important interface in the semiconductor technology, DC electric field induced SHG had been intensively studied for the last few decades.

In this chapter, we discussed the principles of SHG and the driving forces of inducing SHG. In the next chapter, we will discuss the experimental details and the data analysis of our approach of PSC, PCC and carrier population induced SHG.

Chapter 7

Carrier transport studied by second-harmonic generation technique

In chapter 6, I have discussed the principles of intrinsic second-harmonic generation, and then the different types of extrinsic second-harmonic generation process. In this chapter, I will present my experiments on observing the extrinsic second-harmonic generation by the pure spin current, pure charge current, and show that these processes can be used to directly detect these currents in semiconductors.

7.1 Coherent detection

Since the second-harmonic signals induced by the currents are expected to be very weak, we take the advantage of the fact that it is coherent, and used a coherent detection scheme to amplify the signal.

In the coherent control technique, we measure the resulting signal in the experiment by mixing it with another optical field (called a local oscillator) with the same frequency but with a much larger amplitude than the signal. (Hobbs 2009) In our experiment, as the inversion symmetry of the sample (GaAs 400 nm think bulk structure) is broken at the surface, there exist a second-harmonic light generation at the sample surface. We use this surface second-harmonic as a natural local oscillator (LO).

The time-averaged power density of an electromagnetic wave is called the intensity, *I*. (Griffiths 2004) In terms of ε_0, the permittivity of free space and c, the speed of light,

$$I = \frac{c\varepsilon_0}{2} E^2 . \tag{7.1}$$

The total optical field consists of two components, E_{LO} and E_J, the electric field of the local oscillator and the electric field of the second-harmonic induced by the currents. The total intensity can be written as

$$I = \frac{\varepsilon_0 c}{2} (E_{LO} + E_J)^2 . \tag{7.2}$$

By expanding the terms in the parenthesis,

$$I = \frac{c\varepsilon_o}{2}[E_{LO}^2 + 2E_{LO}E_J + E_J^2],$$

$$= I_{LO} + \Delta I\,. \tag{7.3}$$

where

$$I_{LO} = \frac{c\varepsilon_0}{2}E_{LO}^2 \tag{7.4}$$

is the intensity of the local oscillator alone and

$$\Delta I = \frac{c\varepsilon_0}{2}\left(E_J^2 + 2E_{LO}E_J\right) \tag{7.5}$$

is the change of the total second-harmonic intensity caused by the second-harmonic induced by the currents.

The time averaged power corresponding to these two terms can be measured separately by using different modulation schemes. To measure the power of the local oscillator, the probe beam is chopped and the corresponding lock-in voltage is converted back to the optical power at the photodiode. The pump pulses were blocked in order to ensure there is no contribution from the second term in Eq. (7.3). The voltage at the lock-in amplifier,

$$V = PG\eta\,, \tag{7.6}$$

where, *P* is the power of the light falls on to the photodiode, *G* is the gain settings of the detector (no units) and η, the quantum efficiency of the detector at the particular wavelength of the probe beam. In determining the value of *P* emitted by the sample, we have also considered all the losses in the propagation to the detector, which is calibrated experimentally by sending a beam with a known power.

The time averaged power corresponding to ΔI, ΔP is measured by modulating the relative phase of the two pump pulses, that is, by modulating the injected current density. The additional SHG is induced when there is a current in the sample and the corresponding lock-in voltage is measured. Similarly, the value of ΔP is calculated by converting the corresponding voltage in to power. We found that ΔP is approximately two orders of magnitude smaller than the P_{LO}.

Therefore, in Eq. (7.5), $E_J^2 <<< 2E_{LO}E_J$. This means, the local oscillator is much stronger than the signal. Thus, approximately, we have,

$$\Delta P \propto E_J . \tag{7.7}$$

Since

$$E_J \propto \chi_J^{(2)} \propto J , \tag{7.8}$$

there is a linear relationship of the change of the second-harmonic power induced by the current (ΔP) and the current density (J). In our experiments, we can measure ΔP as a function of the probe delay and the relative position of the probe spot with respect to the pump spots.

7.2 Pure spin current induced second-harmonic generation

As PSC does not carry a net charge current or a net magnetization, it does not involve an electromagnetic induction. Previously, the observation of PSC in our lab (Ruzicka 2009, Loren 2009) as well as in many other groups (Loren 2009; Zhao 2006; Kato 2004; Wunderlich 2005; Stevens 2003) were done by detecting the accumulation of spin-up and spin-down electrons, which is caused by the spin transport. In addition, it is also possible to convert the spin current to electrical signals. (Kane 2005; Ganichev 2007; Cui 2007; Appelbaum 2007). These are both indirect techniques, in the sense that not the spin current itself, but rather some effects of the PSC, are detected. For example, the spin accumulation is related to the PSC, but does not reflect the state of the PSC in a real-time frame. Therefore, it is desirable to have a technique that directly senses the PSC, with a measureable quantity that directly reflects the density of the PSC.

7.2.1 Experimental setup

Figure 7.1 shows the experimental configuration we used to demonstrate the SHG induced by PSC. The ω pulse with a central wavelength of 1500 nm is obtained directly from the signal output of the OPO and 2ω pulse with a central wavelength of 750 nm is obtained by SHG of the 1500 nm pulse with a BBO crystal. The orthogonally linearly polarized pulses are separated by a dichroic beamsplitter; thus the polarizations, the powers and the phases can be controlled independently. The 750 nm pulse is sent through an electro-optic crystal in order to modulate its phase. A Treacy grating pair is used to partially compensate for temporal broadening of the 750 nm pulse caused by the elector-optic crystal and other optics. The pulses are combined by using another dichroic beamsplitter, and then focused to the GaAs sample by a microscope objective lens with a numerical aperture of 0.26.

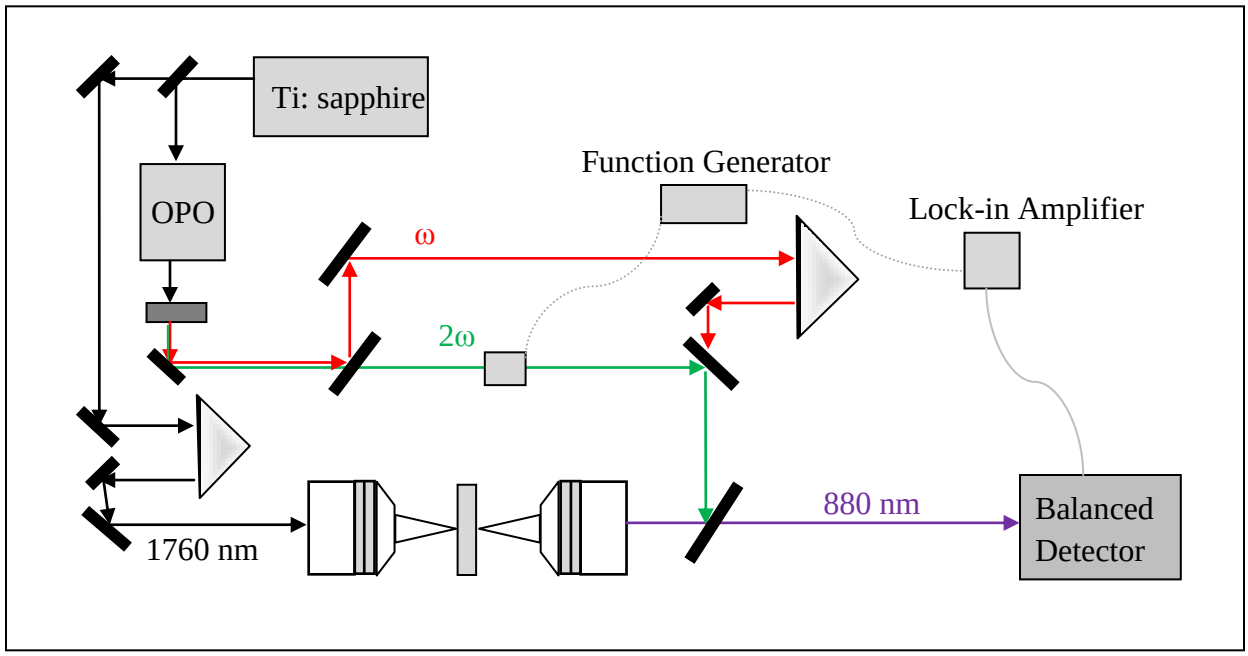

Figure 7.1: The schematic diagram of the apparatus configuration for inducing second-harmonic light by PSC. The pump pulses, orthogonally, linearly polarized ω and 2ω are used to inject PSC in the sample and the generated second-harmonic light of the probe pulse is collected using a Si-photodiode.

The sample is kept at 10 K in a closed-cycle cryostat (Advanced Research Systems). The 750 nm pulse has a spot size of 1.9 μm (FWHM), injecting carriers with a density profile of the same size through one-photon absorption. Since the 1500 nm pulse injects carriers through two-photon absorption, the carrier density profile produced is a factor of $2^{0.5}$ narrower that the laser intensity profile. Therefore we set the spot size of the 1500 nm pulse to 2.6 μm, such that the two pulses produce the same size of carrier density profiles.

The temporal width of the ω pulse is close to transformation limited 75 fs, because the dispersion of most optical materials is negligible at that wavelength. The 2ω pulse has a temporal width of 290 fs, even after dispersion compression. The polarization of the each pulse is controlled by a series of wave-plates and polarizers. To inject a PSC with velocities along $\hat{x}$ direction and spin orientations along $\hat{z}$ direction, the 1500 nm and 750 nm pulses are linearly polarized along $\hat{x}$ and $\hat{y}$ directions, respectively.

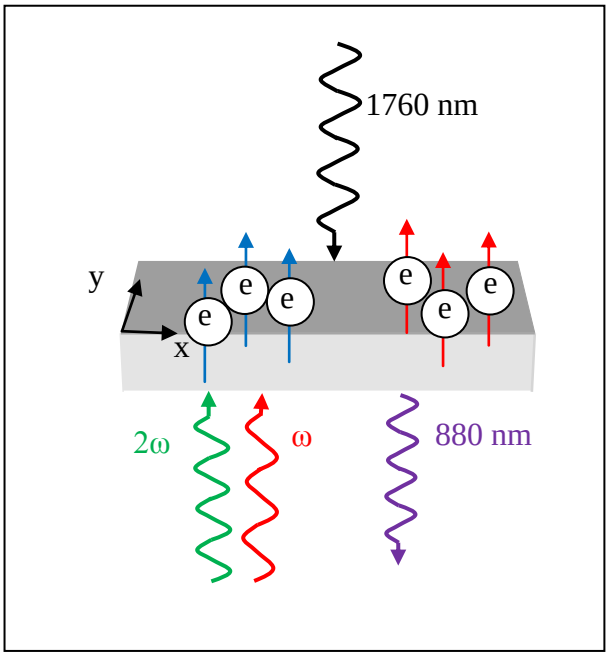

Figure 7.2: Illustration of the input and output beams near the sample. The ω and 2ω serve as the pump pulses. The probe pulse, 1760 nm and the PSC induced second-harmonic pulse of the probe pulse (purple - 880 nm) propagate in $\hat{z}$ direction.

As shown in Fig. 7.1, the probe pulse with a central wavelength of 1760 nm is obtained from the idler output of the OPO, and is focused to the sample by another objective lens with a numerical aperture of 0.4. The spot size and the temporal width at the sample are 2.1 μm and 170 fs, respectively. The generated second-harmonic pulse with a central wavelength of 880 nm is collimated and detected as a function of the probe delay, spatial position, and the relative phase. Figure 7.2 shows all of the four beams near the sample.

We measured the ΔP as a function of three controllable parameters in our experiments using the coherent detection scheme. 1) The time delay between the peaks of the probe and the current-injecting pulses, τ; 2) the distance between the centers of the probe and the current-injecting spots, x; and 3) the relative phase, $\Delta\phi$. Figure 7.3 shows the ΔP as a function of the probe delay and the relative phase at fixed probe position, $x = 0$.

The upper panel of Fig. 7.3 shows, ΔP as a function of both probe delay and relative phase with $x = 0$. In the lower-left panel, at $\tau = -0.06$ ps, the ΔP is plotted as a function of the relative phase. The cosine dependence is consistent with the theoretical prediction that the $\chi^{(2)}$ is proportional to the current density. In the lower-right panel, with a certain relative phase and a probe position, $x = 0$, ΔP is plotted as a function of the probe delay. The ΔP increases to a peak at about $\tau = -0.06$ ps, and then decays rapidly. This temporal behavior indicates that the relaxation time of the spin current is shorter than the laser pulses at such a high carrier density.

Figure 7.4 shows the change of ΔP as a function of the space position and the relative phase at fixed $\tau = -0.06$ ps. At each point, ΔP has a Gaussian-like spatial profile, consistent with the size and the shape of the laser spots (lower-left panel). The blue line is a Gaussian fit of the data. The same cosine dependence on the relative phase is observed at every probe position (lower-right panel).

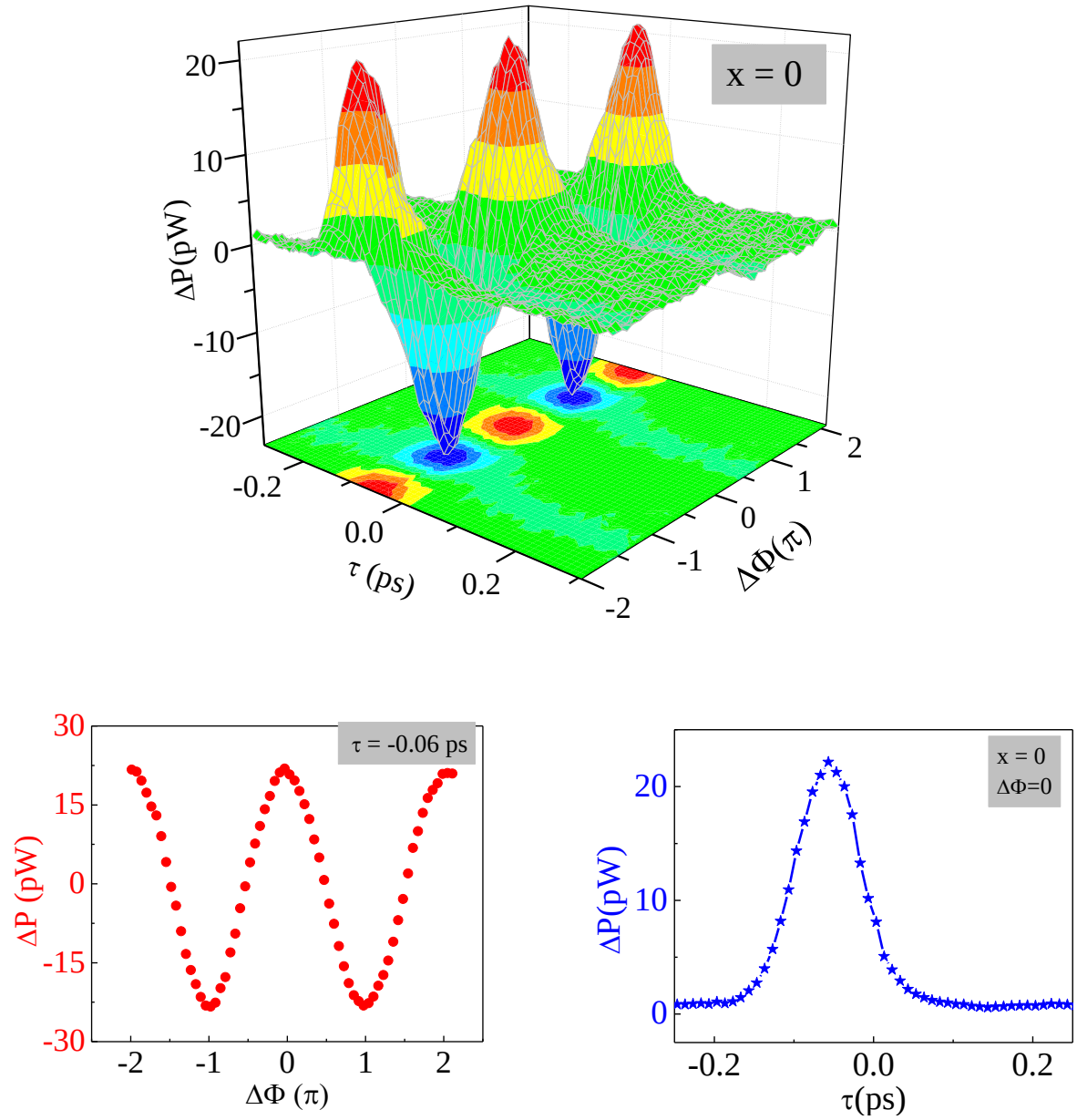

Figure 7.3: The SHG induced by PSC with the probe and pumps overlapped at $x = 0$. (Top panel) The ΔP measured as a function of τ, and $\Delta\phi$. The cross sections of the graph in the top panel with $\tau = -0.06$ ps (left-lower panel) and $\Delta\phi = \pi$ (right-lower panel). (Werake 2010)

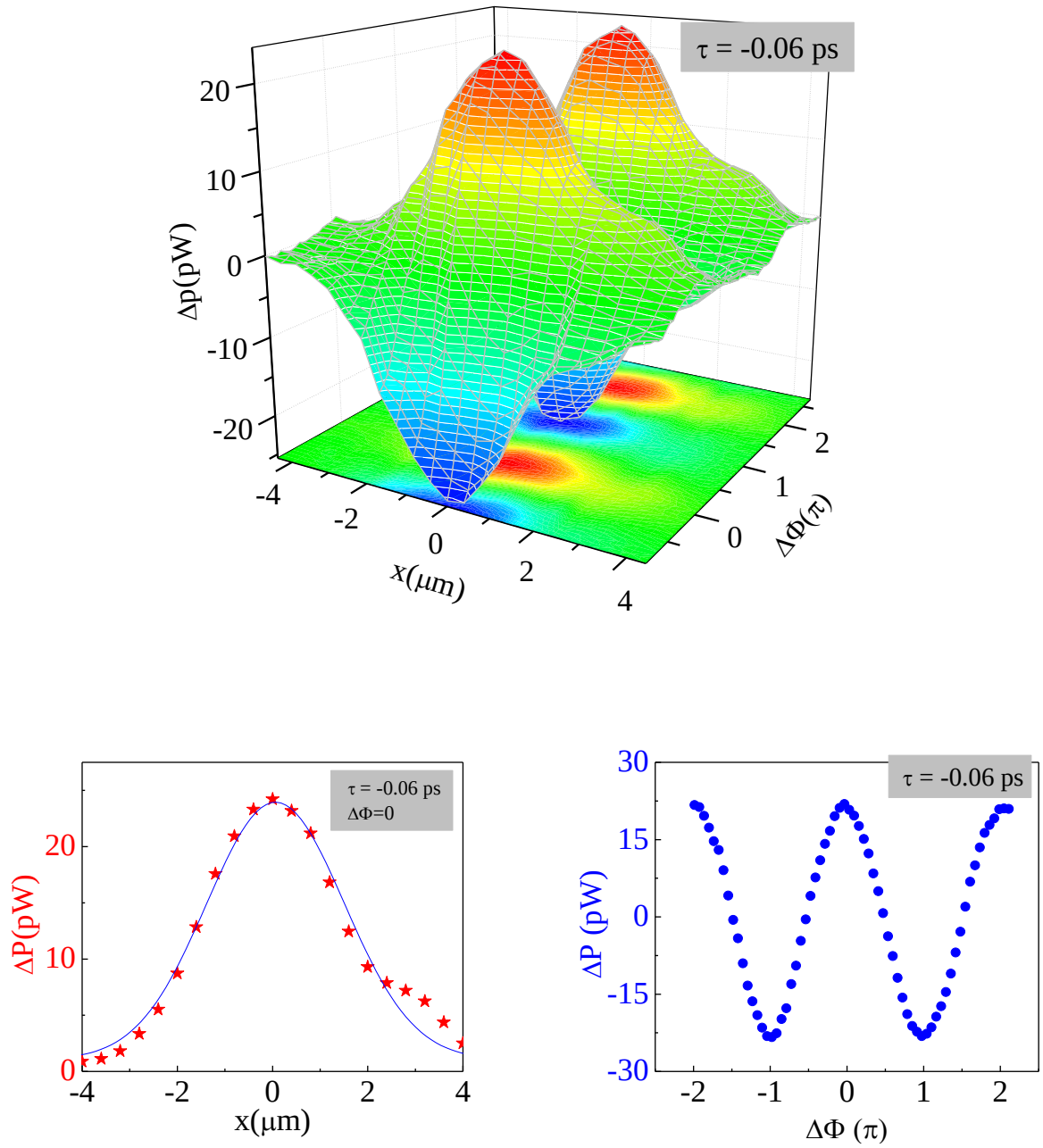

Figure 7.4: The SHG induced by PSC at fixed $\tau = -0.06$ ps. (Top panel) The ΔP as a function of space, x and $\Delta\phi$. The cross sections of the graph in the top panel with $\Delta\phi = 0$ (left-lower panel) and $x = 0$ (right-lower panel). (Werake 2010)

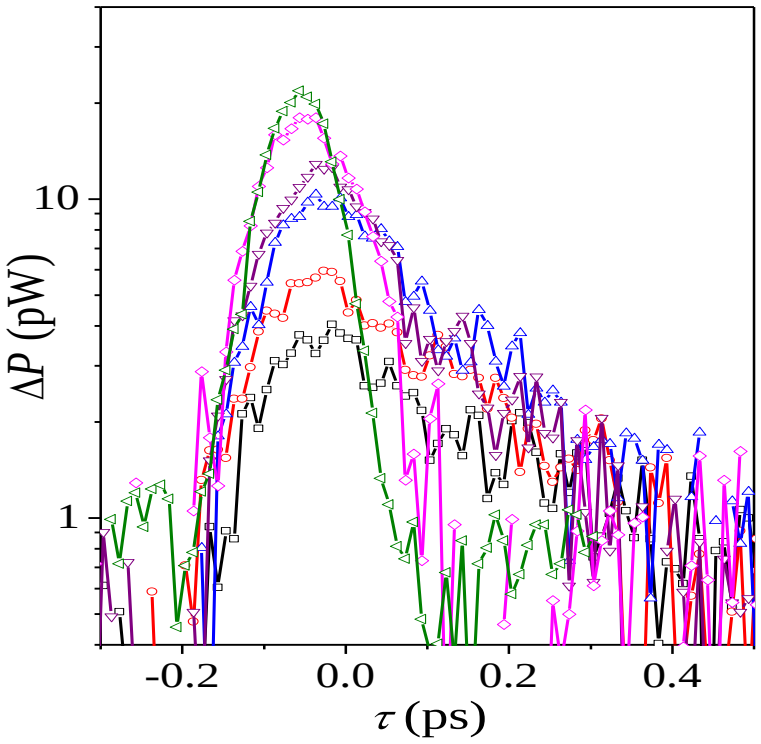

Figure 7.5: The power of SHG as a function of carrier density ($3.6\times10^{17}cm^{-3}$ in black-up triangles, $4.8\times10^{17}cm^{-3}$ in red-solid circles, $6\times10^{17}cm^{-3}$ in blue stars, $7.2\times10^{17}cm^{-3}$ in purple stars, $9.6\times10^{17}cm^{-3}$ in pink-solid square, $11.5\times10^{17}cm^{-3}$ in green-up triangles. (Werake 2010)

The measurements described above are repeated with different carrier densities by adjusting the power of the current-injecting pulses. In this way the injected current density is varied by changing the carrier density, while the average velocity is kept unchanged. A few examples are shown in Fig. 7.5. As the carrier density increases, the peak of ΔP shifts to earlier probe delays and the decay becomes faster. The height of the peak is determined by both the injection and the relaxation processes of the PSC. As the carrier densities increases, owing to the faster scattering rate the PSC relaxes faster.

Figure 7.6 shows the height of the peak increases linearly with the carrier density. The slight deviation from a linear relation can be attributed to the fact that, although the injected

current density is proportional to the carrier density, the current relaxes faster with higher densities.

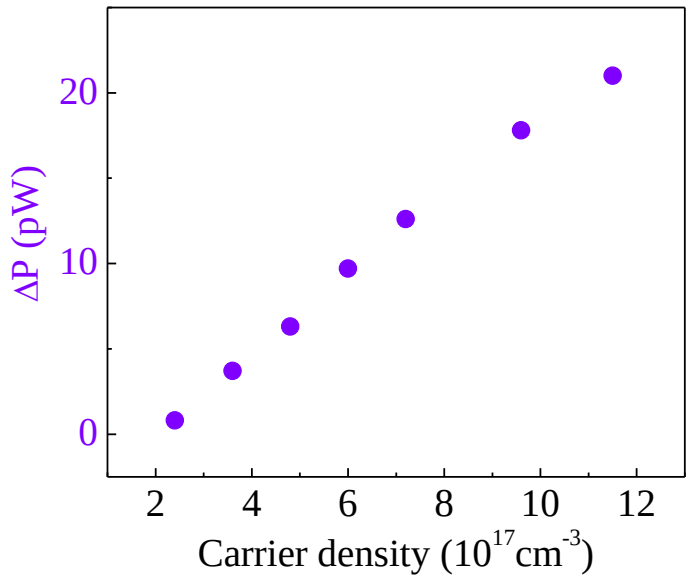

Figure 7.6: Linear dependence of the power of the SHG driven by PSC with the carrier density (Werake 2010).

Using the measured data, the $\chi^{(2)}$ is calculated as follows. Let us write the amplitude of the electric field of the LO,

$$E_{LO} = A_{LO}E_P^2, \tag{7.9}$$

where E_P is the field amplitude of the probe pulse (1760 nm) and

$$A_{LO} = \frac{e\epsilon_0}{2}\frac{I_{LO}}{I_P^2}, \tag{7.10}$$

with $I_P$as the intensity of the probe. The field amplitude of the current-induced second-harmonic can be written as

$$E_J = A_J E_P^2, \tag{7.11}$$

where

$$A_J = \frac{\pi L \chi_J^{(2)}}{n^2 \lambda}. \tag{7.12}$$

Here, L and n are the thickness and the index of refraction of the sample, respectively and λ is the wavelength of the second-harmonic in a Vacuum. Substituting Eq. (7.9) in Eq. (7.4) gives,

$$I_{LO} = \frac{c\epsilon_0}{2} A_{LO}^2 E_P^2, \tag{7.13}$$

and

$$\Delta I = \frac{c\epsilon_0}{2} (2A_{LO}A_J + A_J^2) E_P^4 \approx \frac{c\epsilon_0}{2} (2A_{LO}A_J) E_P^4. \tag{7.14}$$

Using Eqs. (7.13) and (7.14),

$$\frac{\Delta I}{I_{LO}} = \frac{2A_J}{A_{LO}}. \tag{7.15}$$

Finally, considering Eqs. (7.10), (7.12) and (7.15), the current induced $\chi_J^{(2)}$ can be written as

$$\chi_J^{(2)} = \left(\frac{n^2\lambda}{2\pi L}\right)\left(\frac{\Delta I}{I_{LO}}\right)\left(\frac{c\epsilon_0}{2}\right)^{1/2}\left(\frac{I_{LO}^{1/2}}{I_P}\right). \tag{7.16}$$

Each intensity, ΔI, I_P and I_{LO} is a Gaussian function of time. The peak intensities can be calculated from the experimentally determined time-average powers, ΔP, P_P and P_{LO} using the relation,

$$I \approx \frac{P}{f\tau\pi w^2}, \tag{7.17}$$

where f, τ and w are the repetition rate of the laser, the temporal width of the pulse and the width of the laser spot.

The demonstrated second-order nonlinear optical effect is large enough to detect low-density spin currents. We choose the probe photon energy to be less than half of the energy bandgap of the sample, so that neither the two-photon absorption of the probe pulse nor the one-photon absorption of the second-harmonic pulse is allowed. Therefore, the probe pulse will not disturb the spin current by injecting extra carriers. However, one could tune the probe photon

energy towards the interband transition frequency of the electrons to increase $\chi^{(2)}$. In our experiments, a higher repetition-rate (82 MHz) laser system is used. With high-density spin currents of the order of 10^5 A cm^{-2}, the probe beam with an average power of 10mW generates second-harmonic signals of the order of 10 pW. Owing to the quadratic dependence of the second-harmonic field amplitude on the probe field amplitude, the SHG process can be significantly enhanced with amplified laser systems with lower repetition rates. For example, a 1-kHz laser system with the same average power (commercially available) will increase the second-harmonic power by about five orders of magnitude.

From the experiments, we have $P_P = 10$ mW, $P_{LO} = 4$ nW, and $\Delta P = 20$ pW (corresponding carrier density of 2.4×10^{17}cm^{-3} and current density of 10^5Acm^{-2}). Using Eq. (7.17), with $f = 80$ MHz, $\tau = 170$ fs, and w = 2.1 μm, the intensities can be calculated as, $I_P = 5.3\times10^{12}$Wm^{-2}, $I_{LO} = 2.4\times10^5$ Wm^{-2} and $\Delta I = 1.5\times10^2$ Wm^{-2}, respectively. With all the calculated intensities and $n = 3.6$, $\lambda = 880$ nm, $L = 400$ nm, $c = 3\times10^8$ ms^{-1}, and $\epsilon_0 = 8.85\times10^{-12}$ C^{2}N^{-1}m^{-2}, Eq. (7.16) gives, $\chi_J^{(2)} \approx 0.079$ pm V^{-1}.

7.3 Pure charge current induced second-harmonic generation

As discussed in Sec. 6.2, PCC can induce SHG by breaking the symmetry in a system. In this section, the experimental results of the PCC induced SHG are discussed.

Lineally polarized ω and 2ω pump pulses are used to inject PCC in the GaAs 400 nm thick bulk sample. The rest of the experimental details and the setup configuration are similar to Sec. 7.2.1 and Fig 7.1. The coherent detection scheme is also used to amplify the signal. Similar to Sec. 7.2, we measured the SHG induced by the PCC as a function of the probe delay, the relative phase and the probe postion. Finally the ΔP is measured as a function of the powers of ω and 2ω. The top panel of Fig. 7.7 shows the power of the induced SHG, ΔP, as a function of both probe delay and relative phase with $x = 0$. The two phase scans shown in the lower-left panel, at $\tau = 0.045$ ps and 0.22 ps, respectively are out phase by 90^o. The blue and red lines are the sinusoidal fits of the data. Thus the electrons are moving in opposite directions at these probe delays. The right-lower panel shows the ΔP as a function of the probe delay. It shows an oscillatory behavior which is a result of the separation of the electron-hole pair in space.

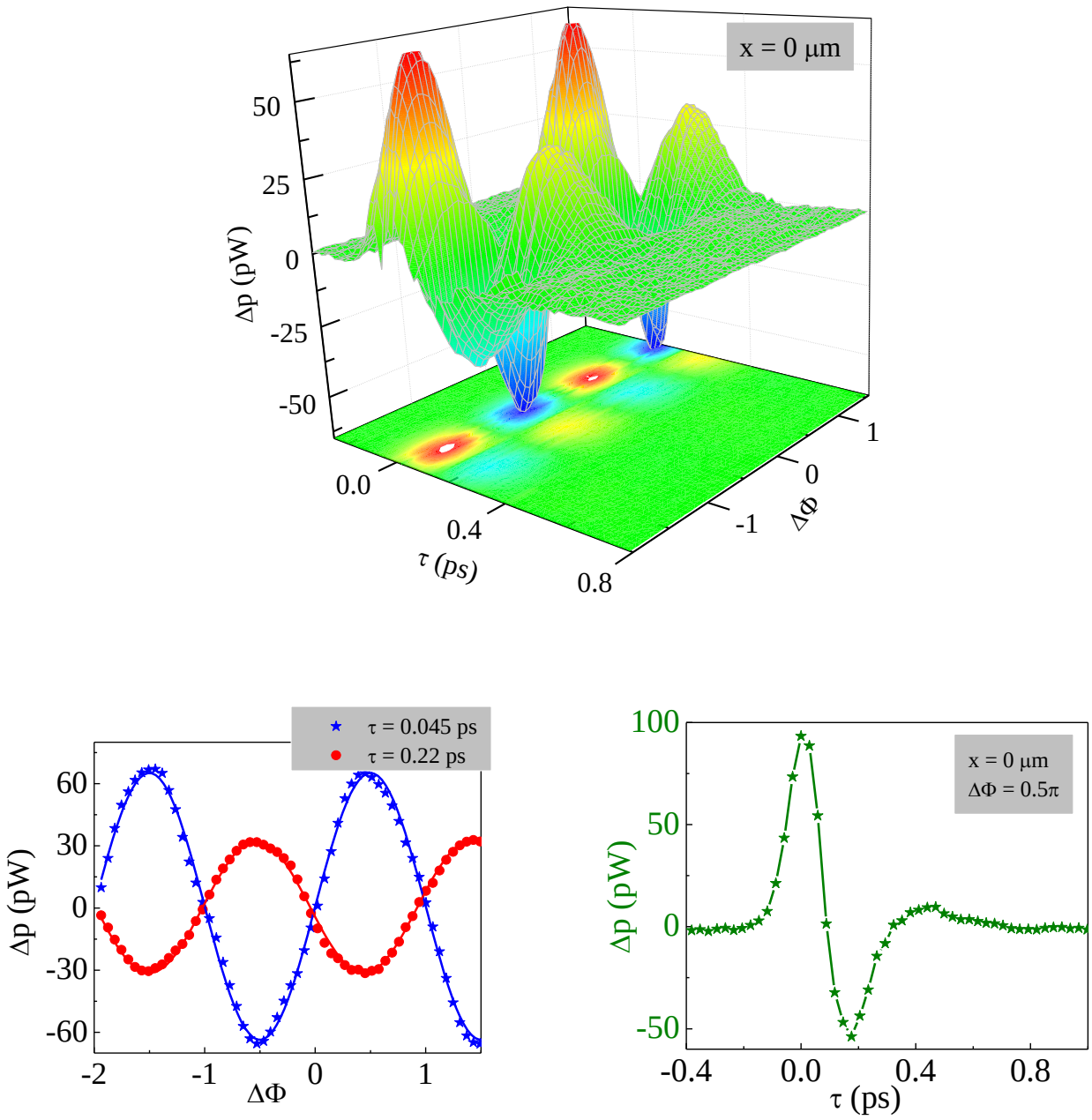

Figure 7.7: The SHG induced by PCC (upper panel). The power of the induced SHG, ΔP is graphed as a function of τ and $\Delta\phi$, with probe and pump pulses overlapped at $x = 0$ is analyzed. The cross section of the top panel with (lower-left panel) at $\tau = 0.045$ ps (blue stars) and 0.22 ps (red- solid circles) and (lower-right panel) $\Delta\phi = 0.5\,\pi$.

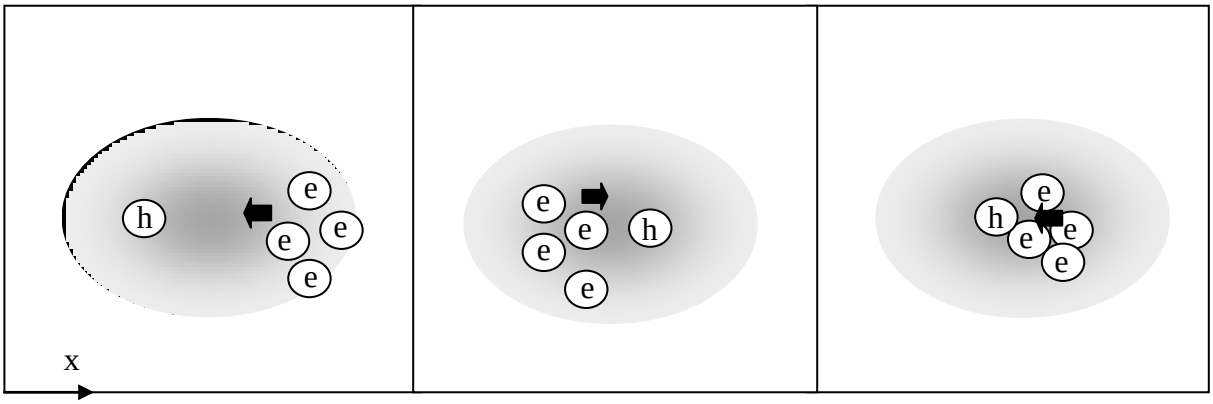

Figure 7.8: Illustrates the electrons oscillatory behavior in a medium. Upon the injection of a PCC, both spin-up and spin-down electrons move in $\hat{x}$ direction and the holes will move in $-\hat{x}$ direction. As holes are heavier than electrons, they have much smaller velocities than electrons. Thus, the electro-hole pair will separate in the space. Left-panel, the space-charge field develops and pulls electrons and holes back to a common origin. If the force is high, electrons will be over shoot, to the other opposite side as shown in the center panel and again electrons and holes will be pulled back. As shown in right panel, the electrons and holes will be pulled back to a common origin after another over shoot.

To understand the oscillatory behavior shown in Fig. 7.7, let us consider the dynamics of the carriers as plotted in Fig. 7.8. The electrons and holes are injected with opposite crystal momenta. Once they separate, a strongly nonuniform space-charge field develops which decelerates the carriers and causes the current density to drop. After the carriers reach their maximum displacement, the current density drops to zero. They are driven back towards the origin by the space charge field, giving rise to a negative current.

Although the charge current is accompanied by a space-charge field, we can safely rule out the latter as the cause of SHG: the space-charge field is proportional to the charge separation, and hence is delayed with respect to J by approximately a quarter period. We observed the peak SHG around zero probe delay. Such a lag had been confirmed in previous high-resolution pump-probe experiments, where the charge separation was found to reach a peak after more than 100 fs.

(Zhao 2008). Hence, the all-optical time-resolved technique has the advantage to unambiguously distinguish the field-induced and the current-induced SHG effect. This can be quite difficult in steady-state measurements where the current is proportional to the field.

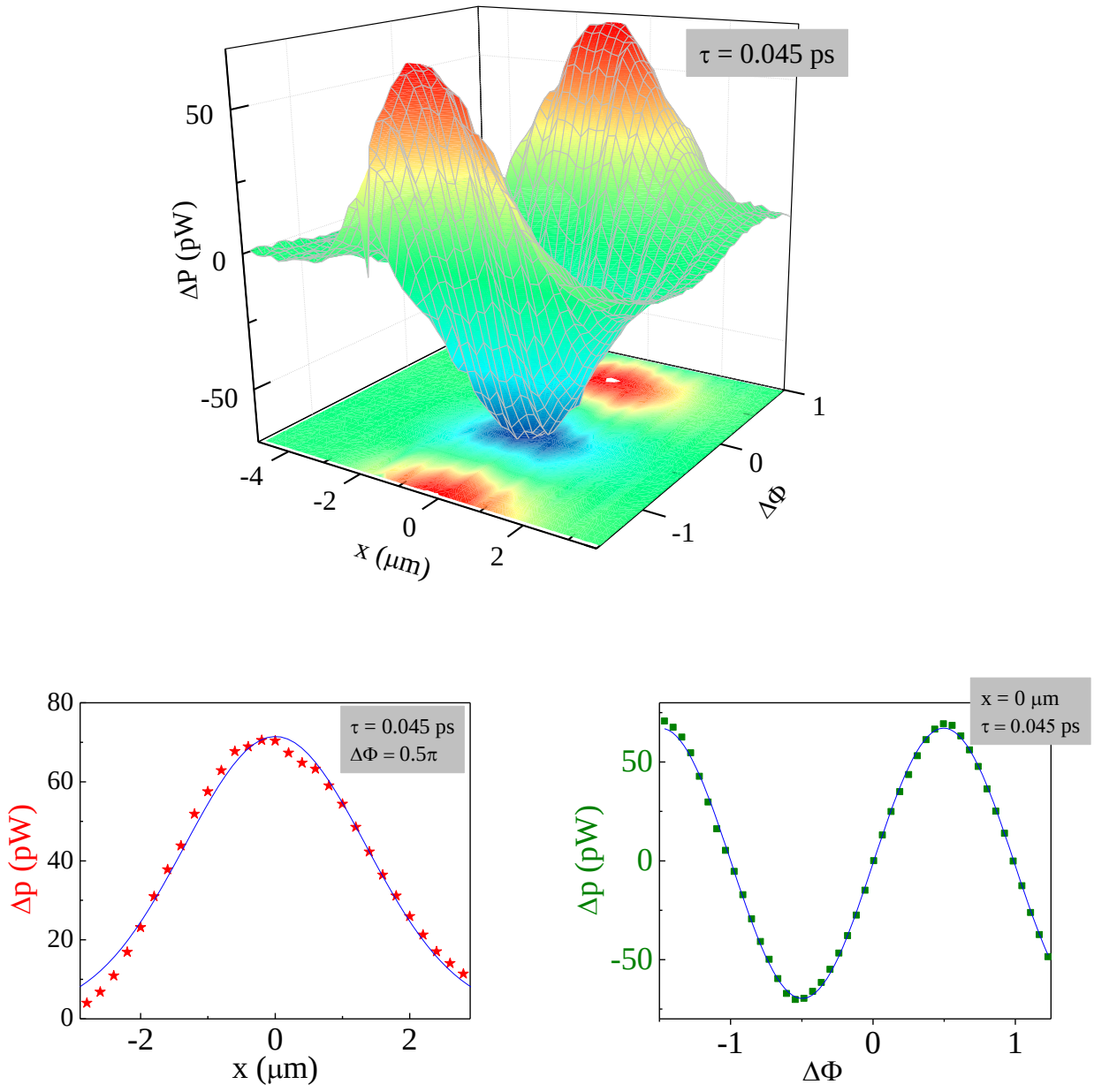

Figure 7.9: The SHG induced by PCC. (upper panel) the power of the induced SHG, ΔP is graphs as a function of both probe position in the space, x and the relative phase and the probe delay. Cross sections of the upper panel at $\Delta\phi = 0.5\pi$ (lower-left panel) and $x = 0$ (lower-right panel).

Figure 7.9 shows the measured experimental data of ΔP as a function of the probe position, and the relative phase at fixed $\tau = 0.045$ ps. The top panel shows the power of induced SHG as a function of the spatial position of the probe along $\hat{x}$ direction and the relative phase. The left-panel of Fig. 7.9 shows the spatial profile of ΔP with fixed phase and probe delay. It has a Gaussian shape, which is consistent with the laser spots. The blue line is a Gaussian fit of the data. The lower right-panel of Fig. 7.9 shows the expected sinusoidal phase dependence in the injection process of the PCC and the blue line represents a sinusoidal fit of the data.

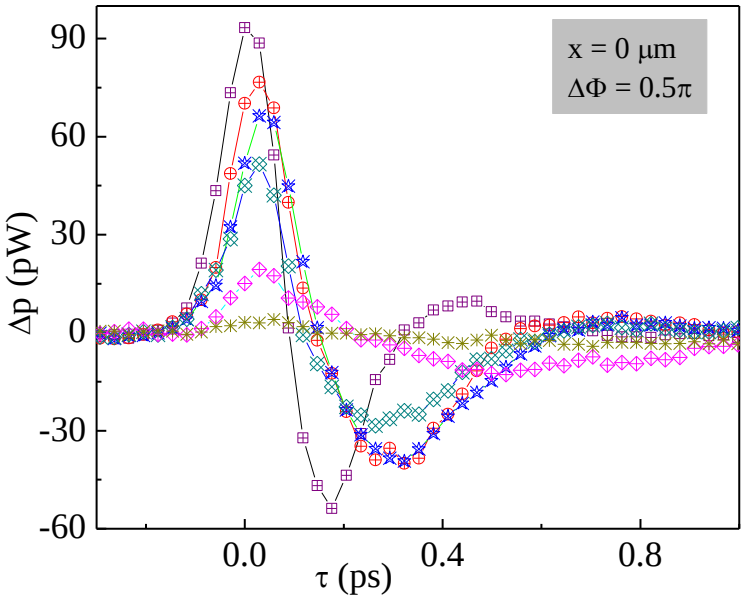

Figure 7.10: The ΔP is graphed as a function of the carrier density. (purple squares) 5.2×10^{16} cm^{-3}, red circles) $4.3\times10^{16}cm^{-3}$, blue stars) $3.5\times10^{16}cm^{-3}$, (crossed squares) $2.6\times10^{16}cm^{-3}$, (pink diamonds) $1.7\times10^{16}cm^{-3}$, (brown-double cross) $0.9\times10^{16}cm^{-3}$.

Figure 7.10 shows the ΔP of the induced SHG as a function of the carrier density of the PCC. The measurements are taken at $x = 0$ μm and $\Delta\phi = 0.5\pi$. As the carrier density increases, the peak of the ΔP shifts to left. The height of the peak of the induced SHG determines by both the injection and the relaxation of the PCC. As the carrier density increases, so does the rate of

scattering. Thus the charge current relaxation is faster. Therefore for higher carrier densities, the peaks shift to the left.

From the experiments, we have P_P=10 mW, P_{LO}= 4 nW, and ΔP = 90 pW (corresponding carrier density of 5.2×10^{16}cm^{-3}). Using the expression, (7.17), with f=80 MHz, τ=200 fs, and $w = 2$ μm, the intensities can be calculated as, I_P= 10^{14}Wm^{-2}, I_{LO}= 4×10^{7} Wm^{-2} and ΔI = 9×10^{5} Wm^{-2}, respectively. With all the calculated intensities and n = 3.6, $\lambda = 800$ nm, $L = 400$nm, $c = 3\times10^{8}$ ms^{-1}, and $\epsilon_0 = 8.85\times10^{-12}$ C^{2}N^{-1}m^{-2}, the Eq. (7.16) gives, $\chi_J^{(2)} \approx 0.183$ pm V^{-1}.

7.4 Carrier-induced second-harmonic generation

As explained in above sections, by introducing an external field to break the inversion symmetry, SHG is possible in centrosymmetric systems. It can be done by a PSC, PCC, and DC electric field. In addition to these, we have observed SHG induced by carrier populations in GaAs samples.

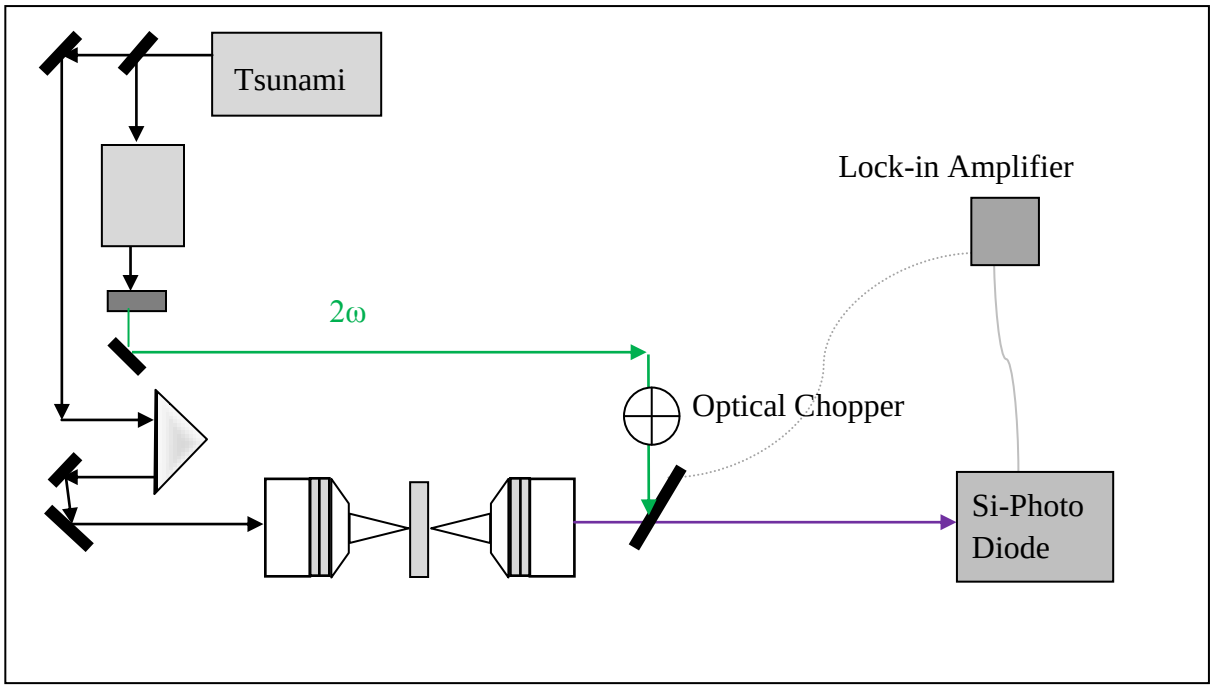

Figure 7.11: The Schematic diagram of the experimental setup.

The schematic diagram of the experimental setup is shown in Fig. 7.11. In our experiment, we used a GaAs 400 nm thick bulk structure at 8 K temperature. The ω pulse with a central wavelength of 1453 nm and a pulse width of 100 fs is obtained from the OPO pumped by the Ti:sapphire laser with a repetition rate of 82 MHz. The idler output of the OPO, with a wavelength of 1770 nm and a pulse width of 290 fs. The second-harmonic of the probe with a wavelength of 885 nm is directly collected using a photodiode. The output voltage of the photodiode was measured using a lock-in amplifier. Several color and interference filters are used to block unnecessary light reaching the photodiode; only the 885 nm light is detected.

The injection of electrons from the VB to the CB is done by one-photon absorption of the horizontally polarized, 2ω pulse with a central wavelength of 726 nm, which is generated by doubling the frequency of the ω pulse using a BBO crystal.

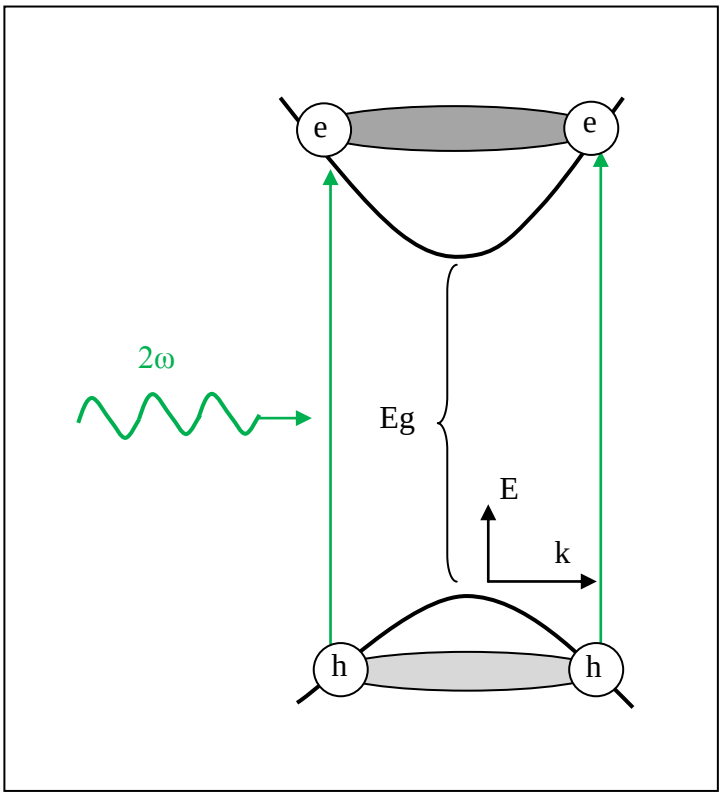

Figure 7.12: E-k diagram of one photon absorption of 2ω excitation of carriers. Electrons are excited from the VB to the CB while leaving holes in the VB.

As shown in Fig. 7.12, the single color excitations of carriers from the VB to the CB generate carrier populations and spin populations (if the pulse is circularly polarized), but not ballistic currents. The one photon absorption of a linearly polarized 2ω pulse create equal number of electrons in the $+\boldsymbol{k}$ and $-\boldsymbol{k}$ states and leave holes in the VB. As these electrons have opposite momenta in real space, they move oppositely. There is no net charge current. Moreover, when 2ω pulse is linear polarized, equal number of spin-up and spin-down electrons are excited, resulting in no net spin polarization.

Figure 7.13 shows the power of the induced SHG, (red-dotted circles) and the differential transmission of the 2ω pump pulse, (blue stars), as a function of the probe delay. The temporal behavior of the SHG shows a very slow raising time, approximately 15-20 ps, and a slower recombination time compared to the differential transmission.

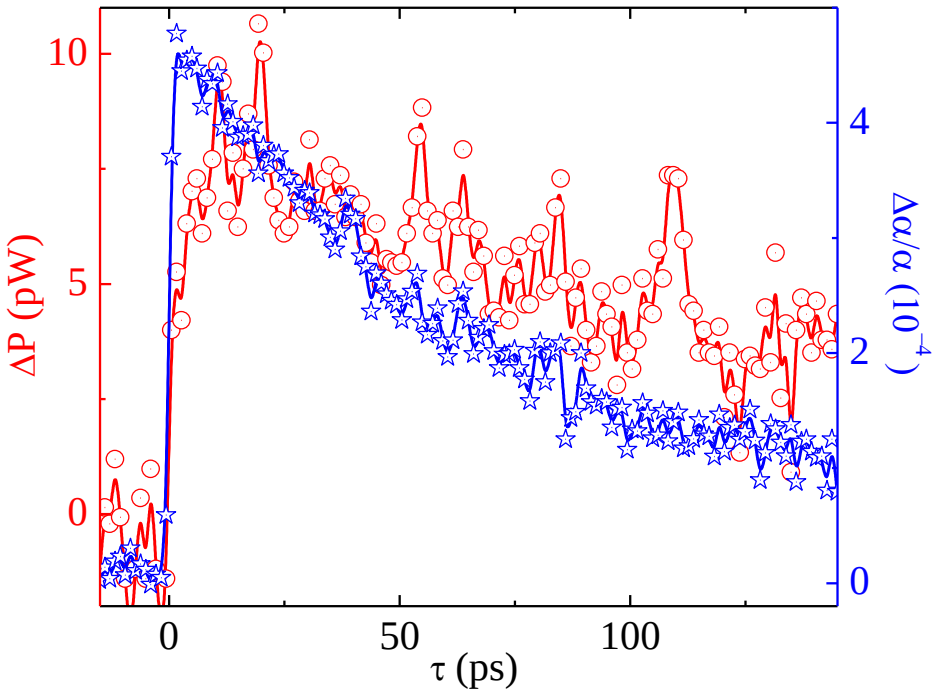

Figure 7.13: Graphical representation of (red-dotted circles) the carrier induced SHG and (blue–open stars) the differential transmission of the pump pulse as a function of the τ.

This temporal behavior of the SHG can be explained as follows. The sudden jump in the differential transmission of the probe at zero delay is induced by the carrier injection by the pump pulse. The decay of the signal shows the carrier recombination. During this process, same carriers can be trapped at the surface, which changes the property of the surface. Therefore the change of the total SHG reflects the amount of carriers trapped in the surfaces. The slow raising time shows the time for the carrier to be trapped. The slower decay time of the SHG signal shows that the lifetime of carriers in these traps are longer than those in the bulk.

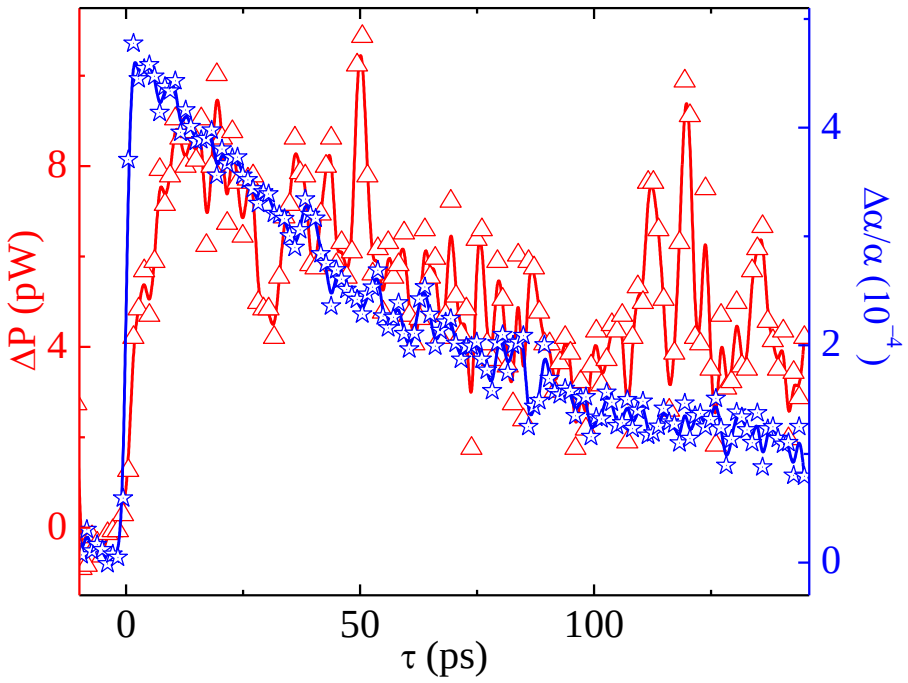

Figure 7.14: Graphical representation of the (red-open triangles) spin induced SHG and (blue–open stars) the differential transmission of the pump pulse as a function of the τ is shown.

In order to see if such a carrier-induced SHG is sensitive to the spin-polarization of the carriers, the measurement is repeated with a circularly polarization 2ω pulse instead a linearly polarized 2ω. Therefore, the one-photon absorption of 2ω pulse creates spin-polarized carriers.

The curve in red-dotted circles in Fig. 7.14 is similar to the curve in red triangles in Fig. 7.13 which means there is no significant difference between the linearly and circularly polarized pump pulses. Thus the spin density induced SHG is much smaller than the carrier density induced SHG.

Chapter 8

Summary

Anticipated data processing requirements in the coming decades are such that future electronic chips must have device-densities greatly in excess of the current value of approximately 4 million devices per chip. To achieve substantially greater densities, device features must be of the order of 10 nm or less. Since the device size has been reaching to its fundamental limits, the continuous reduction of the size to gain more space and power is no longer practical; thus the Moore law will clearly run out of its momentum in near future. As an alternate to accomplish the future desires in the information technology, the intrinsic angular momentum of the electron; the "spin" is considered as a promising candidate due to its potential possibility of achieving higher circuit density and consuming less energy in operation. Spintronics has achieved commercial success in some areas and is advancing towards additional applications that rely on recent fundamental discoveries. The injection, detection and manipulation of "spin" in to materials were recognized as high hurdles in the field previously but after years of research and development, they have solved the limitations to some extent. This dissertation is dedicated to study spin (and charge to some extent) transport in semiconductor nanostructures using ultrafast laser techniques.

In the first chapter, I have briefly introduced spintronics and semiconductor spintronics followed by a detailed explanation of the different techniques and the current status of spin transport. In the second chapter, I have discussed the different aspects of carrier transport phenomena in semiconductors. Both drift-diffusion and ballistics transport is introduced together with a definitions of the pure charge current and pure spin currents. In the third chapter, I have discussed the principles and configurations of the quantum interference and control technique which is the ballistic current injection technique we exploit in our experiments. Chapters 4, 5, 6, and 7 are devoted to the theories, experimental configurations and experimental data of the two spin transport techniques we developed.

In the fourth chapter, I have discussed the pump-probe technique as the first method of spin transport technique. Under sub topics of the chapter, I have discussed the principles of the technique by introducing the concepts of detecting carrier and spin densities with the

corresponding experimental configurations. Achieving high temporal and spatial resolutions are also discussed as sub topics in the chapter. In the fifth chapter, I have discussed the carrier transport studies done in group III-V and IV semiconductors using the pump-probe technique. Under sub topics of the chapter, I have discussed the observation of spin-polarized charge current and pure spin current in GaAs and Ge, respectively. The observation of the intrinsic spin-Hall effect in the inverse manner is also explained as in the chapter.

Chapters 6 and 7 are devoted to the details of the second-harmonic generation technique. In the sixth chapter, I have discussed the theories of both intrinsic and extrinsic second-harmonics generation. In the seventh chapter, I have discussed the coherent detection scheme and the experimental details of the pure spin current and pure charge current. I have also discussed our attempt to observe the carrier and spin density induced second-harmonics generation.

This dissertation is devoted to the spin (charge to some extend) transport studies in semiconductor nanostructure using ultrafast laser techniques. The efforts are made to study spin transport in different semiconductor nanostructures as well as to develop new techniques.

References

[Aktsipetrov 1994] Aktsipetrov, O., Fedyanin, A., Golovkina, V. and Murzina, T. (1994) "Optical Second-Harmonic Generation Induced by a DC Electric Field at the Si-$Si0_2$ Interface" Opt. Lett. **19** 18.

[Applebaum 2007] Appelbaum, I., Huang, B. and Monsma, D. (2007) "Electronic Measurement and Control of Spin Transport" Nature (London) **447** 295.

[Application note] Application note – 29 Technology and Application Center, Newport Corporation.

[Baibich 1988] Baibich, M. N. (1988) "Gaint Magnetoresistance of (001) Fe/(001) Cr Magnetic Superlattices" PRL **61** 21.

[Bernevig 2005] Bernevig, B. and Zhang, S. (2005) "Intrinsic Spin Hall Effect in the Two-Dimensional Hole Gas" Phys. Rev. Lett. **95** 01680.

[Bhat 2000] Bhat, R. and Sipe, J. (2000) "Optically Injected Spin Currents in Semiconductors" Phys. Rev. Lett. **85** 5432-5436.

[Boyd 2008] Boyd, R. W. "Nonlinear Optics and Applications" (2008) Elsevier publications USA.

[Cameron 1996] Cameron, A. R., Riblet, P., and Miller, A. (1996) "Spin Grating and Measurements of Electrons Drift Mobility in Quantum Well Semiconductors" Phys. Rev. Lett. **76** 4793.

[Carter 2006] Carter, S., Chen, Z. and Cundiff, S. (2006) "Optical Measurement and Control of Spin Diffusion in n-type Doped GaAs Quantum Wells" Phys. Rev. Lett. 97 136602

[Cho 2007] Cho, K.S. et al. (2007) "Spin-dependent Photocurrent Induced by Rashba-Type Spin Splitting in $Al_{0.25}Ga_{0.75}N$/GaN Heterostructures" Phys. Rev. B **75** 085327.

[Cho 2007] Cho, K., Chen, Y., Tang, Y. and Shen, B. (2007) "Photogalvanic Effects for Interband Absorption in AlGaN/GaN Superlattices" Appl. Phys. Lett. **90** 041909.

[Cho 2007] Cho, S., Chen, Y. and Fuhrer, M. (2007) "Gate-Tunable Graphene Spin Valve" Appl. Phys. Lett **91** 123105.

[Couto 2007] Couto, O. D. et al. (2007) "Anisotropic Spin Transport in (110) GaAs Quantum Wells" Phys. Rev. Lett. **98** 036603 1-4.

[Crooker 2005] Crooker, S. and Smith, D. (2005) "Imaging Spin Flows in Semiconductors Subject to Electric, Magnetic, and Strain Fields" Phys. Rev. Lett. **94** 236601 1-4.

[Cui 2007] Cui, X. D. et al. (2007) "Observation of Electric Current Induced by Optically Injected Spin Current" Appl. Phys. Lett. **90** 242115.

[Das Sarma 2000] Das Sarma, S., Fabian, J., Hu X. and Zutic, I. (2000) "Theoretical Perspectives on Spintronics and Spin-Polarized Transport" IEEE **36** 5.

[Datta 1990] Datta, S. and Das, B. (1990) "Electric Analog of the Electro-optic Modulator" Appl. Phys. Lett. **56** 7.

[Dietl 2007] Dietl, T. (2007) "Lecture Notes on Semiconductor Spintronics" arxiv:0801.0145v1.

[Diehl 2007] Diehl, H. et al. (2007) "Spin Photocurrents in (110)-Grown Quantum Well Structures" New Journal of Physics **9** 349.

[Diels 2006] Diels, J. and Rudolph, W. (2006) "Ultrashort Laser Pulse Phenomena – Fundamentals, Techniques, and Applications on a Femtosecond Time Scale" Elsevier.

[D'yakonov 2008] D'yakonov, M. (2008) "Spin Physics Semiconductors" Springer-solid state science.

[D'yakonov 1971] D'yakonov, M. and Perel V. (1971) "Possibility of Orienting Electron Spins with Current" JETP Letters **13** 467.

[Engel 2005] Engel, H. et al. (2005) "Theory of Spin Hall Conductivity in n-Doped GaAs" Phys. Rev. Lett. **95** 166605.

[Finn 1971] Finn, R. and Ward J. (1971) "DC-Induced Optical SHS in the Inert Gases" Phys. Rev. Lett. **26** 6 285.

[Flatte 2007] Flatte, M. E. (2007) "Spintronics" IEEE **54** 5.

[Franken 1961] Franken, P., Hill, A., Peters, C. and Weinreich, G. (1961) "Generation of Optical Harmonics" Phys. Rev. Lett. **74** 118.

[Ganichev 2001] Ganichev, S.D. et al. (2001) "Conversion of Spin into Directed Electric Current in Quantum Wells" Phys. Rev. Lett. **86** 4358.

[Ganichev 2000] Ganichev, S.D. et al. (2000) "Circular Photogalvanic Effect Induced by Monopolar Spin Orientation in p-GaAs/AlGaAs Multiple-Quantum Wells" Appl. Phys. Lett. **77** 3146.

[Ganichev 2003] Ganichev, S.D. et al. (2003) "Resonant Inversion of the Circular Photogalvanic Effect in n-Doped Quantum Wells" Phys. Rev. B **68** 035319.

[Ganichev 2007] Ganichev, S.D. et al. (2007) "Pure Spin Currents Induced by Spin-Dependent Scattering Processes in SiGe Quantum Well Structures" Phys. Rev. B **75** 155317.

[Giordmaine 1962] Giordmaine, J. A. (1962) "Mixing of Light Beams in Crystals" Phys. Rev. Lett **8** 19.

[Goto 2008] Goto, H. et. al. (2008) "Gate Control of Spin Transport in Multilayer Graphene" Appl. Phys. Lett. **92** 212110.

[Griffiths 2004] Griffiths, D. J. (2004) "Introduction to Electromagnetism" Prentice-Hall Inc NJ USA.

[Hall 2003] Hall, K., et al (2003) "Nonmagnetic Semiconductor Spin Transistor" Appl. Phys. Lett. **83** 2937.

[Hamaya 2007] Hamaya, K. et. al. (2007) "Spin Transport through a Spingle Self-Assembled As Quantum Dot with Ferromagnetic Leads" Appl. Phys. Lett. **90** 053108.

[Hammer 1999] Hammer, P., Bennet, B., Yang, M. and Johnson, M. (1999) "Observation of Spin Injection at a Ferromagnet-Semiconductor Interface" Phys. Rev. Lett. **83** 203.

[Hammar 2002] Hammar, P. and Johnson, M. (2002) "Detection of Spin-Polarized Electrons Injected into a two-Dimensional Electron Gas" Phys. Rev. Lett. **88** 066806.

[He 2007] He, X. W. et al. (2007) "Circular Photogalvanic Effect of the Two-Dimensional Electron Gas in $Al_XGa_{1-X}N$/GaN Heterostructures under Uniaxial Strain" Appl. Phys. Lett. **91**, 071912.

[Hirsch 1999] Hirsch, J. E. (1999) "Spin Hall Effect" Phys. Rev. Lett. **83** 1834-1838.

[Hobbs 2009] Hobbs, P. C. D. (2009) "Polarization in Building Electro-Optical Systems" Making it all Work" John Wiley.

[Huang 2007] Huang, B., Monsma, D. and Applebaum, I. (2007) "Experimental Realization of a Silicon Spin Field-Effect Transistor" Appl. Phys. Lett. **91** 072501.

[Haung 2007] Haung, B., Altfeder, I. and Applebaum, I. (2007) "Spin-Valve Phototransistor" Appl. Phys. Lett. **90** 052503.

[Huang 2007] Huang, B., Zhao, L., Monsma, D. and Applebaum, I. (2007) "35% Magnetocurrent with Spin Transport through Si" Appl. Phys. Lett. **91** 052501.

[Hubner 2003] Hubner, J. et al. (2003) “Direct Observation of Optically Injected Spin-Polarized Currents in Semiconductors” Phys. Rev. Lett. **90** 21.

[Hueso 2007] Hueso, L. et. al. (2007) “Transformation of Spin Information into large Electrical Signals using Carbon Nanotubes” Nature **445** 410.

[International Technology Roadmap for Semiconductors 2003] International Technology Roadmap for Semiconductors (2003) Semicond. Ind. Assoc. San Jose CA. Available: http://public.itrs.net

[Ivanov 2004] Ivanov, A., Aminov, T., Novotortsev, V. and Kalinnikov, V. (2004) “Spintronics and Spintronics Materials” Russian chemical bulletin, international edition **53** 11.

[Jensen 2005] Jensen, A., Hauptmann, J., Nygard, J. and Lindelof, P. (2005) “Magnetoresistance in Ferromagnetically Contacted Single-Wall Carbon Nanotubes” Phys. Rev. B **72** -35419.

[Jonker 2007] Jonker, B. et. al. (2007) “Electrical Spin-Injection into Silicon from a Ferromagnetic Metal/Tunnel Barrier Contact” Nat. Phys. **3** 542.

[Kane 1998] Kane, B. (1998) “A Silicon-based Nuclear Spin Quantum” Nat. **393** 133.

[Kane 2005] Kane, C. and Mele, E. (2005) “Quantum Spin Hall Effect in Graphene” Phys. Rev. Lett. **95** 22680.

[Kato 2004] Kato, Y., Myers, R., Gossard, A. and Awschalom, D. (2004) “Observation of the Spin Hall Effect in Semiconductors” Science **306** 1910.

[Khurgin 1995] Khurgin, J. B. (1995) “Current induced second harmonic generation in semiconductor” Appl. Phys. Lett. 67 1113.

[Kikkawa 1997] Kikkawa J. M and Awschalom (1997) “Lateral drag of spin coherence in GaAs” Nature **397** 139.

[Kimura 2007] Kimura, T. et al. (2007) "Room-Temperature Reversible Spin Hall Effect" Phys. Rev. Lett. **98** 156601.

[Kittle 1996] Kittel, C. "Introduction to Solid-State Physics" (1996) Wiley New York.

[Koo 2007] Koo, H. et. al. (2007) "Electrical Spin Injection and Detection in an InAs Quantum Well" Appl. Phys. Lett. **90** 022101.

[Lee 1967] Lee, C., Chang, R. and Bloembergen, N. (1967) "Nonlinear Electroreflectance in Silicon and Silver" Physical Review Letters **18** 5.

[Loren 2009] Loren, E. J. et al. (2009) "Optical Injection and Detection of Ballistic Pure Spin Currents in Ge" Appl. Phys. Lett. **95** 092107.

[Loren 2010] Loren E., Zhao, H. and Smirl, A. (2010) "All-Optical Injection and Detection of Ballistic Charge Currents in Ge" J. of Appl. Phys. **108** 083111.

[Loss 1998] Loss, D and DiVincenzo, D. (1998) "Quantum Computation with Quantum Dots" Phys. Rev. A. **57** 120.

[Lou 2006] Lou, X. el. al. (2006) "Electrical Detection of Spin Accumulation at a Ferromagnet-Semiconductor Interface" Phys. Rev. Lett. **96** 176603.

[Lou 2007] Lou, X. et. al. (2007) "Electrical Detection of Spin Transport in Lateral Ferromagnet-Semiconductor Devices" Nat. Phys. **3** 197.

[Maker 1962] Maker, P., Terhune, R., Nisenoff, M. and Savage, C. (1962) "Effects of Dispersion and Focusing on the Production of Optical Harmonics" Phys. Rev. Lett. **8** 1.

[Malajovich 2000] Malajovich, I. et al. (2000) "Coherent Transfer of Spin Through a Semiconductor Heterostructures" Phys. Rev. Lett. **84** 1015-1018.

[Malajovich 2001] Malajovich, I. Berry, J., Samarth, N. and Awschalom, D. (2001) "Persistent souring of coherent spins for multifunctional semiconductor spintronics" Nature **411** 77.

[Man 2006] Man, H., Wever, I. and Morpurgo, A. (2006) "Spin-Dependent Quantum Interference in Single-Wall Carbon Nanotubes with Ferromagnetiic Contacts" Phys. Rev. B. **73** 241401.

[Meier 1984] Meier and Zakharchenya (1984) "Optical Pumping in Semiconductors" Vol. 8 North-Holland Amsterdam.

[Mishchenko 2004] Mishchenko, E., Shytov, A. and Halperin, B. (2004) "Spin Current and Polarization in Impure Two-Dimensional Electron Systems with Spin-Orbit Coupling" Phys. Rev. Lett. **93** 226602.

[Moodera 1995] Moodera, J. et al (1995) "Large Magnetoresistance at Room Temperature in Ferromagnetic Thin Film Tunnel Junctions" PRL **74** 16

[Murakami 2003] Murakami, S., Nagaosa, N. and Zhang, S. (2003) "Dissipationless Quantum Spin Current at Room Temperature" Science **301** 1348.

[Murakami 2004] Murakami, S., Nagaosa, N. and Zhang, S. (2004) "Spin-Hall Insulator" Phys. Rev. Lett. **93** 156804.

[Nagabhirava 2006] Nagabhirava, B. et. al. (2006) "Gated Spin Transport through an Individual Signal Wall Carbon Nanotube" Appl. Phys. Lett. **88** 023503.

[Najmaie 2003] Najmaie, A., Bhat, R. and Sipe, J. (2003) "All-Optical Injection and Control of Spin and Electrical Currents in Quantum Wells" Phys. Rev. B **68** 165348.

[Nikolic 2005] Nikolic, B., Souma, S., Zarbo, L. and Sinova, J. (2005) "Nonequilibrium Spin Hall Accumulation in Ballistics Semiconductor Nanostructures" Phys. Rev. Lett. **95** 046601.

[Nishioka 2007] Nishioka, M. and Goldman, A. (2007) "Spin Transport through Multilayer Graphene" Appl. Phys. Lett **90** 252505.

[Palmer 2002] Palmer, C. (2002) “Hand Book of Diffraction Grating” 5th edition, Thermo RGL NY.

[Pi 2010] Pi, K., Han, W., K., McCreary, K., Swartz, A. and Kawakami, R. (2010) “Manipulation of Spin Transport in Graphene by Surface Chemical Doping” Phys. Rev. Lett. **104** 18.

[Popinciuc 2009] Popinciuc, M. et al (2009) “Electronic Spin Transport in Graphene Field-Effect Transistors” Phys. Rev. B **80** 214427.

[Prinz 1998] Prinz, G. A. (1998) “Magnetoelectronics” Science **282** 1660.

[Rougemaille 2008] Rougemaille, N. et. al. (2008) “Injection Energy Dependence of Spin-Polarized Hot-Electron Transport through a Ferromagnetic Metal/Oxide/Semiconductor Junction” Phys. Rev. B **77** 094409.

[Rulliere 2005] Rulliere, C. (2005) “Femtosecond Laser Pulses: Principles and Experiments” Springer New York.

[Ruzicka 2008] Ruzicka, B., Higley, K. Werake, L. and Zhao, H. (2008) “All-Optical Generation and Detection of Subpicosecond ac Spin Current Pulses in GaAs” Phys. Rev. B **78** 045314.

[Ruzicka 2009] Ruzicka, B. and Zhao, H. (2009) “Power Dependence of Pure Spin Current Injection by Quantum Interference” Physical Review B **79** 155204.

[Sahoo 2005] Sahoo, S. et. al. (2005) “Electric Field Control of Spin Transport” Nat. Phys. **1** 99.

[Sheng 2005] Sheng, L. and Yang, Z. (2005) “Intrinsic Spin and Orbital Angular Momentum Hall Effect” Phys. Rev. Lett. **94** 016602.

[Shen 2004] Shen, S., Ma, M., Xie, X. and Zhang, F. (2004) “Resonant Spin Hall Conductance in Two-Dimensional Electron Systems with a Rashba Interaction in a Perpendicular Magnetic Field” Phys. Rev. Lett. **92** 256603.

[Sih 2006] Sih, V. et al. (2006) "Generating Spin Currents in Semiconductors with the Spin Hall Effect" Phys. Rev. Lett. **97** 096605.

[Sih 2005] Sih, V., et al (2005) "Spatial Imaging of the Spin-Hall Effect and Current-Induced Polarization in Two-Dimensional Electron Gases" Nat. Phys. **1** 31.

[Sinova 2004] Sinova, J. et al. (2004) "Universal Intrinsic Spin Hall Effect" Phys. Rev. Lett. **92** 126603.

[Sogawa 2001] Sogawa, T., et al (2001) "Transport and Lifetime Enhancement of Photoexcited Spins in GaAs by Surface Acoustic Waves" Phys. Rev. Lett. **87** 276601

[Stern 2006] Stern, N. P. et al. (2006) "Current-Induced Polarization and the Spin Hall Effect at Room Temperature" Phys. Rev. Lett. **97** 126603.

[Stern 2007] Stern, N. P. et al. (2007) "Drift and Diffusion of Spins Generated by the Spin Hall Effect" Appl. Phys. Lett. **91** 062109.

[Stern 2008] Stern, N. P. et al. (2008) "Time-Resolved Dynamics of the Spin Hall Effect" Nat. Phys. **4** 843.

[Stevens 2002] Stevens, M. J. et al. (2002) "Coherent Control of an Optically Injected Ballistic Spin-Polarized Current in Bulk GaAs" J. Appl. Phys. **91** 4382.

[Stevens 2003] Stevens, M. J. et al. (2003) "Quantum Interference Control of Ballistic Pure Spin Currents in Semiconductors" Physical Review Letters **90** 136603.

[Stotz 2005] Stotz, J., Hey, R., Santos, P. and Ploog, K. (2005) "Coherent Spin Transport Through Dynamic Quantum Dots" Nat. Mat. **4** 585

[Tang 2007] Tang, Y. Q. et al. (2007) "Room-Temperature Spin-Oriented Photocurrent under Near-IR Irradiation and Comparison of Optical Means with Shubnikov De-Haas Measurements in $Al_xGa_{1-X}N$/GaN Heterostrucutres" Appl. Phys. Lett. **91** 071920.

[Terhune 1962] Terhune, R., Myker, P. and Savage, C. (1962) "Optical Harmonic Generation I Calcite" Phys. Rev. Lett. **8** 404.

[Tombros 2007] Tombros, N. et. al. (2007) "Electronic Spin Transport and Spin Precession in Single Graphene layer at room Temperature" Nature **448** 571.

[Tsukagoshi 1999] Tsukagoshi, K., Alphenaar, B. and Ago, H. (1999) "Coherent Transport of Electron Spin in a Ferromangetically Contacted Carbon Nanotubes" Nature **401** 572.

[Valenzuela 2006] Valenzuela, S. and Tinkham, M. (2006) "Direct Electronic Measurement of the Spin Hall Effect" Nature **442** 176 b.

[Wang 1990] Wang, C. T. (1990) "Introduction to Semiconductor Technology, GaAs and Related Compounds" Wiley and Sons NY.

[Wang 2010] Wang, J., Zhu, B. and Liu, R. (2010) "Second-Order Nonlinear Optical Effects of Spin Currents" Physical Review Letters **104** 256601.

[Wei 2007] Wei, C. M. et al. (2007) "Photogalvanic Effects for Interband Transition in p-type $Si_{0.5}$/Si Multiple Quantum Wells" Appl. Phys. Lett. **91** 252102.

[Werake 2011] Werake, L., Ruzicka, B. and Zhao, H. (2011) "Observation of Intrinsic Inverse Spin Hall Effect" Phys. Rev. Lett. **106** 107205.

[Werake 2010] Werake, L. and Zhao, H. (2010) "Observation of Second-Harmonic Generation Induced by Pure Spin Currents in Semiconductors" Nat. Phys. **6** 875.

[Wolf 2001] Wolf, S. A. et al. (2001) "Spintronics: A Spin Based Electronics Vision for the Future" Science **294** 5546.

[Wunderlich 2005] Wunderlich, J., Kaestner, B., Sinova, J. and Jungwirth, T. (2005) "Experimental Observation of the Spin Hall Effect in a Two-Dimensional Spin-Orbit Coupled Semiconductor System" Phys. Rev. Lett. **94** 047204.

[Yi 2005] Yi, H. et. al. (2005) “Spin Transport in an InAs based Two-Dimensional Electron Gas Nanochannel” J. Appl. Phys. **97** 10d502.

[Zhang 2000] Zhang, S. F. (2000) “Spin Hall Effect in the Presence of Spin Diffusion” Phys. Rev. Lett. **85** 393.

[Zhang 2005] Zhang, S. and Yang, Z. (2005) “Intrinsic Spin and Orbital Angular Momentum Hall Effect” Phys. Rev. Lett. **94** 066602.

[Zhao 2005] Zhao, H. et al. (2005) “Injection of Ballistic Pure Spin Currents in Semiconductors by a Single-Color Linearly Polarized Beam” Phys. Rev. B **72** 201302 R.

[Zhao 2006] Zhao, H., Loren, E., Driel, H. and Smirl, A. (2006) “Coherent Control of Hall Charge and Spin Currents” Phys. Rev. Lett. **96** 246601.

[Zhao 2007] Zhao, H., Smirl, A. and Driel, H. (2007) “Temporally and Spatially resolved Ballistic Pure Spin Transport” Phys. Rev. B **75** 075305.

[Zhao 2009] Zhao, H., Mower, M. and Vignale, G. (2009) “Ambipolar Spin Diffusion and D’yakonov-Perel Spin Relaxation in GaAs Quantum Wells” Phys. Rev. B **79** 115321.

[Zhao 2002] Zhao, B. et. al. (2002) “Spin-Coherent Transport in Ferromagnetically Contacted Carbon Nanotubes” Appl. Phys. Lett. **80** 3144

[Zutic 2004] Zutic, I., Fabian J. and Sarma S. (2004) “Spintronics: Fundamentals and Applications” Rev. of Mod. Phys. **76** 323